Dual optical frequency comb analog to digital conversion

A thesis submitted to UCL (University College London) for the partial fulfilment
of the requirements for the degree of Doctor of Philosophy (PhD)

Callum Deakin

Optical Networks Group
Department of Electronic and Electrical Engineering
University College London

Monday 1st August, 2022

Declaration

I, Callum Deakin, confirm that the work presented in this thesis is my own. Where information has been derived from other sources, I confirm that this has been indicated in the thesis.

Abstract

Analog to digital converters (ADCs) are the fundamental technology that allows the capture and analysis of signals across all scientific and engineering disciplines and underpin the digital links that connect our analog world. Modern communications systems demand high bandwidth, high resolution ADC in order to detect higher order modulation formats at high baud rates and maximise the spectral efficiency of the channel. However, the resolution of high speed (i.e. 1 GHz) electronic ADCs is typically limited by clock jitter and, at especially high frequencies, the speed of the component transistors that results in comparator ambiguity. This presents a trade-off between the frequency of the detected signal and accuracy, defined by the SINAD or ENOB. In a jitter limited ADC, the SINAD decreases quadratically with increasing frequency, giving a 6 dB SINAD penalty for every doubling of the input frequency.

This thesis proposes a frequency interleaving photonic front end for analog to digital converters, based on dual optical frequency combs, in order to meet this challenge of high speed, high resolution signal digitisation. Firstly, the dual frequency comb technique is described and modelled, both analytically and through simulations, to establish the potential performance of the dual comb approach in analog to digital conversion and other radio frequency signal processing applications. Secondly, a dual frequency comb prototype is experimentally demonstrated based on phase coherent electro-optic combs. The phase noise characteristics of the architecture are established and the prototype is evaluated using the IEEE ADC testing standard, outperforming any reported electronic ADC. Finally, arbitrary signal detection using the dual comb technique is demonstrated using a novel phase locking approach that efficiently utilises the comb bandwidth, and the impact of possible implementation errors is investigated.

Keywords: *analog-to-digital converter*, *optical signal processing*, *optical frequency comb*, *phase noise*, *jitter*.

Impact Statement

The vast interconnected web of wired and wireless connections that form the global communications infrastructure requires rapid conversion between the analog and digital domains. The traffic within these connections continues to increase exponentially, as new applications drive demand for increased and higher bandwidth connectivity. The techniques presented in this thesis can support this rapid growth by overcoming the limitations of current digitisation approaches. Enabling more efficient spectrum utilisation in the optical and radio frequency domains is essential to supporting future growth.

Aside from digital communications, the ability to detect high speed signals accurately for digital processing, storage and analysis is crucial across a wide variety of scientific and engineering disciplines such as radar systems and medical imaging. As with past developments in digitisation technology, it is anticipated that the capabilities demonstrated in this thesis may enable the unveiling of previously unseen physical phenomena and greater scientific understanding of complex systems.

Acknowledgements

My first thanks must go to my supervisor Dr Zhixin Liu. His relentless optimism and seemingly unlimited energy, combined with an extensive knowledge of all things optical and electronic, has made my PhD a fascinating and fantastic experience. I could not have asked for a better mentor.

This thesis would not be possible without the many fruitful discussions with the variety of experts throughout the department. In particular, I am deeply grateful to Dr Temitope Odedeyi and Prof. Izzat Darwazeh for their help with analog electronics, to Ronit Sohanpal for discussions on all things combs and Zichuan Zhou for his advice on every idea conceived in the lab.

I must also thank the many past and present members of the Optical Networks Group (ONG) who welcomed me so warmly into the group when I first joined and have supported me ever since. Specifically, Prof. George Zervas for first introducing me to the group, Prof. Polina Bayvel for her invaluable guidance and support, Dr Thomas Gerard and Dr Kari Clark for introducing me to the wonders of the ONG lab, Dr Eric Sillekens for his endless knowledge of apparently everything, Dr. Filipe Ferreira for always letting me borrow his power drill, and Dr Boris Karanov and Dr Paris Andreades for the being the life of 808. I hope those of us who joined along with myself in 2018, Wenting Yi, Hubert Dziecol and Xun Mu, have managed to maintain the 808 spirit!

Table of Contents

List of Figures

List of Tables

List of Terms and Abbreviations

ADC	analog-to-digital converter	9–14, 19–21, 26–30, 32–41, 49, 50, 52, 54, 55, 63–65, 70, 74, 76–81, 83–85, 90, 94, 95, 97–104, 131
ASE	amplified spontaneous emission	48, 83
AWG	arrayed waveguide grating	13, 74, 76, 80, 81
CMRR	common mode rejection ratio	79, 98, 100, 103
DAC	digital-to-analog converter	19, 20, 98
DSP	digital signal processing	83, 102
EDFA	erbium doped fibre amplifier	13, 19, 47–49, 70, 74, 75, 80, 81
ENOB	effective number of bits	28, 34, 40, 76, 78, 79, 82, 84, 103
FI	frequency interleaving	36, 38
FOM	figure of merit	103
GaAs	Gallium Arsenide	20
GSOP	Gram-Schmidt orthogonalisation procedure	15, 91, 94, 96–99
IEEE	Institute of Electrical and Electronics Engineers	9, 21, 33, 45, 70, 77
IMD3	3rd order intermodulation distortion	63, 82, 83
InP	Indium Phosphide	20
MZM	Mach-Zehnder modulator	82–84
PID	proportional integral derivative	71
PLL	phase-locked loop	12, 13, 70–73, 129

RF radio frequency . . . 39, 75, 76, 78, 80–82

RIN relative intensity noise . . . 47

SAR successive approximation register . . . 35

SFDR spurious free dynamic range . . . 12, 29, 62, 64–68, 77, 78

SINAD signal-to-noise-and-distortion ratio . 10, 12, 14, 29, 30, 33, 36, 41, 64–69, 75–77, 81–84

SNR signal-to-noise ratio 9, 13, 14, 19, 28–33, 35–38, 40, 48, 55, 62, 77–80, 82–84, 88–91, 98, 99

SOA semiconductor optical amplifier . . . 47, 48

SSBI signal-signal beat interference . . . 79, 98, 100

THD total harmonic distortion . . . 29, 55, 62

TI time interleaving . . . 34, 35, 37, 38

TIA transimpedance amplifier . . . 14, 15, 76, 78, 94, 98, 102, 103, 131

VCO voltage controlled oscillator . . . 72, 129

Chapter 1

Introduction

1.1 Scope of the Thesis

The digital representation of analog signals has revolutionised the storage, processing and transmission of information. The analog-to-digital converter (ADC) and its counterpart the digital-to-analog converter (DAC) are the essential tools that allow us to build this digital representation of our analog world, enabling a vast array of applications in communications, sensing and scientific research.

The explosive growth in optical and wireless communications in particular has driven demand for ADCs and DACs that can support the transfer of vast quantities of information. The amount of information per second, C, that can be sent through a noisy[*] channel is described by the Shannon-Hartley theorem [1, 2]

$$C = B \log_2(1 + \text{SNR}) \tag{1.1}$$

for bandwidth B and signal-to-noise ratio (SNR). Clearly, increasing either B or SNR will increase the information carrying capacity of the channel, but the logarithmic function in (1.1) means that increasing B is often easier. This is reflected in the history of optical communications, where the vast available bandwidth offered by erbium doped fibre amplifiers (EDFAs) ensured that much of the early development of such systems focused on increasing the bandwidth while maintaining simple modulation formats that require only low SNR for accurate detection [3].

As demand continues to grow however, the bandwidth becomes ultimately limited by some physical effect. This problem is already acutely evident in wireless communications, where the limited radio bandwidth is strictly regulated among competing use cases and businesses. In this case, communications engineers must turn to increasing the SNR and using high order modulation formats to increase the information carrying capacity of the channel.

All digital communications therefore eventually require ADCs and DACs that can handle high bandwidth signals without degrading the SNR. Besides communications systems, the detection and generation of high frequency signals is an essential tool for

---

[*] additive white Gaussian noise

science and engineering. ADCs are ubiquitous in any application that requires continuous time signals to be converted to computer-readable form for processing and storage, such as medical imaging, instrumentation, electronic warfare and consumer electronics.

However, designing data converters that can simultaneously meet these requirements is extremely challenging. ADCs and DACs exhibit a tradeoff between speed and resolution. Historically, the main limitation on the accuracy of high speed converters was the switching speed of the integrated circuit technology, such as Indium Phosphide (InP) or Gallium Arsenide (GaAs), while lower speed converters were typically limited by thermal noise [4]. However, progress in converter design has meant that for high speed ADCs the sampling clock jitter is often the main culprit for this tradeoff.

The challenge of high speed, high resolution conversion has led to a variety of solutions across industry and academia, with leading instrument manufacturers for example employing electronic time and frequency interleaving techniques to increase sampling rate and bandwidth [5]. In academia, many have turned to optics to overcome the bandwidth/resolution tradeoff: photonic based converters utilise the high bandwidth and low jitter of optical signals to increase the absolute bandwidth of converters whilst maintaining high resolution, and could lead to a potentially revolutionary increase in the performance of the vast array of technologies that rely on high speed data converters [6].

In this thesis, we propose using phase stable dual frequency combs as the basis of a photonic frequency interleaved ADC architecture. Frequency interleaving has reduced sensitivity to channel mismatch and timing errors, and performing this channelisation in the optical domain eliminates the need for high frequency electronic circuit design that degrades the performance of electronic frequency interleaving solutions. This concept, supported by the meteoric advance in frequency comb technology over the past few decades [7], could provide a scalable solution for the development of high bandwidth, high resolution data converters. Furthermore, the analysis of dual frequency comb based channelizers presented in this thesis could enable wider deployment of the dual frequency comb technique in signal processing applications.

1.2 Chapter Overview

The rest of this thesis is arranged as follows:

Chapter 2 describes analog to digital converters, including their theory of operation, performance metrics and common noise sources that can degrade their performance. Common approaches to conventional high speed electronic ADCs are discussed along with previously published photonic ADCs and subsystems required for dual optical frequency comb ADCs.

Chapter 3 introduces the dual frequency comb ADC concept and develops a theoretical framework for the performance analysis of dual frequency comb based channelizers in general. The model is compared to simulations of a dual frequency comb ADC detecting single- and two-tone test signals.

In *Chapter 4* a prototype dual frequency comb ADC is designed, built and tested using the Institute of Electrical and Electronics Engineers (IEEE) ADC sine wave testing standard. The phase noise of dual comb system is also measured to verify the model derived in Chapter 3.

Chapter 5 describes a technique for detecting arbitrary signals within each dual comb sub-band without the use of coherent receivers, based on stabilising the phase relationship between the dual combs. This method is used to detect sub-band limited arbitrary signals, and possible implementation errors are examined both analytically and experimentally.

Chapter 6 concludes the thesis and details possible future work on dual comb ADCs, including prospects for photonic integration and phase noise compensation techniques to improve performance.

Appendix A provides mathematical derivations supporting equations shown elsewhere within the thesis.

Appendix B provides supplementary data relating to simulations and experiments presented throughout the thesis.

1.3 Key Contributions

The key contributions of this thesis included:

i) The concept of using dual frequency combs as a frequency interleaving front end for analog to digital conversion is proposed. This was first published in [8] along with preliminary experimental results.

ii) A comprehensive analysis of noise and distortion sources in more general dual frequency comb based channelizers is presented and was published in [9, 10].

iii) A model of phase noise in phase coherent dual comb systems was developed and published in [9, 10].

iv) The phase noise of coherent electro-optic dual comb systems was measured and explained using the phase noise model in [9]. These results were published in [11].

v) The dual comb analog to digital converter was shown to outperform conventional electronic ADCs in [12].

vi) A method for using the upper and lower sidebands of the comb for arbitrary signal detection using dual frequency combs has been derived. This was published in [13].

vii) Sub-band limited arbitrary signal detection using the method described in [13] was demonstrated for the first time, and the impact of phase locking error was discussed.

1.4 List of Publications

The following publications resulted from the work presented in this thesis:

Journal papers

1. **C. Deakin** and Z. Liu, “Dual frequency comb assisted analog-to-digital conversion,” *Optics Letters*, vol. 45, no. 1, pp. 173176, 2020.
2. **C. Deakin** and Z. Liu, “Noise and distortion analysis of dual frequency comb photonic RF channelizers,” *Optics Express*, vol. 28, no. 26, pp. 39750-39769, 2020.
3. **C. Deakin** and Z. Liu, “Phase noise of electro-optic dual frequency combs,” *Optics Letters*, vol. 46, no. 6, pp. 1345-1348, 2021.

Conference papers

1. **C. Deakin**, T. Odedeyi, and Z. Liu, “Dual Frequency Comb Photonic Analog to Digital Conversion,” *2020 IEEE Photonics Society Summer Topical Meeting Series (SUM)*, paper WB4.3, Jul. 2020.
2. **C. Deakin**, and Z. Liu. “Performance of dual frequency comb channelizers for RF signal processing”, *2021 Optical Fiber Communications Conference and Exhibition (OFC)*, paper Tu5F.4 , Jun. 2021.
3. **C. Deakin**, and Z. Liu, “Frequency interleaving dual comb photonic ADC with 7 bits ENOB up to 40 GHz,” *2022 Conference on Lasers and Electro-Optics (CLEO)*, paper STh5M.1, May 2022.

Patents

1. Z. Liu, and **C. Deakin**. “Signal processor apparatus”, International App. No. PCT/GB2021/050452, Feb. 2020.

The following academic publications also include contributions that were made by the author of this thesis during the completion of their PhD project, which are not presented within this thesis:

Journal papers

1. **C. Deakin**, M. Enrico, N. Parsons and G. Zervas, "Design and Analysis of Beam Steering Multicore Fiber Optical Switches," *Journal of Lightwave Technology*, vol. 37, no. 9, pp. 1954-1963, 2019.

2. K. T. P. Lim, **C. Deakin**, B. Ding, X. Bai, P. Griffin, T. Zhu, R. A. Oliver, and D. Credgington, "Encapsulation of methylammonium lead bromide perovskite in nanoporous GaN," *APL Materials*, vol. 7, pp. 021107, 2019.

3. W. Yi, Z. Li, Z. Zhou, E. Sillekens, T. Gerard, **C. Deakin**, F. M. Ferreira, L. Galdino; Z. Liu, P. Bayvel, and R. I. Killey. 'Frequency-modulated Chirp Signals for Single-photodiode Based Coherent LiDAR System,' *Journal of Lightwave Technology*, vol. 39, no. 14, p. 4661-4670, 2021.

4. Z. Zhou, K. Clark, **C. Deakin**, and Z. Liu. 'Clock synchronized transmission of 51.2 GBd optical packets for optically switched data center interconnects,' *Journal of Lightwave Technology*, vol. 40, no. 6, p. 1735-1741, 2022.

5. R. Sohanpal, H. Ren, L. Shen, **C. Deakin**, A. M. Heidt, T. W. Hawkins, J. Ballato, U. J. Gibson, A. C. Peacock, and Z. Liu. "All-fibre heterogeneously-integrated frequency comb generation using silicon core fibre." *Nature Communications* 13, 3992, 2022.

Conference papers

1. Z. Zhou, J. Wei, K. Clark, E. Sillekens, **C. Deakin**, R. Sohanpal, Y. Luo, R. Slavik, and Z. Liu. 'Multipoint-to-Point Data Aggregation Using a Single Receiver and Frequency-Multiplexed Intensity-Modulated ONUs ', *2022 Optical Fiber Communications Conference and Exhibition (OFC)*, paper Tu2G.4, Mar. 2022.

2. R. Sohanpal, H. Ren, L. Shen, **C. Deakin**, A. M. Heidt, T. W. Hawkins, J. Ballato, U. J. Gibson, A. C. Peacock, and Z. Liu. 'Parametric frequency comb generation using silicon core fiber', *2021 Optical Fiber Communications Conference and Exhibition (OFC)*, paper M5B.5, Jun. 2021.

3. Z. Zhou, K. Clark, **C. Deakin**, P. Laccotripes, and Z. Liu. 'Clock Synchronized Transmission of 51.2 GBd Optical Packets for Optically Switched Data Center

Interconnects', *2021 Optical Fiber Communications Conference and Exhibition (OFC)*, paper Th4E. 2 , Jun. 2021.

Chapter 2

Background and literature review

This Chapter introduces fundamental ADC theory and common performance metrics for the evaluation of ADC performance. Common noise sources, with a special focus on clock jitter, are discussed and how they can degrade ADC performance along with common high speed ADC designs. A review of previous proposals for photonic ADCs is presented, followed by a review of the required subsystems for the dual comb ADC designs presented in this thesis and a unified discussion of opto-electronic oscillator phase and amplitude noise.

2.1 ADC characterisation

The digitisation of any analog signal requires assigning discrete values to both time and the measured quantity (e.g. voltage). These two processes are referred to as sampling and quantisation respectively, and it is important to separate these two operations in any theoretical description since these are directly related to our two performance parameters. The number of sampling points per second relates to the bandwidth of the instrument, whilst the number of quantisation levels relates to the resolution of the conversion process. Sampling and resolution therefore relate to how precisely an ADC can measure an analog signal in the time and voltage domains respectively.

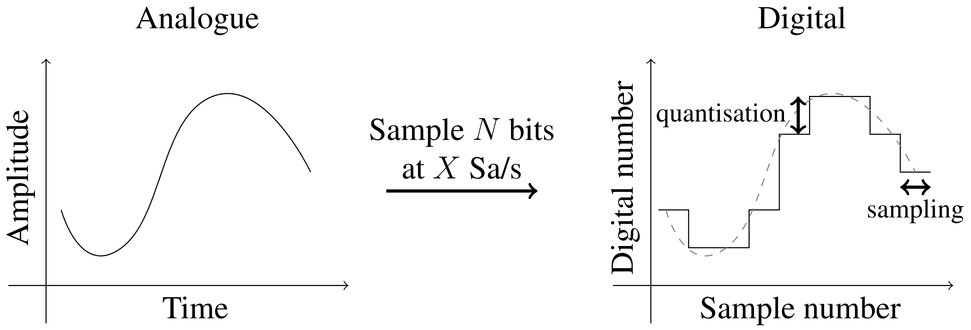

Fig. 2.1: An analog signal can be represented digitally by a series of discrete values.

The resolution of a converter is the number of discrete amplitude levels it can produce, usually expressed in number of bits, meaning a N-bit converter can output 2^N

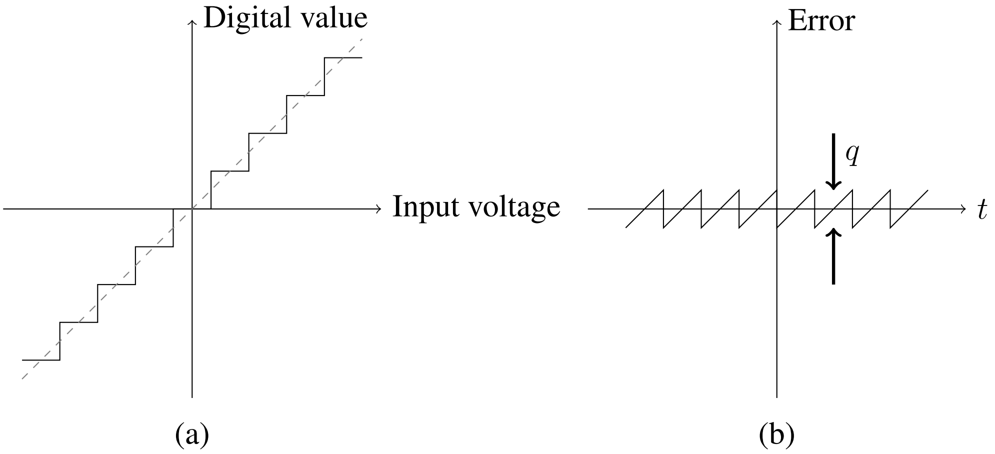

Fig. 2.2: Quantisation noise can be derived by considering the ADC response to a linear increase in voltage, (a), and the subsequent error (with maximum error of $\pm q/2$) in the digitised signal compared to the actual analog input, versus time, t, (b) [14].

voltage levels. Quantising an analog signal into 2^N digital levels introduces noise into the system, referred to as quantisation noise. To understand how this noise will manifest itself in the digital representation of a signal, consider the digital values produced by a linear ramp in voltage at the input, as shown in Fig. 2.2(a). The corresponding error produced by the quantisation process is shown in Fig. 2.2(b), which is a sawtooth function with respect to time of slope s with a worst case error of $\pm q/2$

$$e(t) = st, \frac{-q}{2s} < t < \frac{q}{2s} \tag{2.1}$$

for the minimum distinguishable voltage change q, i.e. the full scale voltage input divided by 2^N. The root mean square quantisation error is then

$$e_{\text{RMS}} = \sqrt{\overline{e^2(t)}} = \sqrt{\frac{s}{q}\int_{-q/2s}^{q/2s}(st)^2dt} = \frac{q}{\sqrt{12}}. \tag{2.2}$$

The noise introduced by the quantisation process is essentially a nonlinear distortion applied by modulating the incoming signal with the staircase function. Such noise is usually white and Gaussian, except in circumstances where the signal and clock are harmonically related: in this case, the quantisation noise will be concentrated in harmonics of the input signal [14].

Now consider a sine wave input that spans the full scale of the ADC

$$V_{\text{in}}(t) = \frac{q2^N}{2}\sin(\omega t). \tag{2.3}$$

By taking the ratio of the mean square sine wave amplitude to the mean square of the quantisation noise, we obtain the signal to noise ratio due to quantisation noise in an ideal ADC, i.e. one without any error or uncertainty in the sampling or quantisation process. In decibels

$$\mathrm{SNR_q} = 10\log_{10}\left(\frac{q2^N\sqrt{12}}{q2\sqrt{2}}\right)^2 = 20\log_{10}\left(\frac{2^N\sqrt{3}}{\sqrt{2}}\right). \tag{2.4}$$

This is often written simply as

$$\mathrm{SNR_q} = 6.02N + 1.76. \tag{2.5}$$

If the signal does not swing across the full voltage range of the converter then the analog signal will be represented using less than the full 2^N levels and will see a subsequent reduction in SNR. Thus the SNR calculated by (2.4)/(2.5) represents a theoretical maximum for an ideal ADC, with the aforementioned assumptions.

The actual SNR of a real converter is further reduced from this theoretical maximum by several factors dependent on the ADC implementation, which are discussed later in this Chapter. The net result of these additional noise sources will result in a measured SNR that is below the theoretical maximum defined by (2.5). Rearranging (2.5) allows us to infer an effective number of bits (ENOB) for a given SNR

$$\mathrm{ENOB} = \frac{\mathrm{SNR_q} - 1.76}{6.02}. \tag{2.6}$$

ENOB is a common metric for defining the accuracy of an ADC since it allows us to compare a real converter to its ideal counterpart. For example, a converter with a measured SNR of 62 dB has an ENOB of 10 bits, and therefore has a resolution equivalent to a 10-bit ideal converter.

The key parameter in the time domain is sampling rate, which defines the highest frequency that a converter can handle without aliasing. This is the result of the Nyquist sampling theorem, which requires a sampling rate of f_s to perfectly reconstruct a signal with highest frequency $f_s/2$. For ADCs, a frequency f_a above f_s will be indistinguishable from the frequency $f_b = f_s - (f_a - f_s)$ and appear as its alias in the ADC spectrum. This is illustrated in Fig. 2.3. Note that an ideal ADC with an infinitely flat frequency response can in theory detect arbitrarily high frequencies, but will be unable to distinguish a signal from its aliases in the other Nyquist zones. As a consequence, the maximum bandwidth wideband signal that an ADC can detect is $f_s/2$ [2].

However, the frequency response of the analog circuitry within a real converter is inevitably not flat due to the finite frequency response of its constituent components.

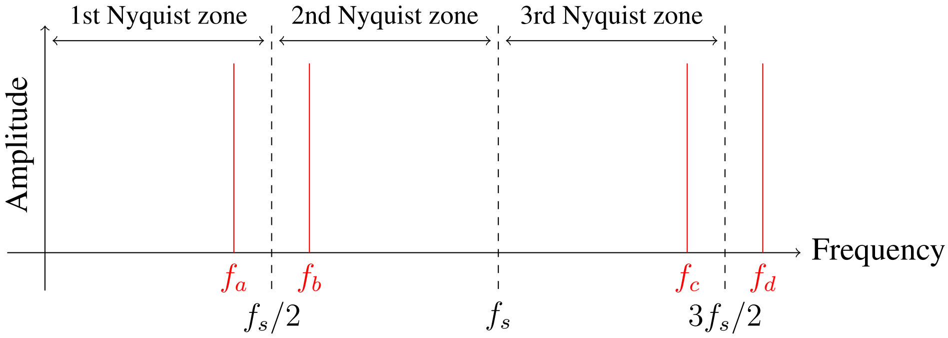

Fig. 2.3: Aliasing occurs in ADCs with a finite sampling rate f_s. The result is that the detected frequencies f_a, f_b, f_c, f_d are indistinguishable in the digitised signal, and the the ADC can only detect wideband signals of bandwidth $f_s/2$ unambiguously.

The response of a converter will be reduced at higher frequencies and so it is also necessary to define the analog bandwidth, which is the frequency at which the amplitude of a signal is reduced by 3 dB. For example, a 100 GSa/s ADC might only have an analog bandwidth of 23 GHz*, which means that although the ADC can detected signals up to 50 GHz without aliasing, signals at 23 GHz will be detected with 3 dB lower SNR. On the other hand, a 3 GSa/s ADC might have an analog bandwidth of 9 GHz†, which allows it to detect 1.5 GHz bandwidth signals well above its Nyquist frequency in what is sometimes referred to as ‘intentional aliasing’. This is a common scenario in wireless communications, where the ability to directly detect narrow band signals at high frequencies has eliminated the need for local oscillators at the receiver front end in software defined radio [15].

Another important metric when assessing converter performance is spurious free dynamic range (SFDR). SFDR is the ratio of the power of the signal to that of the worst spurious signal in the spectrum, which is often a harmonic of the input signal. In this case, SFDR is measure of the nonlinearity of the system. However the SFDR-limiting spur can also be a result of non-ideal interleaving of separate channels in more complex ADCs. In any case, SFDR is especially important for communications systems where it represents the smallest change in the signal that can be distinguished from an interfering spur.

To more precisely define the ADC nonlinearity, the strength of the inter modulation distortion products can be measured. Summing all of the harmonics generated gives the total harmonic distortion (THD). Typically ADC specifications draw a distinction between SNR without harmonic distortion, which is simply referred to as SNR, and signal-to-noise-and-distortion ratio (SINAD)

$$\mathrm{SINAD} = (\mathrm{SNR}^{-1} + \mathrm{THD}^{-1})^{-1} \tag{2.7}$$

---

*Tektronix DPO72304DX digital phosphor oscilloscope.

†Analog devices AD9208.

This distinction between SNR and SINAD is made because for narrowband signals, harmonics can be easily filtered out meaning that SNR is the key quantity. However for wideband signals, distortion products cannot be easily filtered and so SINAD is the key quantity. We will follow these definitions thoughout this thesis, and since our focus is on the digitisation of wideband signals, SINAD will be our key metric when assessing ADC designs.

2.1.1 Sampling clock jitter in ADCs

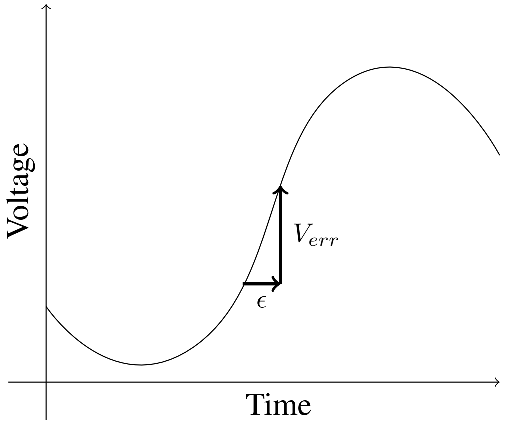

Fig. 2.4: A sampling error ϵ translates to a voltage error V_{err} in the ADC output. The magnitude of the error is directly related to the current slope of the signal, which is in turn related to the frequency of the signal.

Aside from the aforementioned quantisation noise, the principle cause of SINAD degradation in high speed ADCs is clock jitter. Jitter (or phase noise) in the sampling clock causes variations in the periodicity of the sampling points and consequently degrades SINAD. To understand how jitter in the sampling clock degrades the accuracy of the digitised signal, consider a sinusoidal input to an ADC with frequency f

$$V_{in}(t) = A\cos 2\pi f t \tag{2.8}$$

which is sampled N times at times

$$t = nT_s + \epsilon \tag{2.9}$$

with T_s defining the sampling period. ϵ represents the sampling error induced by clock jitter, which follows a Gaussian distribution $N(0, \sigma^2)$. The sampled output is then

$$V_{out}(nT_s) = V_{in}(nT_s + \epsilon) \tag{2.10}$$

with the resulting voltage error defined as

$$V_{err}(t) = V_{out}(nT_s) - V_{in}(nT_s) \tag{2.11}$$

and noise power

$$P_N = \frac{1}{N} E\left\{ \sum_{n=0}^{N-1} [V_{err}(nT_s)]^2 \right\} \tag{2.12}$$

Where $E\{\cdot\}$ is the expectation value operator. For the sinusoidal input Eq. 2.8

$$P_N = A^2(1 - \exp(-2\pi^2 f^2 \sigma^2)) \tag{2.13}$$

which corresponds to an SNR (in dB)

$$\text{SNR} = -10 \log_{10}[2(1 - \exp(-2\pi^2 f^2 \sigma^2))] \tag{2.14}$$

In the limit $2\pi f \sigma \ll 1$, the jitter σ is significantly less than a single cycle of the input frequency. This allows the linear approximation of the exponential function Taylor expansion, giving

$$P_N \approx 2\pi^2 A^2 f^2 \sigma^2 \tag{2.15}$$

$$\text{SNR} \approx -20 \log_{10}(2\pi f \sigma) \tag{2.16}$$

An inituitive derivation of this approximation can be found in [16] and was orignally derived in [17]. This approximation is generally accurate for any reasonable (> 10 dB) SNR level. It clearly fails for large $2\pi f \sigma$, since the noise power in Eq. 2.15 diverges, leading to strongly negative SNRs. In reality the SNR approaches -3 dB in the large jitter / high frequency limit as per Eq. 2.14.

In [18], this idea is extended to any arbitrary input to give the noise power

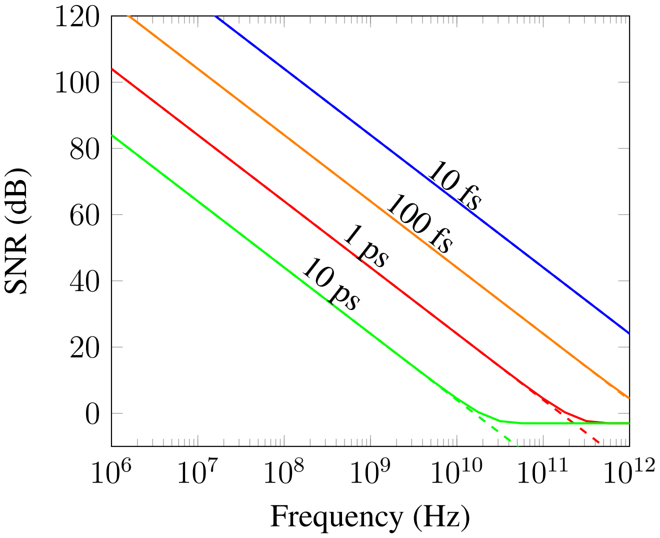

Fig. 2.5: Maximum SNR vs frequency, limited by sampling clock jitter. Solid lines are Eq. 2.14, dashed lines are Eq. 2.16. Eq. 2.16 is a very good approximation except for very low SNRs.

$$P = \int_{\infty}^{-\infty} |F(\omega)|^2 [1 - \exp\Big(- \frac{\omega^2 \sigma^2}{2} \Big)] d\omega \tag{2.17}$$

provided that the Fourier transform of $V_{in}(t)$, $F(\omega)$, exists, i.e. the input signal is an absolutely integrable function. This result is somewhat intuitive given the result for a single sine wave in Eq. 2.13 and considering that a signal can be described as a sum of sinusoids. The total noise power is simply a sum over all frequencies of the noise power produced by a single sinusoid at each frequency, with the amplitude A^2 replaced by the amplitude of the Fourier transform at each frequency.

Eq. 2.16 and Fig. 2.5 clearly illustrate the importance of clock stability at high frequencies. The clock stability of an oscillator is more often described by its phase noise, which can be converted to jitter by integrating the phase noise over the bandwidth of interest,

$$\sigma = \frac{1}{2\pi f_0} \sqrt{2 \int_{f_L}^{f_U} \mathscr{L}(f) df} \tag{2.18}$$

where σ is the RMS jitter in seconds. The quantity $\mathscr{L}(f)$ is the single sided power spectral density of the phase noise, as is typically specified by the oscillator manufacturer measured at the frequency f_0 [19]. The frequency f_U defines the highest offset frequency considered, which in the case of an ADC is typically the bandwidth of the clock driving circuitry, also called the ‘encode’ bandwidth. For high frequency ADCs this can greatly exceed the frequencies specified in phase noise measurements for oscillators, which are usually only specified to around 10 MHz, so it is important to understand if the wideband phase noise is making a contribution to the clock jitter [20]. The lower frequency limit, f_L, is often a little trickier to specify, since it is essentially application specific and depends on how many samples the ADC needs to capture. The longer the capture, the more the long term frequency drift of the oscillator affects the measurement and so f_L should be set closer to the carrier. In many applications such as communications, sufficiently slow phase noise can be effectively compensated by digital signal processing algorithms [21, 22].

2.2 High speed electronic ADCs

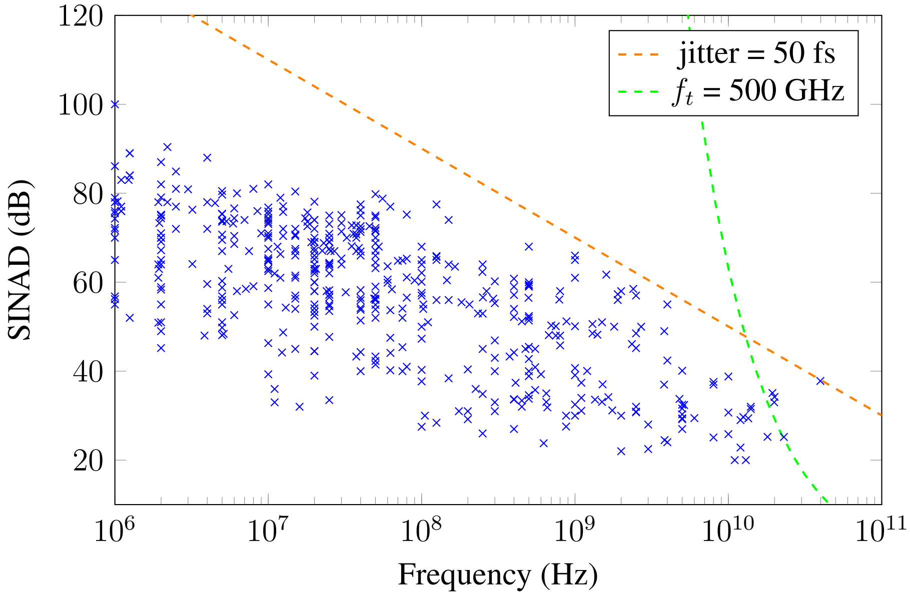

Fig. 2.6: SNR measured at the maximum input frequency for ADC designs presented at International Solid-State Circuits Conference and the IEEE Symposium on Very Large Scale Integration Technology and Circuits from 1997-2021. Theoretical limits imposed by clock jitter of 50 fs and transistor transition frequency of 500 GHz are shown. Adapted from [23], data from [24].

The current state of the art for high speed electronic ADCs is demonstrated by Fig. 2.6, which maps the SINAD achieved at the highest input frequency measured (which may be at or above the Nyquist frequency) for results presented at the two main semiconductor conferences: International Solid-State Circuits Conference and the IEEE Symposium on Very Large Scale Integration Technology and Circuits. The tradeoff between SINAD and frequency is clearly demonstrated, as well as the scarcity of results at frequencies above 20 GHz. A jitter of around 50 fs represents the current state of the art and it is clear that this imposes the current performance limit for gigahertz frequencies. Lower ($< 10^8$ Hz) frequencies cannot approach the jitter limit as readily since their performance is further degraded by thermal noise [23].

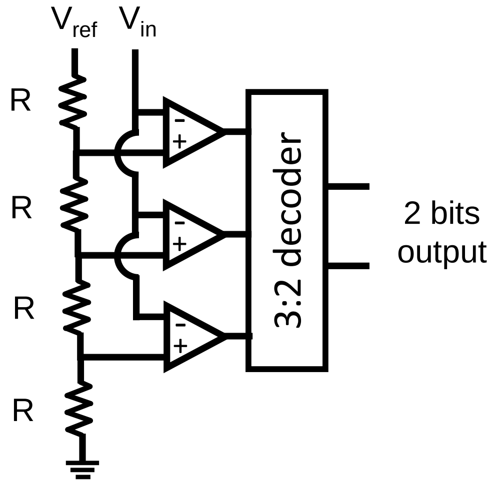

Fig. 2.7: A 2 bit flash ADC, requiring 3 comparators. An N bit ADC requires $2^N - 1$ comparators.

At especially high frequencies (>10 GHz), the speed of the component transistors also start to limit performance. At high frequencies, the comparators within the ADC are unable to make a unambiguous decision regarding the relative input voltage amplitudes, due to the switching speed of the integrated circuit technology used to manufacture the device. Device speed is measured using the transition frequency f_T, which for the latest transistor designs can be over 500 GHz [25], and defines the maximum achievable ENOB

$$\text{ENOB}_{\text{comparator}} = \frac{\pi f_T}{13.9 f} - 1.1 \tag{2.19}$$

which imposes a strict limit on the highest frequency that a single comparator can accurately detect [23].

2.2.1 Time interleaving ADCs

The simplest and fastest ADC implementation is what is known as a flash ADC which consists simply of a resistor ladder followed by a bank of parallel comparators, as shown in Fig. 2.7. To implement a N-bit flash ADC, $2^N - 1$ comparators are required that must operate at the full sampling rate. At high resolutions therefore, the flash ADC becomes completely infeasible due to the exponential increase in power consumption and input buffer capacitance [26]. Moreover, switching all of the comparators at the full sampling rate makes the design susceptible to comparator ambiguity [23].

To overcome these challenges, almost all modern high speed ADCs are time interleaving (TI) designs, as shown in Fig. 2.8. In time interleaving, the input signal is

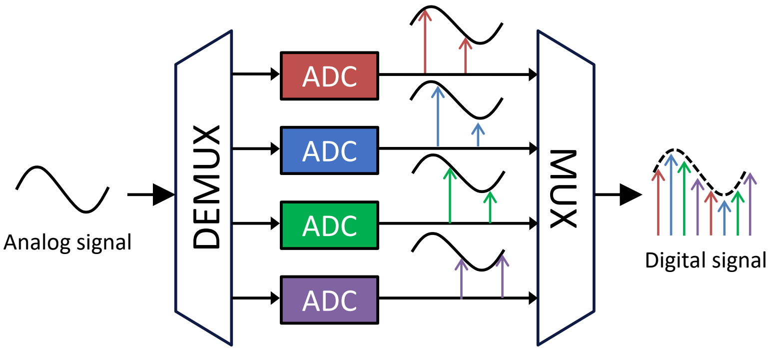

Fig. 2.8: Time interleaving ADC concept. The incoming signal is sampled by a bank of M sub-ADCs in turn, such that they can operate a fraction $1/M$ of the total sampling rate.

concurrently sampled by a bank of M parallel sub-ADCs whose sampling clock is offset from the neighbouring ADCs by a fraction $1/M$ of a clock cycle. In this way, the input signal can be sampled in turn by each ADC operating at $1/M$ of the total desired sampling rate. This architecture allows for slower ADC designs, such as successive approximation register (SAR) ADCs, to be used that can achieve much higher resolution than is possible using a flash design. Furthermore, the sampling clock distributed to the sub-ADCs is only $1/M$ the frequency of the total sampling rate which greatly simplifies clock generation. The best performing high speed ADCs typically implement a TI-SAR design with up to 72 channels [27, 28, 29].

Although TI-ADCs allow for efficient implementation of high sampling rate ADCs, the design of TI-ADCs is not without its challenges. Firstly, time-interleaving does not avoid the jitter problem and TI-ADCs follow the exact same SNR degradation due to jitter described by (2.14)/(2.16) as a direct sampling ADC, since the derivation of (2.14)/(2.16) does not assume any relationship between the phase error imposed on successive samples, other than they are drawn from the same Gaussian distribution. This is also evident from the fact that despite each sub-ADC running at a fraction of the full sampling rate, each ADC still samples the entire signal bandwidth and therefore subject to the same jitter requirements.

Secondly, the input buffer, the principal component of the ‘DEMUX’ shown in Fig.2.8, often limits the ADC analog bandwidth. At high channel counts, the input capacitance becomes quite large and as a result makes designing high bandwidth input buffers extremely challenging. For example, the bandwidth of the 90 GSa/s ADC in [29] is less than half the Nyquist frequency at 20 GHz, almost certainly a result of the limited bandwidth of the input buffer that has to distribute its output to 64 channels. In [27], this problem is alleviated somewhat by using a cascaded input buffer structure at the cost of a small power penalty, achieving 40 GHz analog bandwidth for a 97 GSa/s design.

Finally, all TI-ADC designs have to contend with the effects of channel mismatch.

Ideally, each channel should be physically identical and the timing offset between the sampling clock in each channel should be precisely calibrated. In reality, manufacturing variations lead to differences in the gain, offset (DC level), and timing (referred to as skew) between each channel. Of course, all of these mismatch effects are deterministic once the ADC is manufactured and so are possible to correct using post-production calibration techniques [30]. Offset mismatch is the easiest to correct since it generates observable spurs in the digital output that are independent of the input signal [31], and for some signals may not even cause a degradation in SINAD. Gain and timing mismatch are trickier since they are dependent on the input signal and will generate the same spurious spectral components, so must be considered together during calibration [32, 33].

2.2.2 Frequency interleaving ADCs

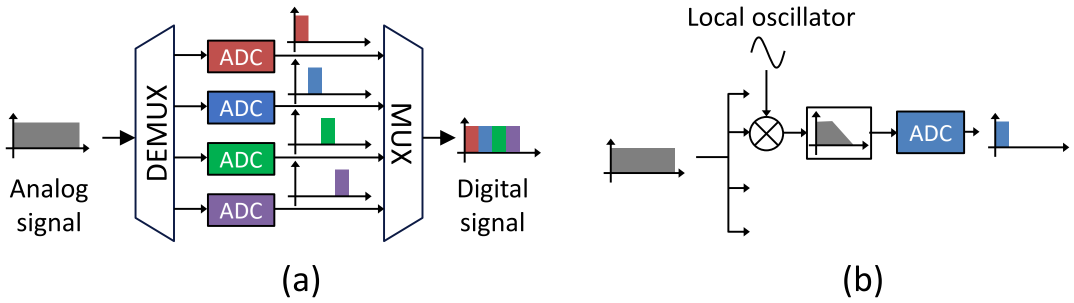

Fig. 2.9: (a) Frequency interleaving ADC concept. The incoming signal is separated into M frequency sub-bands, either by simple filtering or a combination of local oscillator down conversion and filtering, to be sampled by the parallel ADCs. The signal is then reconstructed digitally. (b) Example DEMUX circuit for a frequency interleaving ADC, consisting of a local oscillator and low pass filter before digitisation by the sub-ADC.

One alternative to the time-interleaving approach is to instead perform the interleaving in the frequency domain, which is shown conceptually in Fig. 2.9. In a frequency interleaving (FI) ADC system, the input signal is channelised into M frequency bands by a bank of down mixing local oscillators and low pass filters [34, 35]. In the original formulation [34] down-mixing local oscillators were not required since the overall sampling speed was low. The frequency shifting was achieved by intentional aliasing at the sub-ADCs since the analog bandwidth of the ADCs was sufficient to prevent significant SNR degradation. In high speed designs (e.g. [36]), down mixers are required since the analog bandwidth is often close or even below the Nyquist frequency of the sub-ADC. Furthermore, without down mixing local oscillators the sub-ADCs still have to sample the high frequency components of the signal directly and so follow the same jitter-SNR degradation derived in (2.14)/(2.16).

The original motivation for exploring frequency interleaving as an alternative to time-interleaving was to reduce susceptibility to channel mismatch effects [34]. The spurious frequency components generated by mismatch errors are the same as time interleaving since they simply describe the input frequency being detected out of band by the sub-ADCs not assigned to its frequency band. However, the attenuation of the out of band signals means that the distortions caused by mismatches in frequency interleaved systems are significantly reduced for timing and gain errors [37]. For DC offset errors, the distortion level is actually increased, but as this is an input signal independent distortion it is the most easily correctable. The detailed mathematical treatment of these errors is described in [37, 38]. In any case, all of these errors, as in the time interleaving case, are deterministic and therefore correctable through calibration or compensation.

Now let us consider how clock jitter affects the frequency interleaving system. Considering a bank of perfect ‘brick wall’ filters and noiseless local oscillators, the bandwidth requirements of a single sub-ADC is reduced by M which modifies (2.16) to

$$\text{SNR} \approx -20\log_{10}\left(\frac{2\pi f\sigma}{M}\right) = -20\log_{10}(2\pi f\sigma) + 20\log_{10}(M) \tag{2.20}$$

and relaxes the jitter requirements to that of the sub-ADC [39]. This naive formulation suggests an SNR gain of $20\log_{10}(M)$ over a single ADC (and equivalently, any TI-ADC) in a jitter limited system. Another way to see how this gain arises is that in contrast to the time interleaving case, the parallel samples for each sub-ADC are taken at the same time instant, rather than being phase offset as in time interleaving. Thus, any phase errors produced by the sampling clock will be perfectly correlated across all sub-ADCs. This maintaining of the sub-ADC SNR is demonstrated in [40].

However, (2.20) is naive in several aspects. Firstly, real filters have finite roll-offs and therefore cannot provide perfect channel separation. This means the attenuated aliased out-of-band signal is present at every sub-ADC, and in the case of uniformly channelised first order filters, leads to worse jitter performance than the single or time interleaved ADC case [41]. In order to actually achieve the promised benefits of frequency interleaving, high order uniform filters are generally required [42]. Some have utilised low order filters by reducing the bandwidth of the filter to below the channel bandwidth, but this necessarily causes detrimental in-band losses that must be compensated [41]. The analog filter bank design is critical therefore in any frequency interleaving design, which is why they are sometimes referred to as ‘hybrid filter bank’

ADCs.

Aside from filter design, the key challenge introduced by the frequency interleaving architecture is the introduction of additional phase noise and harmonics from the down converting local oscillators. This is explored extensively in [43] and also considered in [44]. A more accurate description of the jitter-SNR limit for an FI-ADC includes the phase noise introduced by the down mixing local oscillators [43]

$$\text{SNR} \approx -10\log_{10}[(2\pi f_{IF}\sigma_{sampling})^2 + 2(2\pi f_{LO}\sigma_{LO})^2] \tag{2.21}$$

Where $\sigma_{sampling}$ is the sampling clock jitter at the sub-ADC, σ_{LO} is the jitter of the down converting local oscillator, f_{LO} is the local oscillator frequency and f_{IF} is the downconverted frequency observed at the sub-ADC. It is likely that the LOs and sampling clock will be derived from the same reference clock, so it is not immediately clear that the apparent decreased jitter sensitivity can be maintained in any practical frequency interleaving design. However, although σ_{LO} and $\sigma_{sampling}$ may be derived from the same reference the integration limits when calculating the jitter (see (2.18)) will be different, since we only need to integrate to the maximum possible frequency, f_{max}, that will be presented to the ADC as all phase noise above this point can be eliminated by placing a low pass filter with a stop band of f_{max} before the ADC. For a TI-ADC, the sub-ADCs still see the full bandwidth so f_{max} is the full bandwidth of the entire ADC. But for a FI-ADC, for M channels a sub-ADC will only see a $1/M$ fraction of the signal bandwidth so we only need to integrate f_{max}/M.

It is possible therefore for the FI-ADC to outperform direct sampling or TI-ADCs. At what frequency the FI-ADC starts outperforming its TI-ADC all depends on the integration bandwidth of σ_{LO}, i.e. the bandwidth of the sub-ADCs. More channels should lead to higher performance, provided that mismatches can be compensated. Ref. [43] shows this by simulating an 8-channel FI-ADC architecture at the system level and obtains a 6-12 dB SNR improvement at a Nyquist frequency of 25 GHz over the equivalent TI-ADC architecture.

As well as having low phase noise, the local oscillators also need to be free of harmonic distortions. The presence of higher order harmonics within the LO before mixing will lead to the undesired shifting of higher channels to the baseband. For a large number of channels, M, harmonic mixing will become a serious issue that will hinder the SNR, especially in the lower frequency bands. Even if there is no signal content in the higher bands, the noise will still be mixed to the lower bands and decrease the SNR. To mitigate this, filters or harmonic rejection mixers can be used that reduce the higher frequency harmonics [45, 46]. A digital compensation technique for harmonic rejection in FI-ADCs is also demonstrated in [47].

2.3 Photonic ADCs

Photonic components have been employed in ADC designs since the early 1970s, although they have yet to be widely adopted in commercial devices [6]. The relative immaturity of photonic components and relentless advance in digital electronics has ensured that photonic ADCs have remained within the academic and research communities. However, the rapid recent improvement in photonic device technology has demonstrated several photonic ADC techniques that can outperform their electronic counterparts, whilst the massive growth of the integrated photonics market and the corresponding improvement in photonic integrated circuit fabrication techniques offers promise that photonic ADCs can be integrated and retain a small footprint. A comprehensive overview of photonic ADCs is provided by Valley [6]. Although now outdated, Valley's review still showcases the main concepts that have been evaluated for photonic ADCs in the literature.

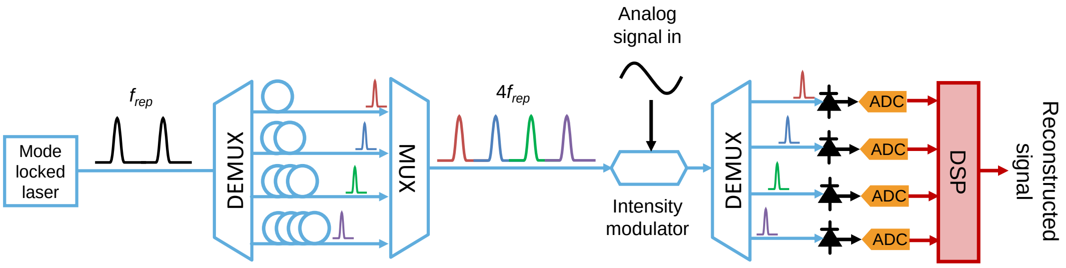

Fig. 2.10: A time interleaving photonic ADC concept, as demonstrated in [48].

Photonic ADCs can be broadly categorised according to whether the photonic devices are employed to perform or enhance the sampling or quantisation functions, or both. Since the primary distinction between electronics and photonics is frequency, the majority of and most successful ADC designs have focussed on incorporating photonics into the the sampling function. This can range from simply driving the ADC sampling gates with the low jitter optical source [49], to more complicated designs in which an optical preprocessor is used to either replicate or stretch the radio frequency (RF) signal in the optical domain [50, 51]. Single shot designs with the time stretching technique can achieve extremely high effective sampling rates of up to 10 TSa/s [52], but are restricted in their sampling rates when scaled to continuous operation. Many of the most successful photonic sampling designs can simply be considered as time to wavelength mappers that then exploit dense wavelength demultiplexers to effectively channelise the signal to the sub-rate ADCs in a time-interleaving concept [48], as shown in Fig. 2.10.

Significantly less explored is the concept of performing frequency interleaving in the optical domain. Although the concept of using optics to channelise RF signals in the frequency domain has been demonstrated using one or multiple frequency combs [53, 54, 55, 56, 57], literature investigating its use for improving ADC performance is limited. Two demonstrations of frequency interleaved photonic ADCs have been identified although the experimental demonstrations were extremely limited and recorded performances poor [58, 59]. Although [58] claims 6 bits ENOB at 40 GHz, the data presented contradicts the SNR calculation which suggests that the actual ENOB achieved was less that 2 bits. Furthermore, the sub-band detection technique prohibits full reconstruction of an arbitrary signal within each sub-band and therefore cannot scale to the full bandwidth without modification.

A relatively small body of research has explored implementing the quantisation function with photonics. In this concept, an electronic sample and hold circuit produces a staircase voltage waveform which then modulates the wavelength of a wavelength tunable laser. A grating or other diffractive element can then be used to quantise the laser output which can either be kept in the optical domain or converted back to RF. The resolution of such a scheme is defined by the number of resolvable wavelength bands and is severely hampered by the response time and nonlinearities in the wavelength tunable laser [60, 61].

Finally, some photonic ADCs aim to implement both sampling and quantisation in the optical domain and are sometimes referred to as all-optical ADCs. The oldest such ADC design was first proposed by Taylor [62] in 1975 and spawned a smorgasbord of variations that have been produced in the 40 years since [63, 64, 65, 66, 67, 68, 69]. The basic principle is that a bank of modulators with lengths differing by a factor of two can be assigned to each bit in the ADC ouput and driven by the input signal of interest. Correct biasing of the modulators and determination of the threshold intensity of each bit can then yield a quantised optical output. Despite the significant body of work dedicated to Taylor's design, resolutions of above 4 bits have yet to be achieved due to the large half wave voltage (known as V_π) needed to switch the modulators.

Another full optical approach investigates implementing the fundamental building block of an ADC, the comparator, in the optical domain. Many optical devices and techniques exist that can implement the comparator function (e.g. saturable absorber, symmetric self electro-optic devices and nonlinear effects) [70, 71, 72, 73, 74], yet optical comparator designs are often inhibited by device response time or inability to scale to the sufficient number of levels required for high resolution digitisation.

The best performing photonic ADCs in the literature are plotted against the best performing high speed electronic ADCs in Fig. 2.11. Note that all the photonic results presented in Fig. 2.11 were obtained in undersampling mode, since the the authors likely did not have access to the required number of sub-ADCs to perform full bandwidth detection. Impressive results have also been obtained for high frequency sub-sampling designs, yet it is not clear how these can be scaled to full bandwidth operation [81, 82,

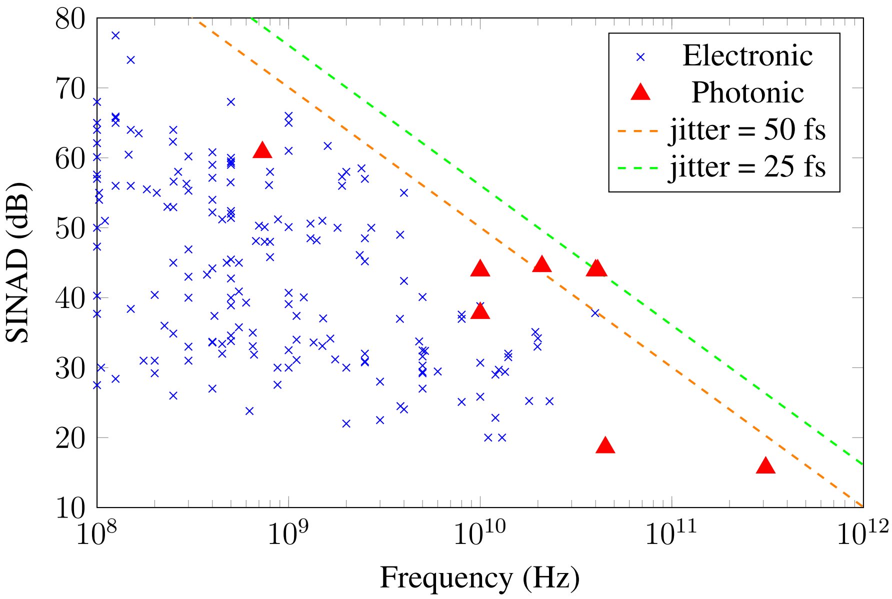

Fig. 2.11: SINAD vs input frequency for selected photonic ADCs reported in the literature [48, 75, 76, 77, 78, 79, 80, 58, 56], compared to the best performing electronic ADCs reported at ISSCC and the VLSI symposium from 1997-2021 [24]. Theoretical limits imposed by clock jitters of 25/50 fs are also plotted.

83].

The most impressive results are [48] and [79] which achieve 15 fs equivalent jitter, exceeding the current limit for electronic ADCs of 50 fs as shown in Fig. 2.6. Note that scaling [79] to full wideband operation however would require an extensive network of modulators that would likely impact its performance at full bandwidth. Aside from the impressive headline figures, [48] also performs restitching of two time interleaved channels and demonstrates that the electronic mismatch compensation techniques can be successfully applied to photonics.

2.4 Subsystems for Photonic ADCs

2.4.1 Optical frequency combs

A key aspect of the approach proposed within this thesis is the generation of low noise optical frequency combs. An optical frequency comb is a laser whose spectrum consists of a series of evenly spaced discrete coherent frequency tones. That is, an electromagnetic field described by

$$E(t) = \sum_{n=-N}^{N} A_n e^{i2\pi(f_0+nf_{rep})t}, \tag{2.22}$$

where f_0 is the central frequency and f_{rep} is the spacing between the comb lines in the frequency domain, as illustrated in Fig. 2.12. In the time domain, this is a series of optical pulses centred at frequency f_0 with a repetition rate of $1/f_{rep}$. The precise shape and width of these pulses in the time domain depends on the number of comb lines, N and their precise amplitude A_n and relative phase. The usefulness of such an optical source is derived from the fact the precise spacing of these frequency components provides a link between radio frequencies (RF), represented by f_{rep}, and optics, represented by f_0, by referencing to itself or another comb source [84, 85]. It is this attribute that led to the wide deployment of combs in precision spectroscopy, metrology and photonic RF signal processing, while the mutual coherence of the comb lines offers significant advantages over a simple bank of lasers with uncorrelated noise in applications that require a multi-wavelength source [86, 87, 88].

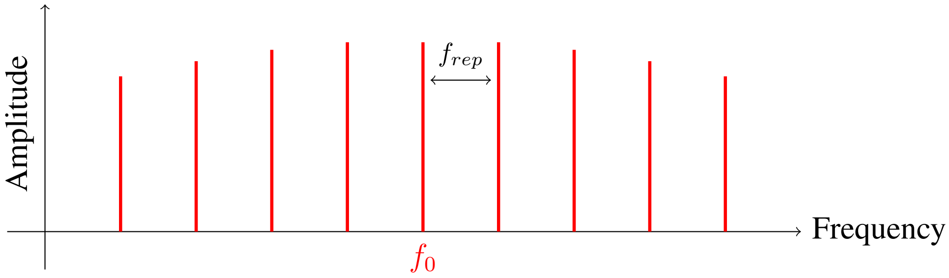

Fig. 2.12: Optical frequency combs are light sources that consist of a series of evenly spaced coherent optical frequencies $f_0 + nf_{rep}$, with central optical frequency f_0.

Perhaps the most widespread source of frequency combs is the mode-locked laser. In fact, the concept of mode locking was first established in the frequency domain, with the realisation that constructing ultra short pulses in the time domain required the phase locking of multiple longitudinal laser cavity modes [89]. In a mode-locked laser, the frequency comb spacing is essentially determined by the round trip cavity time, and is therefore not usually tunable over a wide range once the laser is constructed [90]. This, along with low repetition rate and need for lossy equalisation of the comb lines generally limits the use of mode locked lasers for many RF photonic applications [87].

A more recently studied method for frequency comb generation is through the third order nonlinear process of four wave mixing, which is illustrated in Fig. 2.13. Four wave mixing can occur if at least two different frequency components propagate through a nonlinear medium, where a refractive index modulation occurs at the difference frequency. This causes new frequency components to be generated spaced at the difference frequency from the original components, which in turn can create more components by further four wave mixing. In this way, an entire frequency comb can be created by cascaded four wave mixing of two CW laser sources. The most obvious way of generating a frequency comb through four wave mixing is simply by launching these two laser sources into a highly nonlinear fibre (HNLF) [91, 92]. However, care must be taken to ensure that the phase noise in the two seed tones is correlated, for example by using a electro optic comb as seed, to prevent excessive degradation of the outer tones linewidth [93]. As an alternative to HLNF, many have investigated the use of highly nonlinear waveguides to generate broadband frequency combs with a much smaller device footprint, example materials include aluminium-gallium-arsenide-on-insulator [94, 95], chalcogenide glass [96] and silicon [97]. Many of these devices however suffer from poor coupling loss due to their rectangular waveguide nature or mode field mismatch, which is often polarisation or wavelength dependent [98].

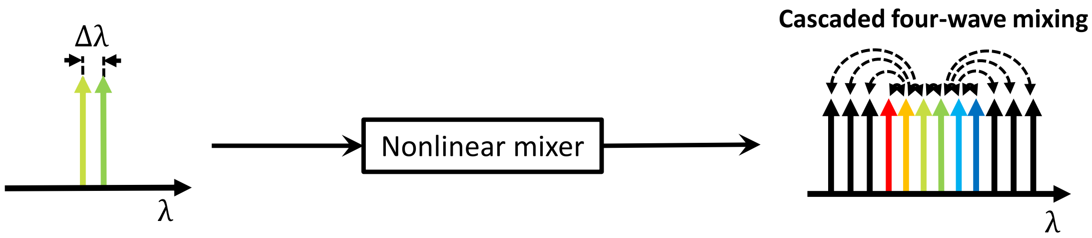

Fig. 2.13: Broadband optical frequency combs can be generated by pumping a nonlinear waveguide with a multi-wavelength source. New frequency components are generated through cascaded four wave mixing.

Effective cascaded four wave mixing can also be achieved by confining light in micro ring resonators [99, 100]. The extremely high Q-factors of these resonators leads to long interaction lengths and enhanced non-linearity, with low thresholds for nonlinear processes, leading to effective comb generation with a small device footprint. Since the four-wave mixing products will be generated at the ring cavity modes, the spacing of the comb will be determined by the free spectral range (FSR) of the cavity, with the bandwidth of the comb limited by dispersion causing the FSR to deviate from the comb spacing at high and low frequencies. The compact nature of microresonator comb sources offers promise of highly integrated and portable comb based devices with high bandwidth [101, 94], although achieving the required optical signal to noise ratio (OSNR) and frequency stability required for many signal processing applications is a significant challenge [102].

A more robust and flexible approach to frequency comb generation is through the modulation of a continuous wave laser source with electro-optic modulators. Since the spacing is determined by the modulator driving frequency, the spacing can be easily adjusted by changing the driving frequency, whilst the wavelength and phase noise characteristics (i.e. linewidth) of the comb lines will be inherited from the seed laser. Furthermore, such frequency combs can be equalised by the use of cascaded phase and intensity modulators [103], as shown in Fig. 2.14. In this scheme, the phase modulator can be seen as a time to frequency converter (or time lens) that maps the shape of a train of flat topped pulses to the frequency domain, with the square pulses being generated by the intensity modulator [104]. The number of tones generated is directly dependent on the amplitude of the phase modulation, whilst the flatness of the comb is dependent on accurate square pulse generation and ensuring that the phase modulation oscillates around the pulse centre. The robustness and simplicity of electro-optic comb generation schemes has made them the comb source of choice for photonic RF signal processing [7].

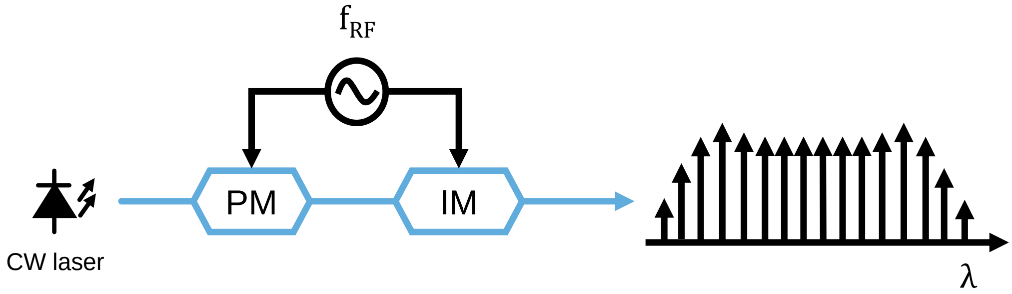

Fig. 2.14: Flat electro-optic combs can be generated by cascading a continuous wave (CW) laser source with cascaded phase and intensity modulators.

2.4.2 Oscillator phase and amplitude noise

The previous section described how optical frequency combs are essentially composed of two oscillations in the optical and radio frequencies. In (2.22) however, we assumed that the optical and radio oscillations, f_0 and f_{rep} respectively, were perfect and did not exhibit any noise. In reality, the quality of an oscillator is of course defined by how well it can track this perfect sinusoid, with fluctuations in phase and amplitude

$$x(t) = A_0(1 + \alpha(t))e^{i(\omega_0 t + \phi(t))}. \tag{2.23}$$

The phase noise $\phi(t)$ is typically much more of a concern for high quality oscillators since saturation effects do not prevent its propagation through the entire system. Indeed, the phase error $\phi(t)$ can accumulate indefinitely and cause large divergence from $\phi(t) = 0$, given enough time. Slow fluctuations in $\phi(t)$ especially will easily propagate through complex optical or electronic systems if not accounted for.

The phase noise $\phi(t)$ is a random process and is most helpfully described by its one sided power spectral density $S_\phi(f)$ [19], which is the Fourier transform of the autocorrelation function $R_{\phi\phi}(\tau) = \mathrm{E}\left\{\phi(t)\phi(t+\tau)\right\}$

$$S_\phi(f) = \int_{-\infty}^{\infty} R_{\phi\phi}(\tau) e^{-i2\pi f\tau} d\tau \tag{2.24}$$

$$= \int_{-\infty}^{\infty} \mathrm{E}\left\{\phi(t)\phi(t+\tau)\right\} e^{-i2\pi f\tau} d\tau \tag{2.25}$$

and is fully equivalent to the phase-time power spectral density $S_x(f)$ of $x(t)$ by the simple relation

$$S_x(f) = \frac{1}{\omega_0^2} S_\phi(f) \tag{2.26}$$

which follows immediately from (2.23). Alternatively, $S_\phi(f)$ can be defined via the finite-time Fourier transform of $\phi(t)$, $\phi(f)$

$$S_\phi(f) = \mathrm{E}\left\{\lim_{T\to\infty} \frac{1}{T} |\phi(f)|^2\right\} \tag{2.27}$$

for measurement time T. For simplicity the notation

$$S_\phi(f) = |\phi(f)|^2 \tag{2.28}$$

can be used. For historical reasons, phase noise is most commonly reported as

$$\mathscr{L}(f) = \frac{1}{2} S_\phi(f) \tag{2.29}$$

as suggested by the IEEE standard [105]. For theoretical analysis however, $S_\phi(f)$ is the more fundamental and intuitive quantity. Equivalently, the random fluctuations in phase $\phi(t)$ can be described instead as random fluctuations in frequency $\delta f(t)$. As frequency is the derivative of phase with respect to time, this leads to a multiplication by $i2\pi f$ in the Fourier transform and therefore multiplication by $(2\pi f)^2$ in the spectrum, leading to the relation

$$S_f(f) = f^2 S_\phi(f) \tag{2.30}$$

between the frequency noise power spectral density $S_f(f)$ and the phase noise power spectral density $S_\phi(f)$.

$S_\phi(f)$ is modelled typically as a power law function

$$S_\phi(f) = \sum_{i=-\infty}^{0} b_i f^i. \tag{2.31}$$

Phase noise spectra are plotted as log-log plots, as in Fig. 2.15, with each f^i process appearing as a straight line of increasing slope with increasing i. The different i correspond to different physical processes within the oscillator, depending on the individual components and oscillator design. Typically, observed i are > -4 although higher order slopes are possible.

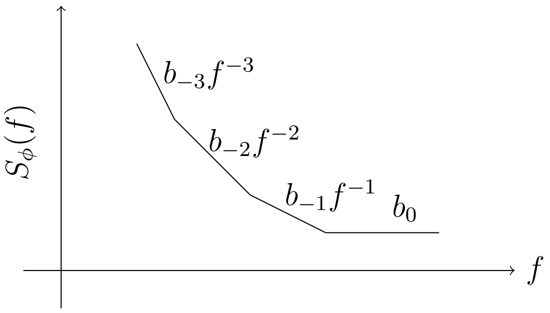

Fig. 2.15: Oscillator phase noise can be described by a number of power law segments that appear as straight lines on a log-log plot.

For a two port device such as an amplifier, white phase noise ($i = 0$) and flicker noise ($1/f$) are the main noise processes. Indeed, slopes steeper than $1/f$ are not possible in a two port device for $f \rightarrow 0$ since the group delay would diverge rapidly [19]. White phase noise is most predominately caused by shot/quantum noise and thermal noise, while flicker noise is ubiquitous in electronic amplifiers with a variety of origins [106].

Oscillators however have feedback, which can lead to the observation of the higher order slopes shown in Fig. 2.15. The boundary conditions enforced by the oscillator resonator converts the phase noise of the sustaining amplifier (i.e. the amplifier within the resonator) to frequency fluctuations at the oscillator output and consequently scales their slope by a factor $1/f^2$, in a phenomenon known as the Leeson effect [107, 108].

For example, in an electronic oscillator, the $1/f$ noise and white thermal noise of the sustaining amplifier are converted to $1/f^3$ and $1/f^2$ noise respectively at the oscillator output. On the other hand, in an optical oscillator (i.e. a laser) the white amplified spontaneous emission noise of the laser gain medium is converted to $1/f^2$ noise at the laser output.

For lasers, the phase noise is often specified by a single linewidth value, usually the full width half maximum. To extract the actual phase noise spectral density, it is often assumed that the phase noise only follows a $1/f^2$ function and has a corresponding Lorentzian line shape, as for example described by the modified Schawlow-Townes formula [109, 110] for the full width half maximum linewidth δf

$$\delta f = \frac{\pi h f_0 n_{sp}}{P 2\pi \tau_p}(1 + \alpha^2) \tag{2.32}$$

where f_0 describes the lasing frequency, τ_p is the photon lifetime, n_{sp} is the spontaneous emission factor, α is the linewidth enhancement factor and P is the total emission power. However it has been shown that lasers also exhibit $1/f^3$ phase noise [111, 110], which in semiconductor lasers is generally understood to be a result of coupling between the index of refraction and the fluctuations of charge carrier due to spontaneous emissions [109, 112]. With this in mind, the laser line shape is often better described by a convolution between a Lorentzian and Gaussian [113, 114, 115], known as a Voigt profile. The relation between lineshape and frequency noise is described in Appendix B, along with a defintion of the Voigt profile.

The amplitude noise $\alpha(t)$ is typically very small in high quality oscillators due to saturation effects in sustaining amplifiers and we can assume that the mean is close to the desired amplitude, i.e. $\langle\alpha(t)\rangle \approx 0$ [19]. Close-in noise in well designed oscillators tends to be dominated by phase noise, but the amplitude noise power spectral density $S_\alpha(f)$ can be described with the same power laws as phase noise as in (2.31), with typically $i \geq -2$ [116]. The contribution of amplitude noise is often limited to the wideband white noise in electronic oscillators, where it contributes an equal proportion along with phase noise. However, in some specific oscillators nonlinear processes can result in the conversion of amplitude to phase and frequency noise [117, 118].

In optical oscillators, i.e. lasers, amplitude noise is typically referred to in terms of relative intensity noise (RIN) which simply specifies the fluctuations ΔP in terms of power rather than amplitude

$$P(t) = \overline{P} + \Delta P \tag{2.33}$$

which has an associated single-sided power spectral density $S_I(f)$, normalised to the average power $\overline{P}$ [119]. For well designed lasers, fast fluctuations in amplitude are typically determined by shot noise, while the close-in amplitude noise is often dominated by pump fluctuations and a peak that is caused by relaxation oscillations [120]. For shot noise limited RIN the power spectral density is white and offset frequency independent

$$S_{I,sh}(f) = \frac{2hf_0}{\overline{P}} \tag{2.34}$$

for lasing frequency f_0.

2.4.3 Optical amplifiers

Amplification in optical systems can be achieved using an optical gain medium as a two port device without feedback. These can be either semiconductor based, referred to as semiconductor optical amplifiers (SOAs) or fibre based, the most common of which is the EDFA [121]. Nonlinear gain mechanisms such as Raman amplifiers are not discussed within this thesis, mainly as a result of their poor pump efficiency and challenges for integration.

EDFAs are ubiquitous in optical networks due to their wide bandwidth (≈ 5 THz in a typical C-band EDFA) and easy integration into fibre based networks. Although modern SOAs can exceed the gain bandwidth of EDFAs, their polarisation sensitivity and noise performance has generally precluded their wide deployment in optical networks. Since both SOAs and EDFAs use stimulated emission as their amplification mechanism, their principle source of noise is amplified spontaneous emission (ASE). ASE is an unavoidable quantum effect where spontaneous emission from the gain medium upper state is amplified to high power levels.

The noise performance of optical amplifiers is typically characterised by their noise figure [122, 123], which describes ratio of input to output SNR under the assumption that the input signal is shot noise limited

$$F = \frac{\mathrm{SNR}_{\mathrm{shot}}}{\mathrm{SNR}_{\mathrm{out}}}. \tag{2.35}$$

Shot noise in optical systems originates from the discrete nature of light, and its power spectral density can be related to the energy of an individual photon hf of frequency f by considering the so-called 'zero-point' fluctuations [124]

$$\rho_{\mathrm{shot}} = hf \tag{2.36}$$

where h is the Planck constant. From the definition of noise figure, (2.35), we can therefore also state the ASE power spectral density at the amplifier output for a shot noise limited input

$$\rho_{\mathrm{ASE}} = (GF - 1)hf. \tag{2.37}$$

Note that when detected on a photodetector, the dominant ASE noise term is the signal ASE beat, which is given by multiplying (2.37) by the input signal power. Both G and F are actually wavelength dependent, leading to a wavelength dependent ρ_{ASE}, but this wavelength dependence can be ignored over typical detection bandwidths (<100 GHz) and the ASE can be treated as a white noise.

Typical noise figures for EDFAs are 4-7 dB, while SOAs often have noise figures in the range 7-9 dB. It is often remarked that phase-insensitive amplifiers such as EDFAs cannot have a better noise figure than 2 (or 3 dB). However this is only true in the high gain limit $G \gg 1$, and EDFAs operating with low gain ($G < 10$) can readily achieve noise figures below this limit [125].

However, any integrated photonic device must make use of SOAs since fibre based amplifiers can obviously not be included in an photonic integrated circuit. When the photonic system is confined within a chip, the polarisation sensitivity is not an issue since the entire system is typically single polarisation but the increased noise performance compared to EDFAs cannot be avoided. EDFAs are used in the prototype designs presented within this thesis for practical purposes, and when assessing the system performance of an integrated designs the change in system losses and noise figure of any amplifiers must be considered.

2.5 Summary

This Chapter explained the fundamental functions and performance metrics of ADC and explored typical approaches to high speed ADCs in the literature. It was shown that the frequency interleaving approach to ADCs has less susceptibility to clock jitter than the more common time interleaving designs, yet their adoption is hindered by the difficulties associated with local oscillator distribution and electronic filter design. Previous photonic approaches to ADCs were discussed, with the best performing examples being based on exploiting the low jitter of mode locked lasers in a time interleaving design. Finally, important subsystems for the photonic ADC designs presented in this thesis were reviewed.

Chapter 3

Modelling and numerical analysis

This Chapter introduces the concept of using dual optical frequency combs as the front end for a frequency interleaving photonic ADC. Dual frequency combs were originally proposed and have been extensively explored for use in spectroscopy [85], and the general concept is outlined in Fig. 3.1. Two frequency combs, one of spacing f_{sig} ('signal comb') and one of spacing $f_{LO} = f_{sig} + \Delta f$ ('local oscillator (LO) comb') are generated, both centred at the region of interest in the optical spectrum. The comb spacings therefore differ by Δf. The signal comb is passed through the material (e.g. a gas) of interest so that its absorption spectrum is recorded across the entire bandwidth of interest. Then, the signal comb is mixed with the LO comb on a photodiode so that the beating between the n-th comb lines of each comb produce an RF comb at the photodiode output of spacing Δf. The amplitude and phase of these RF frequencies will be directly proportional to the product of the electric fields of the corresponding optical comb lines.

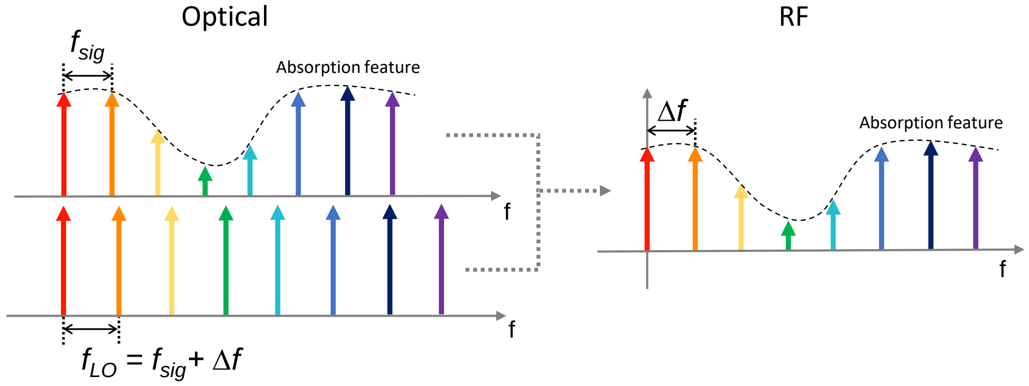

Fig. 3.1: Dual frequency comb spectroscopy concept. The absorption feature of a substance (e.g. a gas, liquid etc) is observed by passing an optical frequency comb ('signal comb') of appropriate wavelength with comb spacing f_{sig} through the substance. A second reference comb of spacing $f_{LO} = f_{sig} + \Delta f$ is then mixed with the signal comb on a photoreceiver. The beating between the two combs means that the absorption feature is down converted to RF frequencies $n\Delta f$ for rapid acquisition of broadband spectra.

In this way, the dual comb spectroscopy technique effectively maps the optical spectrum to an RF spectrum that is $f_{sig}/\Delta f$ times smaller, allowing for rapid acquisition on a low speed (e.g. <1 GHz) photodector provided that the two combs are phase stable. For spectroscopy, the compression factor $f_{sig}/\Delta f$ can be up to 10^6 utilising several hundred thousand comb teeth, allowing for the detection of tens to hundreds of THz using a 100 MHz photodiode. This is also known as the Vernier effect in analogy to its mechanical equivalent [126, 127].

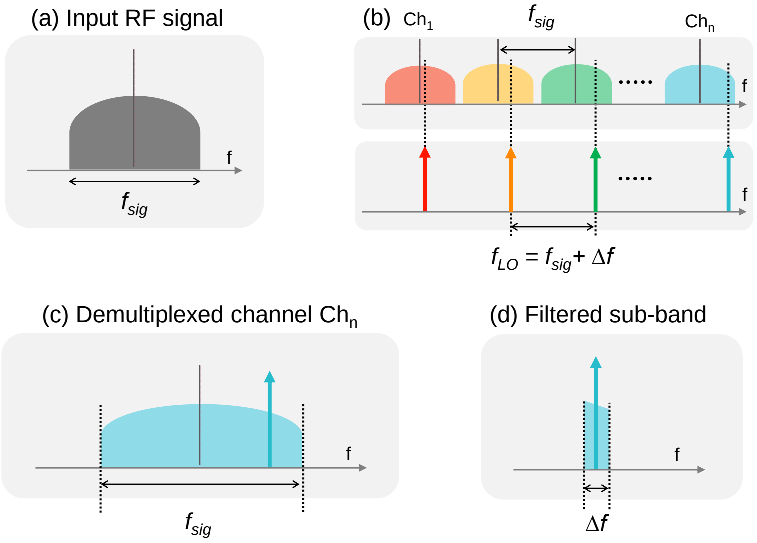

Fig. 3.2: Spectral slicing using dual optical frequency combs. (a) The input RF signal is (b) modulated onto a frequency comb of spacing f_{sig} that is mixed with a frequency comb of spacing $f_{LO} = f_{sig} + \Delta f$ to exploit the Vernier effect in the frequency domain. (c) The demultiplexed n-th channel, i.e. Ch_n in (b), (d) is coherently detected and filtered in parallel with the other channels to obtain a Δf slice of the input signal.

The dual frequency comb concept can be adapted for RF signal processing, as illustrated in Fig. 3.2. In the context of signal processing, the signal comb can be modulated with the input RF signal so that the input signal of interest is copied onto every comb line. This means that the local oscillator (LO) comb will act as a set of local oscillators offset from the baseband of the original signal by $n\Delta f$ in the n-th comb line, provided that the comb lines of both frequency combs can be separated by an optical demultiplexer (e.g. an arrayed waveguide grating of bandwidth f_{sig}) for parallel coherent reception. Ideally, the spacing of the optical demultiplexer should be matched to the LO comb spacing to prevent filter roll-off reducing the power of the detected signal in the higher channels.

The dual comb scheme can therefore act as channelizer [53], decomposing an RF signal into N spectral slices of bandwidth Δf. The use of optical frequency combs allows for low noise and distortion distribution of many local oscillators for a frequency interleaving ADC, while in contrast to single comb based channelisation schemes such as [56, 55], the dual comb approach allows for arbitrarily thin spectral slicing without the need for a correspondingly narrow wavelength demultiplexing device. In contrast to time interleaving systems, the frequency of the detected signal can be determined unambiguously even without all channel receivers being implemented, since the filtering function unambiguously determines the range of frequency content within each channel.

As with all interleaving based ADC schemes, achieving effective massive parallelisation will be a significant implementation challenge for dual comb based ADCs. However, this does not seem like a fundamental obstacle given the ubiquity of the massive time-interleaving architecture for commercially available ADCs. Indeed, this parallelisation challenge should be mitigated for the dual comb ADC given the reduced susceptibility of channel mismatch errors for frequency interleaving designs [34, 37, 128], as discussed in Section 2.2.2.

In this thesis we investigate using this channelization scheme as the analog front end to create a frequency interleaving photonic ADC. Other reported demonstrations of dual frequency comb channelization for RF signal processing include sub-noise signal detection [129, 130], OFDM reception [131, 57], and wideband RF disambiguation of sparse signals [132], with a variety of comb generation techniques used including electro-optic modulation, parametric mixing and micro ring resonators.

3.1 Frequency to channel mapping

We first derive formulae for calculating which channel a given input frequency will fall into for a dual frequency comb channelizer system which is important for detailed analysis of the dual comb system. For a dual comb system with signal comb frequency ω_{sig} ($\omega_{sig} = 2\pi f_{sig}$) and spacing $\Delta\omega$, the input frequency ω (whether the desired input or subsequently generated harmonic), will fall into channel

$$m_{LO} = \left\lceil \frac{\left|\omega - \omega_{sig}\left\lceil \frac{\omega}{\omega_{sig}} \right\rfloor\right|}{\Delta\omega} \right\rfloor \tag{3.1}$$

where $\lceil x \rfloor$ denotes rounding x to the nearest integer, where half is rounded up. This means that it will be detected by the m_{LO}-th LO comb line, and will be carried by the m_{sig}-th signal comb line, given by

$$m_{sig} = \left| m_{LO} \pm (-1)^{\left\lceil \frac{\omega}{2\omega_{sig}} \right\rfloor} \left\lceil \frac{\omega}{\omega_{sig}} \right\rfloor \right|. \tag{3.2}$$

Where the ± accounts for whether the signal is detected using the positive or negative comb lines indices respectively. Note that for $\omega < \frac{\omega_{sig}}{2}$ this reduces to

$$m_{sig} = m_{LO} = \left\lceil \frac{\omega}{\Delta\omega} \right\rfloor . \tag{3.3}$$

The simplified formula (3.3) represents the scenario in which the input signal does not contain any frequency components above the Nyquist frequency of the dual comb ADC, which could be assured by placing a low pass filter with a cutoff at the Nyquist frequency before the input modulator. In this case, the formulae (3.1) are quite intuitive since each frequency component is carried by the n-th comb line when falling into the frequency band $n\Delta\omega - \frac{n\Delta\omega}{2} < \omega < n\Delta\omega + \frac{n\Delta\omega}{2}$, for both signal and LO combs.

However, there are many applications in which signals above the dual comb ADC Nyquist frequency may need to be detected. This is a common scenario in wireless and radar applications [133, 134], where narrowband signals are often modulated onto high frequency carriers. Furthermore, even if the use case can guarantee that no frequencies above the Nyquist frequency will be present at modulator input, the nonlinearity of the modulator will generate these higher than Nyquist frequencies, as is discussed later in this Chapter. In these scenarios, the LO comb line which detects the signal is simply the same as its 1st Nyquist zone alias, which (3.1) accounts for. The detected frequency component will then be carried by the signal comb line that is $k-1$ lines away from the corresponding LO comb line when the frequency falls into the k-th Nyquist zone, as is described by (3.2).

3.2 Noise and distortion analysis

Figure 3.3 shows a generic dual frequency comb RF channelizer architecture with noise and distortion sources highlighted. Two optical frequency combs with angular frequency spacing ω_{sig} and ω_{LO} are generated, one of which is modulated with the input signal, before individual comb lines are filtered optically. Each sub-channel can then be detected by a low speed coherent receiver and filtered to the subchannel bandwidth Δf by low pass filters, followed by signal processing and digitisation. Note that for the numerical results presented in this Chapter, we use cascaded phase and intensity modulators to generate our frequency combs without loss of generality. The models presented here can be equally applied to other comb generating techniques, such as parametric and microresonator combs [99, 135, 136], provided that the phase noise characteristics of the device are known.

We consider four fundamental sources of noise and distortion as highlighted in Fig. 3.3, and label the SNR limits they impose:

1. **Frequency comb phase noise**, SNR$_{pn}$. Each generated frequency comb will have two independent sources of phase noise: the seed laser phase noise, $\phi_0(t)$,

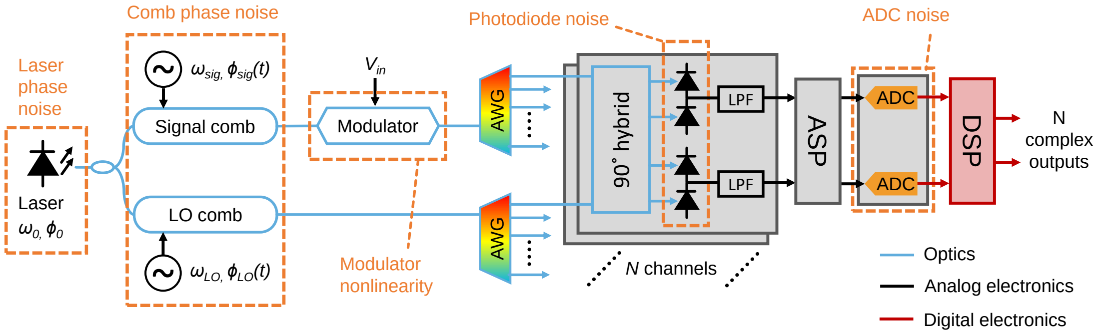

Fig. 3.3: A generic dual comb channelizer scheme, with noise and distortion sources highlighted. The LO comb and signal comb plus modulator paths are length matched to suppress the laser phase noise. Note that the order of the AWG and 90 degree hybrid may be switched. AWG, arrayed waveguide grating; ADC, analog to digital converter; LPF, low pass filter; ASP, analog signal processing; DSP, digital signal processing.

and the phase noise added during the comb generation, $\phi_{sig}(t)$ and $\phi_{LO}(t)$, for the signal and LO comb, respectively. We do not consider amplitude noise in either case since for most oscillators its impact is orders of magnitude lower than the phase noise [137] and can be effectively suppressed [138, 139].

2. **Photodiode noise**, consisting of shot (SNR_{sh}) and thermal (SNR_{th}) noise. Dark noise is negligible compared to the shot noise in the dual comb system since the photodiodes are always illuminated by the local oscillator comb.

3. **Modulator nonlinearity**, SNR_{mod}. The electro-optic modulator that maps the input signal onto the signal comb will have some degree of nonlinearity, depending on the modulator design and the driving conditions, that will cause harmonic distortion. Unlike the stochastic noise sources, this nonlinearity is deterministic and can be mitigated through highly linear modulator design or digital signal processing [140, 141, 142, 143, 144, 145].

4. **ADC noise**, SNR_{ADC}. Each sub channel will be ultimately limited by the ADC noise if it is digitised. At MHz sampling rates and above, ADCs are typically limited by quantisation noise and clock jitter induced sampling error [4].

These noise/distortion sources are independent and so can be calculated separately to determine the level of noise that each source contributes. Furthermore, since the modulator nonlinearity is deterministic, we separate it from the stochastic noise processes to firstly define the signal to noise ratio without harmonics (SNR)

$$\text{SNR} = \left(\text{SNR}_{pn}^{-1} + \text{SNR}_{sh}^{-1} + \text{SNR}_{th}^{-1} + \text{SNR}_{ADC}^{-1}\right)^{-1}. \tag{3.4}$$

The SNR limit imposed by harmonic distortions, SNR$_{mod}$, is often referred to as THD. Together SNR and THD result in a signal to noise and distortion ratio (SINAD), which is the key figure of merit thoughout this thesis

$$\text{SINAD} = \left(\text{SNR}_{pn}^{-1} + \text{SNR}_{sh}^{-1} + \text{SNR}_{th}^{-1} + \text{SNR}_{ADC}^{-1} + \text{SNR}_{mod}^{-1}\right)^{-1}. \tag{3.5}$$

3.2.1 Phase noise

We first analyze the phase noise limited SNR of the dual comb system shown in Fig. 3.3, considering only phase noise from the seed laser and the two comb generators. The output of a continuous wave laser with amplitude A_0, phase noise $\phi_0(t)$ and angular frequency ω_0 is given by

$$E_0(t) = A_0 e^{i(\omega_0 t + \phi_0(t))}. \tag{3.6}$$

A frequency comb can be generated using a multitude of different approaches. For example, in our previous demonstration the combs were generated by modulating the laser output [103, 8], yielding phase noise that scales linearly with number of tones [146]. Note that this is the general property of a number of comb generation approaches including parametric combs and microresonator combs [147]. Consequently, we can assume without losing generality that the added phase noise to the n-th tone of the signal and LO combs are $n\phi_{sig}(t)$ and $n\phi_{LO}(t)$, respectively, where $\phi_{sig}(t)$ and $\phi_{LO}(t)$ is the comb phase noise (i.e. the repetition rate phase noise) for the signal and LO comb respectively. The angular frequency between adjacent tones is $\omega_{sig}, \omega_{LO}$. This results in the optical field of the signal and LO combs for frequency combs with $2N + 1$ tones being

$$E_{sig}(t) = \sum_{n=-N}^{N} \sqrt{P_{sig,n}} e^{i((\omega_0 + n\omega_{sig})t + \phi_0(t) + n\phi_{sig}(t))}, \tag{3.7}$$

$$E_{LO}(t) = \sum_{n=-N}^{N} \sqrt{P_{LO,n}} e^{i((\omega_0 + n\omega_{LO})t + \phi_0(t) + n\phi_{LO}(t))} \tag{3.8}$$

where $P_{sig,n}$, $P_{LO,n}$ is the power of the n-th line in the signal comb and local oscillator comb respectively. Any loss in the optical paths can be accounted for by reducing the value of P_{sig} and P_{LO}. As per the dual comb RF signal processor shown in Fig. 3.3, the signal comb $E_{sig}(t)$ is passed through a Mach Zehnder modulator

(MZM) biased at the null that is modulated with the RF signal under test. Initially, we treat the dual comb channelizer as a linear time invariant system and consider the case of a sinusoidal input

$$V_{in}(t) = A_{in} \sin \omega_{in} t \tag{3.9}$$

and assume that the transfer function of the modulator, $M(V_{in}(t))$, is linear,

$$M(V_{in}(t)) = \sin\left(\frac{\pi V_{in}(t)}{V_\pi}\right) \approx \frac{\pi V_{in}(t)}{V_\pi}. \tag{3.10}$$

This is a valid approximation for a Mach-Zehnder modulator biased at the null if $V_{in} \ll V_\pi$, and we ignore insertion loss since this can be accounted for by a reduction in P_{sig}. Every comb line is therefore modulated with the input signal scaled by the amplitude of the input signal and relative to the V_π of the modulator

$$\frac{\pi A_{in}}{V_\pi} \sin \omega_{in} t \cdot E_{sig} = \frac{\pi A_{in}}{V_\pi} \sin \omega_{in} t \sum_{n=-N}^{N} \sqrt{P_{sig,n}} e^{i((\omega_0 + n\omega_{sig})t + \phi_0(t) + n\phi_{sig}(t))}. \tag{3.11}$$

Now both frequency combs are optically filtered using an arrayed waveguide grating or other method of spacing ω_{LO} so that each comb line is separated for both frequency combs, and the n-th comb lines from each frequency comb can then be used as the inputs for an ideal optical coherent receiver. Assuming that the signal and LO paths are length matched, the balanced receivers yield the output currents

$$I_{I,n}(t) = R\sqrt{P_{sig,n} P_{LO,n}} \frac{\pi A_{in}}{V_\pi} \sin \omega_{in} t \cdot \operatorname{Re}\left\{ e^{-in(\Delta\omega t + \phi_{LO}(t) - \phi_{sig}(t))} \right\}, \tag{3.12}$$

$$I_{Q,n}(t) = R\sqrt{P_{sig,n} P_{LO,n}} \frac{\pi A_{in}}{V_\pi} \sin \omega_{in} t \cdot \operatorname{Im}\left\{ e^{-in(\Delta\omega t + \phi_{LO}(t) - \phi_{sig}(t))} \right\} \tag{3.13}$$

where R is the responsivity of the photodiodes and defining $\Delta\omega = \omega_{LO} - \omega_{sig}$. This can be summed to produce the full sub-band signal for the n-th channel

$$I_{out,n} \propto I_{I,n} + i I_{Q,n} = R\sqrt{P_{sig,n} P_{LO,n}} \frac{\pi A_{in}}{V_\pi} \sin \omega_{in} t \cdot e^{-in(\Delta\omega t + \phi_{LO}(t) - \phi_{sig}(t))}. \tag{3.14}$$

If an ideal low pass filter (LPF) of bandwidth $\frac{\Delta\omega}{2}$ is applied to the I and Q components such that the frequency components $\omega_{in} + n\Delta\omega$ are eliminated, then the output in the n-th channel is

$$I_{out,n} \propto R\sqrt{P_{sig}P_{LO}}\frac{\pi A_{in}}{2V_\pi}e^{i(\omega_{in}-n\Delta\omega)t-n(\phi_{LO}(t)-\phi_{sig}(t))} \tag{3.15}$$

for $|\omega_{in} - n\Delta\omega| < \frac{\Delta\omega}{2}$. This is a complex valued sinusoid that is the analytic representation of the original input V_{in}, shifted in frequency by $-n\Delta\omega$ in the n-th sub-band and scaled by a constant, which will also include any gain experienced during the current to voltage conversion process. Essentially, the n-th channel detects all frequencies in the range $n\Delta\omega \pm \frac{\Delta\omega}{2}$.

This output signal has phase noise that is equal to the relative phase noise between the two corresponding comb lines, denoted $\Delta\phi_n(t) = n(\phi_{LO}(t) - \phi_{sig}(t))$. Since $\Delta\phi_n(t)$ is small we can use the truncated Taylor expansion of e^x to write

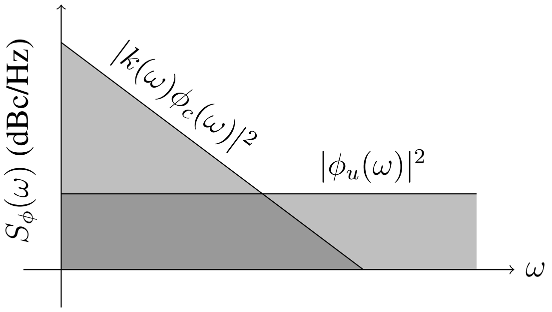

Fig. 3.4: Representative phase noise spectrum (ω plotted in log scale) of a given frequency comb pair in a dual comb system. The phase noise will consist of two parts: a correlated part $\phi_c(\omega)$ transformed by some function $k(\omega)$, and an uncorrelated part $\phi_u(\omega)$.

$$e^{i(\omega_{in}-n\Delta\omega)t-\Delta\phi_n(t))} \approx (1 - i\Delta\phi_n(t))e^{i(\omega_{in}-n\Delta\omega)t} \tag{3.16}$$

and can see that the total noise power resulting from the relative phase noise for n-th tone is

$$\frac{1}{\mathrm{SNR}_{pn}} = \overline{\Delta\phi_n^2} = 2\int_0^{\frac{\Delta\omega}{2}} S_{\Delta\phi_n}(\omega)\mathrm{d}\omega \tag{3.17}$$

where $S_{\Delta\phi_n}(\omega)$ is the one sided power spectral density of $\Delta\phi_n$ which describes the spectral distribution of the down converted carrier in the n-th channel [105], defined as

$$S_{\Delta\phi_n}(\omega) = |n(\phi_{LO}(\omega) - \phi_{sig}(\omega))|^2 \tag{3.18}$$

as per (2.27) and is integrated to the channel bandwidth [20] in (3.17). This phase noise spectrum contains contributions from both combs, so will depend on the phase noise level on each comb and how well this noise is correlated. If the frequency combs are uncorrelated, then the $\phi_{LO}(\omega)$ and $\phi_{sig}(\omega)$ are considered as independent phase noise and the power of the total phase noise is a simply sum of the two independent noise powers. However in this thesis, we consider the fact that the phase noise of the two combs is likely to be correlated to some degree, and write them as being composed of a correlated part $\phi_c(\omega)$ and uncorrelated parts $\phi_{u,LO}(\omega)$ and $\phi_{u,sig}(\omega)$

$$\phi_{sig}(\omega) = k_{sig}(\omega)\phi_c(\omega) + \phi_{u,sig}(\omega), \tag{3.19}$$

$$\phi_{LO}(\omega) = k_{LO}(\omega)\phi_c(\omega) + \phi_{u,LO}(\omega) \tag{3.20}$$

where $k_{sig}(\omega)$, $k_{LO}(\omega)$ are functions describing the mapping of the correlated phase noise component between the repetition rate of each frequency comb [148]. This description is illustrated in Fig. 3.4. For example, if each comb is generated by electro-optic modulation using sinusoidal signals referenced to the same oscillator through an ideal phase locked loop (PLL) based synthesizer, $k_{sig}(\omega)$ and $k_{LO}(\omega)$ are simply equal to the PLL counter setting with any noise added by the PLL itself (or subsequent amplifiers) contributing to the uncorrelated parts $\phi_{u,sig}(\omega)$, $\phi_{u,LO}(\omega)$. Plugging this into (3.18) gives

$$S_{\Delta\phi_n}(\omega) = n^2\Big[|k_{LO}(\omega) - k_{sig}(\omega)|^2|\phi_c(\omega)|^2 + |\phi_{u,LO}(\omega)|^2 + |\phi_{u,sig}(\omega)|^2\Big]. \tag{3.21}$$

The phase noise power in the n-th channel consists of three parts: the correlated phase noise scaled by some factor $|k_{LO}(\omega) - k_{sig}(\omega)|^2$ describing the relationship between the two comb synthesizers, and two contributions from the uncorrelated phase noise of the comb generators, all scaled by the square of the channel number n^2. For the purpose of our analysis, we further define the relative root-mean-square jitter in seconds σ_j

$$\sigma_j = \sqrt{\left(\frac{\overline{\Delta\phi_c}}{\Delta\omega}\right)^2 + \left(\frac{\overline{\Delta\phi_{u,sig}}}{\omega_{sig}}\right)^2 + \left(\frac{\overline{\Delta\phi_{u,LO}}}{\omega_{LO}}\right)^2} \tag{3.22}$$

which expresses the phase noise power (3.17) in seconds rather than radians, by summing the correlated and uncorrelated phase noise power contributions.

The extent to which the phase noise can be correlated is highly dependent on the comb synthesis technique. If each comb is generated by electro-optic modulation, then the driving signals are likely to be generated from the same reference oscillator through a phase locked loop (PLL) based synthesizer. In this case, the close-in phase noise (i.e. within the PLL loop bandwidth) will likely exhibit strong correlation [148], becoming uncorrelated at higher frequencies from carrier, where the phase noise will be contributed mainly from the internal circuitry of the synthesizer. Parametric combs seeded from electro-optic combs will generally exhibit similar characteristics [93].

On the other hand, frequency combs synthesised in microcavity resonators derive their phase noise (in addition to the pump laser phase noise) primarily from the thermorefractive fluctuations of the resonator [149, 150]. Furthermore, optical-to-RF noise conversion via higher order chromatic dispersion and the frequency dependent quality factor of the resonator may facilitate additional decoherence of the comb lines [151].

Note that our phase noise analysis from (3.11)-(3.15) can be extended to any arbitrary input up to the channelizer bandwidth, by representing the input signal as the sum of its Fourier components

$$V_{in}(t) = \frac{a_0}{2} + \sum_{p=1}^{P} (a_p \cos(\omega p t) + b_p \sin(\omega p t)) \tag{3.23}$$

given that the duration $2\pi/\omega$ is finite and that $P < \frac{\omega_{sig}}{2\omega}$. Each channel will detect a sub-band of the input signal so it is simpler to split the input signal into each sub-band

$$V_{in}(t) = \frac{a_0}{2} + \sum_{n=0}^{N} \sum_{p=(n-\frac{1}{2})\frac{\Delta\omega}{\omega}}^{(n+\frac{1}{2})\frac{\Delta\omega}{\omega}} (a_p \cos(\omega p t) + b_p \sin(\omega p t)) \tag{3.24}$$

and the photodiode noise equations (3.33)/(3.34) can be modified by replacing of the mean power the sine wave, $\frac{A_{in}^2}{2}$, with

$$\frac{A_{in}^2}{2} = \sum_{p=(n-\frac{1}{2})\frac{\Delta\omega}{\omega}}^{(n+\frac{1}{2})\frac{\Delta\omega}{\omega}} \left[\frac{a_p^2}{2} + \frac{b_p^2}{2} \right] \tag{3.25}$$

which is simply the signal power within each sub-channel.

3.2.2 Optical path length mismatch

We have implicitly assumed in (3.12)/(3.13) that the optical path length of each comb is matched and therefore that the laser phase noise $\phi_0(t)$ will be perfectly cancelled at the coherent receiver. In reality, some amount of path length mismatch may occur. Consider that one of the optical paths in the dual comb arrangement is mismatched from the other by length ΔL, corresponding to a time delay of $\Delta T = \Delta L \frac{n_{\text{eff}}}{c}$, for a refractive index of n_{eff}. This means that the laser phase noise on each path will be $\phi_0(t)$ and $\phi_0(t + \Delta T)$ and instead of perfect cancellation at the coherent receiver as assumed earlier, the relative phase noise between the two branches will be

$$\Delta\phi_0(t) = \phi_0(t) - \phi_0(t + \Delta T). \tag{3.26}$$

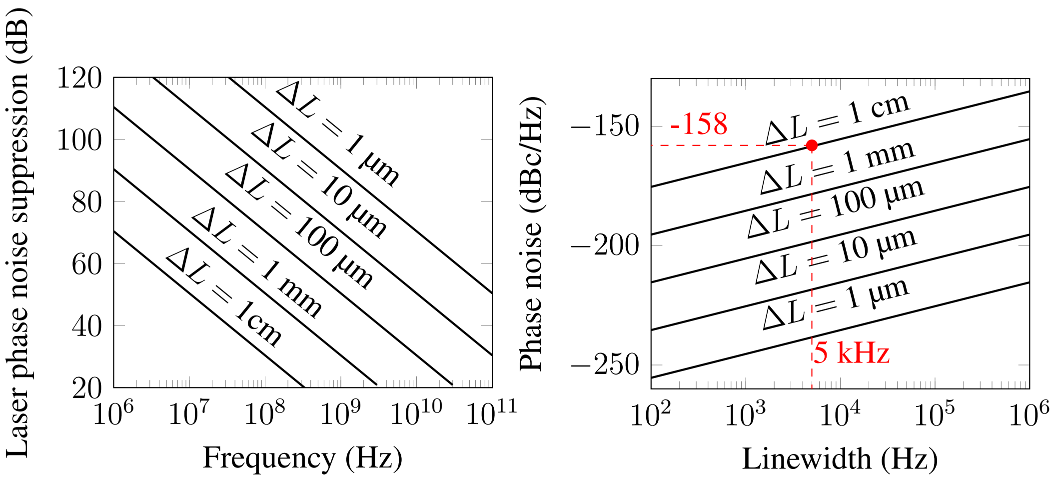

Fig. 3.5: (a) Laser phase noise suppression (3.30) as a function of offset frequency, for $n_{\text{eff}} = 1.44$. (b) Residual laser phase noise at the coherent receiver as a function of laser linewidth assuming a random walk. A 5 kHz linewidth example giving -158 dBc/Hz at 1 cm length mismatch is labelled in red.

The observed power spectral density, $S_{\Delta\phi_0}(f)$, of this relative phase noise is related to its autocorrelation,

$$\begin{aligned} R_{\Delta\phi_0\Delta\phi_0}(\tau) &= \mathrm{E}\left\{\Delta\phi_0(t)\Delta\phi_0(t+\tau)\right\} && (3.27)\\ &= 2R_{\phi_0\phi_0}(\tau) - R_{\phi_0\phi_0}(\tau+\Delta T) - R_{\phi_0\phi_0}(\tau-\Delta T), && (3.28) \end{aligned}$$

by the Fourier transform

$$\begin{aligned} S_{\Delta\phi_0}(f) &= 2S_{\phi_0}(f) - e^{i\omega\Delta T}S_{\phi_0}(f) - e^{-i\omega\Delta T}S_{\phi_0}(f) && (3.29)\\ &= \left[2 - 2\cos(\omega\Delta T)\right]S_{\phi_0}(f), && (3.30) \end{aligned}$$

where $S_{\phi_0}(f)$ is the Fourier transform of $R_{\phi_0\phi_0}(\tau)$ which is the power spectral density of the original laser phase noise. Essentially, one branch will experience a time delay (phase rotation) that decorrelates the phase noise between the two branches and converts it to intensity noise at the coherent receiver. The amount of phase rotation is dependent on the offset frequency and ΔT, with the original laser phase noise power spectral density suppressed by the factor $2 - 2\cos(\omega\Delta T)$ in (3.30). The suppression factor is plotted in Fig. 3.5(a) as a function of offset frequency for a variety of length mismatches.

This laser phase noise suppression can be applied to the power spectral density of the laser phase noise to determine the phase noise power spectral density at the coherent receiver caused by the laser phase noise. To illustrate this, we can use the common approximation that the laser phase noise single sided power spectral density follows a random walk [152]

$$S_{\text{laser}}(f) = \frac{\delta\nu}{\pi f^2} \tag{3.31}$$

where $\delta\nu$ is the laser linewidth. Multiplying (3.31) by the suppression factor (3.30) will result in a white phase noise at the coherent receiver, which is plotted in Fig. 3.5(b) versus linewidth for a variety of length mismatches. Even for a 1 cm mismatch (typical in a discrete component system) at 5 kHz linewidth, the laser phase noise level is at -158 dBc/Hz, implying a SINAD limit of 68 dB across for example 1 GHz bandwidth. Furthermore, any time-dependent optical path length mismatches induced by temperature and mechanical vibrations can be minimised by using an integrated platform or using active phase stability techniques [153, 154].

3.2.3 Photodiode noise

Before calculating the photodiode noise limited SNR expressions, we first give the signal power of the output (3.15)

$$P_{out} = \frac{R^2 P_{sig,n} P_{LO,n} \pi^2 A_{in}^2}{4V_\pi^2}. \tag{3.32}$$

We can assume that $P_{sig} \ll P_{LO}$, since the loss in the signal branch (modulation loss and modulator insertion loss) ensures that the local oscillator comb power is significantly higher than the signal comb and so is the dominant source of shot noise. This allows for the calculation of shot noise limited SNR, where q is the elementary charge

$$\text{SNR}_{sh} \approx \frac{R\pi^2 A_{in}^2}{4V_\pi^2} \frac{P_{sig,n}}{q\Delta f}. \tag{3.33}$$

This is just the standard coherent receiver shot noise limit with the mean modulated signal power [155]. We can also write the thermal noise limited SNR

$$\text{SNR}_{th} = \frac{R^2 P_{sig,n} P_{LO,n} \pi^2 A_{in}^2 R_L}{8k_B T \Delta f V_\pi^2} \tag{3.34}$$

where R_L is the load resistance, k_B is the Boltzmann constant and T is the temperature in Kelvin. This gives the thermal noise limited SNR. Since the thermal noise power does not depend on the optical power, thermal noise limits the SNR when the optical power is low.

3.2.4 Modulator linearity

In (3.11), we approximated the modulator transfer function as linear. To determine how hard we can drive the modulator before we experience appreciable generation of harmonics we need to consider the actual nonlinear transfer function of a Mach-Zehnder modulator biased at the null, which is a sinusoid $M(V_{in}(t)) = \sin\left(\frac{\pi V_{in}(t)}{V_\pi}\right)$. For a single sinusoid input, multiplying E_{sig} by the full transfer function and using the Jacobi-Anger expansion gives

$$M(V_{in}(t))E_{sig} = 2\sum_{j=1}^{\infty} J_{2j-1}\Big(\frac{\pi A_{in}}{V_\pi}\Big)\sin[(2j-1)\omega_{in}t] \tag{3.35}$$

where $J_{2j-1}(z)$ is the $(2j-1)$-th Bessel function of the first kind. This represents the generation of the odd harmonics, $3\omega_{in}, 5\omega_{in}, 7\omega_{in}$...etc in addition to the original frequency ω_{in}. Relative to the fundamental, these harmonics will have amplitude

$$A_{(2j-1)\omega_{in}} = \frac{P_{sig,m_{sig}}P_{LO,m_{LO}}}{P_{sig,n_{sig}}P_{LO,n_{LO}}}\frac{J_{2j-1}\big(\frac{\pi A_{in}}{V_\pi}\big)}{J_1\big(\frac{\pi A_{in}}{V_\pi}\big)} \tag{3.36}$$

where n_{LO} and m_{LO} represent the channel (and therefore LO comb line) that the fundamental and $(2j-1)$-th harmonic respectively fall into, while n_{sig} and m_{sig} represents the signal comb lines that carry the fundamental and $(2j-1)$ th harmonic respectively, which may not equal the channel number if frequencies above $\omega_{sig}/2$ are generated as defined by (3.1) and (3.2).

These additional frequency components will propagate through the dual comb system as described for the linear case (3.10)-(3.15). Harmonic-harmonic and harmonic-fundamental beating (i.e. signal-signal beating) will be eliminated at the coherent receiver. We can therefore estimate the relative power of the harmonics to the fundamental by squaring and summing (3.36) to obtain the total harmonic distortion (THD)

$$\text{THD} = \left(\sum_{j=1}^{\infty} A^2_{(2j-1)\omega_{in}}\right)^{-1}. \tag{3.37}$$

Assuming that the strongest harmonic is for $j = 2$ (true unless significantly overdriving the modulator) we can also estimate the SFDR, which we can use as the SNR limit due to modulator nonlinearity

$$\text{SNR}_{mod} = \text{SFDR} = \frac{1}{A^2_{3\omega_{in}}} = \frac{P_{sig,n}P_{LO,n}}{P_{sig,m}P_{LO,m}}\frac{J_1\big(\frac{\pi A_{in}}{V_\pi}\big)^2}{J_3\big(\frac{\pi A_{in}}{V_\pi}\big)^2} \tag{3.38}$$

observing that SFDR $\approx$ THD. It is clear from the shape of the Bessel functions in (3.38) that minimising A_{in} is required to maximise SFDR. Strictly speaking, we should also modify the shot and thermal noise limits by accounting for reduction in signal power due to modulator nonlinearity. This can be done by the simple substitution

$$\frac{\pi A_{in}}{V_\pi} = J_1(\frac{\pi A_{in}}{V_\pi}). \tag{3.39}$$

For more complex input signals, additional inter-modulation distortion products are generated. We therefore also consider the case of a two tone input

$$V_{in}(t) = \frac{A_{in}}{\sqrt{2}} \sin(\omega_1 t) + \frac{A_{in}}{\sqrt{2}} \sin(\omega_2 t). \tag{3.40}$$

Considering only third order distortion products, this will result in additional frequencies at $3\omega_1, 3\omega_2, 2\omega_1 - \omega_2, 2\omega_2 - \omega_1, 2\omega_2 + \omega_1, 2\omega_2 - \omega_1$ whose amplitudes can be calculated by considering the Taylor expansion of the modulator transfer function which is detailed in the Appendix. To determine the power of these products in the received signal, we multiply the square of the amplitudes by $R^2 P_{sig,m_{sig}} P_{LO,m_{LO}}$ where m_{sig}, m_{LO} are the calculated channel indices for the spurious tone, as calculated by (3.1) and (3.2). By comparing these noise powers to the received signal power, we can obtain the 3rd order intermodulation distortion (IMD3), and define $\text{SNR}_{mod} =$ IMD3 for the two tone case. As per the single tone case, the shot/thermal noise equations should be modified to include the new amplitudes of the fundamental.

3.2.5 ADC noise

Phase noise induced sampling error and quantisation error will be introduced within each channel when the sub-band is digitised. The maximum SNR at each sub-ADC will be given by

$$\text{SNR}_{ADC} = \left[((\omega_{in} - n\Delta\omega)\sigma)^2 + \frac{1}{3 \cdot 2^{2K-1}} \right]^{-1} \tag{3.41}$$

for jitter σ where $\omega_{in} - n\Delta\omega < \frac{\Delta\omega}{2}$ and K the number of bits [156]. In a practical system, it will make more sense to simply determine the ADC SNR limit from its stated effective number of bits, while accounting for any SNR enhancement through oversampling within the sub-band.

3.3 Numerical Simulation

To evaluate our theoretical estimates, we simulated single and two tone sine wave testing of an example channelizer. Two frequency combs were generated by modulating a seed laser via cascaded intensity and phase modulators as in [103] and

Parameter	Value	Parameter	Value
Number of samples	2^{24}	Seed laser power	37.5 dBm
Sample rate	2 THz	Number of channels, N	12
Signal comb spacing, f_{sig}	25 GHz	Demultiplex loss	4.8 dB
LO comb spacing, f_{LO}	26 GHz	Input modulator loss	3.4 dB
Sub-band bandwidth, Δf	1 GHz	Photodiode load resistance	10 kΩ
Total relative jitter, σ_j	9.47 fs	Laser linewidth	5 kHz
Comb insertion loss	7.4 dB	V_π	4 V
Photodiode responsivity	1.0 A/W	Temperature	300 K
ADC clock jitter	100 fs	ADC resolution	14 bits

Table 3.1: Simulation parameters used for results presented in Fig. 3.6 and Fig. 3.7.

the laser phase noise is modelled as a Wiener process of linewidth 5 kHz. The comb driving sinusoids are generated with white phase noise across the uncorrelated jitter bandwidth (i.e. up to ± 500 MHz offset from carrier) using different seeds to a normally distributed Mersenne twister pseudorandom number generator. This bandlimited white phase noise represents the relative jitter after correlation and filtering effects are considered, as well as any decorrelation effects caused by path length mismatch. For reference, the optical power of each comb line is plotted in Fig. B.1 in the Appendix.

The signal comb is modulated with the input RF signal, followed by demultiplex filtering and coherent detection of each modulated tone (sub-channel) as shown in Fig. 3.3. Blackman windowing functions are applied to the input test wave and each detected sub-channel in order to prevent spectral leakage. Photodiode thermal and shot noise are added at each sub-channel. Each detected sub-channel is then summed after being frequency shifted to its correct frequency band to reconstruct the complete input signal. Single tone SINAD and SFDR measurements are obtained by using a modified periodogram to estimate the power spectral density of the output signal, and comparing the relative power of the signal frequency bin to all others. For two tone testing, SINAD and IMD3 values are obtained by comparing the normalised output to the noiseless input signal. A complete list of simulation parameters can be found in Table 3.1.

3.4 Simulation and calculation results

Figure 3.6 shows the SINAD (Fig 3.6(a)) and the SFDR/IMD3 (Fig 3.6(b)) vs input frequency for an example 12-channel 12.5 GHz bandwidth channelizer, with 9.47 fs relative jitter. This jitter value is calculated from a line segment estimate to a commercially available oven controlled oscillator (OCXO) referenced microwave synthesizer, details of which are given in the Appendix. Plotted are SINAD, single

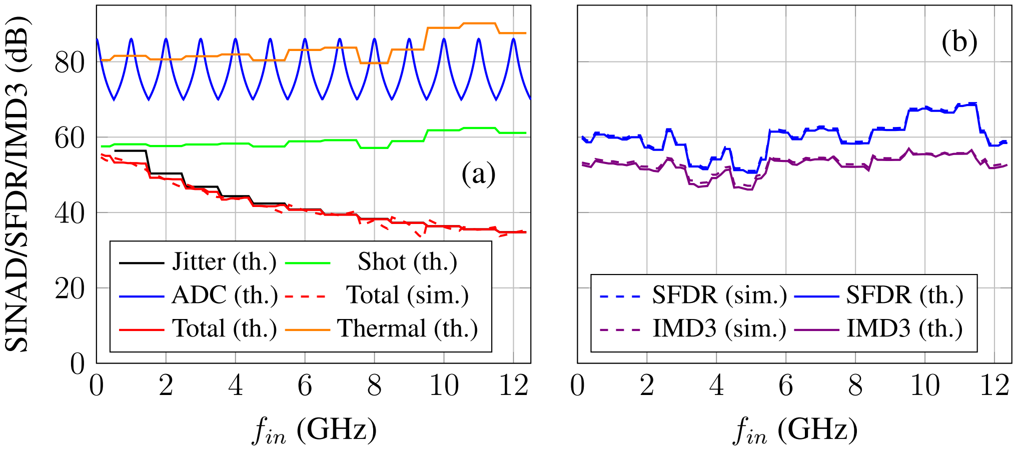

Fig. 3.6: Input test signal frequency f_{in} vs (a) SINAD and (b) SFDR/IMD3 for a 12 channel 12.5 GHz bandwidth jitter limited channelizer based on dual combs generated by cascaded intensity and phase modulator, with 9.47 fs relative jitter. IMD3 measurements (b) are obtained from the equivalent power two tone input signal, where the second tone is $+100$ MHz from f_{in}.The shot noise, jitter limited and ADC limited SINAD are also shown. Sim., numerical simulation results; th., theoretical calculation from our models.

tone SFDR, and two tone IMD3 estimates from the simulation described in the previous section and theoretical estimates derived by summing the derived expressions for photodiode noise, ADC noise, modulator nonlinearity and phase noise. The two tone IMD3 estimate is determined by an input signal equal in power to the single tone case with input frequencies f_{in}, $f_{in} + 100$ MHz. Also plotted are the photodiode shot noise (green solid line), photodiode thermal noise (orange solid line) phase noise limited SINAD (black solid line) to illustrate the limits imposed by the main stochastic noise processes, along with the sub-band ADC SINAD limit (solid blue line) which has negligible impact on the overall SINAD even at a modest ADC clock jitter (100 fs).

As shown in Fig 3.6(a), the SINAD of the channelizer is limited by the relative jitter, and essentially follows the jitter limit except for low frequencies, where shot noise and nonlinearity become prominent. The SINAD/SFDR/IMD3 plots show broad agreement between the simulation (dashed lines) and theoretical (solid lines) estimates. The shot noise limit follows the power variation between the comb lines (see Fig. B.1 in the Appendix), showing the ‘bat ears’ shape that is characteristic of the cascaded phase and intensity modulator comb generating method [103]. Both SFDR and IMD3 are more strongly affected by this variation in comb line power and see strong fluctuations (up to 20 dB) across the input bandwidth. This is because the SFDR/IMD3 for a given input frequency is dependent on the relative strength of the fundamental and generated harmonics, so will increase dramatically if the harmonics fall into a low power channel and the fundamental into a high power channel, and drop dramatically if the reverse is true. We can see from Fig. 3.6(b) therefore even the small variations in frequency comb power in this case (see Fig. B.1) can lead to strong variations in SFDR/IMD3, which highlights the importance of generating a flat frequency comb if minimizing these fluctuations is important for the application.

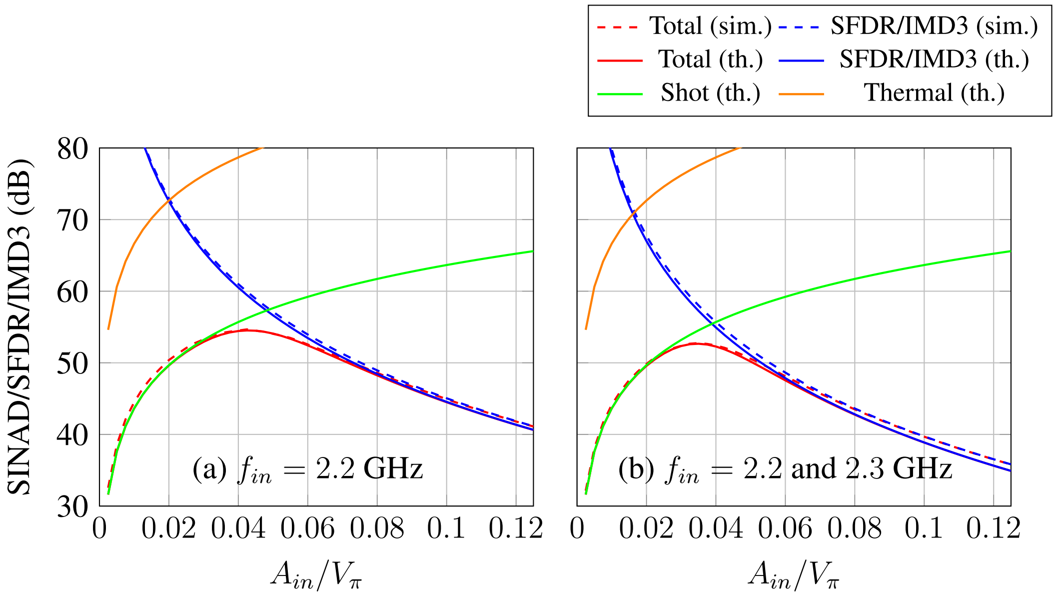

Fig. 3.7: A_{in}/V_π v SINAD for shot noise/harmonic distortion limited 12 channel 12.5 GHz channelizer. (a) shows single tone SINAD/SFDR at 2.2 GHz, (b) shows two tone SINAD/IMD3 with 2.2 and 2.3 GHz inputs. Sim., numerical simulation results; th., theoretical calculation from our models.

Figure 3.7 shows SINAD and harmonic distortion for a low relative jitter (≈ 1 fs) scenario as a function of the A_{in}/V_π, with Fig. 3.7(a) showing a single tone input of 2.2 GHz and with Fig. 3.7(b) showing the equivalent power two tone case at 2.2 GHz and 2.3 GHz. When the relative jitter is sufficiently low, the limiting factors for SINAD become SFDR/IMD3 and shot noise. This is typical of any analog optical link: driving the modulator with a low A_{in} gives a low harmonic distortion but results in a high level of shot noise, and vice versa. Thus there exists some peak value of SINAD where the penalties from nonlinearity and shot noise are balanced, as seen at around $A_{in}/V_\pi = 0.045$ in Fig. 3.7(a) and $A_{in}/V_\pi = 0.035$ in Fig. 3.7(b).

Since the modulation transfer function is known, analog or digital compensation functions can be applied that attempt to reverse the distortion introduced by the modulator and effectively shift the peak SINAD value to higher A_{in}/V_π values in Fig. 3.7. Digital techniques operating at gigasample rates have been demonstrated that achieved up to 30 dB suppression of the third order harmonic [143, 144], and analog techniques achieving as much as 45 dB suppression [145]. Clearly, the increased level of harmonic distortion in Fig. 3.7(b) due to the presence of additional inter-modulation distortion products shows that this linearization is increasingly important for more complex input signals.

The simulation (dashed lines) and theoretical estimates (solid lines) for SINAD and SFDR are in close agreement. Note that the thermal noise limit is well above the shot noise floor in this case due to the high photodiode load (10k Ω), but thermal noise will begin to contribute if the photodiode load is low or the optical power is low. If thermal noise does become a factor, it exhibits a tradeoff with harmonic distortion in the same way as shot noise.

3.5 Discussion and performance limits

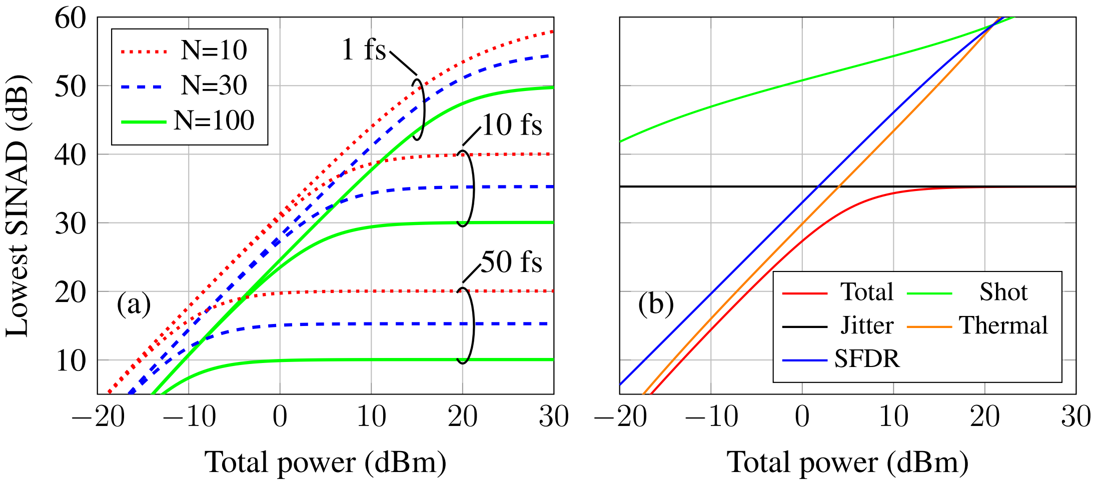

Fig. 3.8: Lowest SINAD (i.e. the N-th channel) as a function of total comb power (for both combs) for a 25 GHz channelizer, with A_{in} optimised to minimise the total noise contribution from shot noise, thermal noise and SFDR. (a) shows a variety of channel numbers, N, and relative jitters, while (b) shows the constituent noise contributions for the $N = 30$, jitter = 10 fs case. The photodiode load is assumed to be 50 Ω, demultiplex loss is 3 dB and modulator insertion loss is 3.4 dB.

After confirming the theoretical modelling with numerical simulation, we expand our discussion to general dual comb systems which may use different comb techniques or target a different bandwidth, and therefore have different number of channels and optical power. Fig. 3.8(a) shows how the worst case SINAD (i.e. for the N-th, or highest, channel) changes with total comb power (assuming the same power for each tone) for a variety of channelizer configurations at 25 GHz bandwidth and is illustrative of the general performance trends for dual frequency comb channelizers. The jitter values are full bandwidth jitter values that assume that the uncorrelated jitter has a white spectrum, and therefore scales with $1/\sqrt{N}$. A relative jitter of 50 fs represents that achievable between two electro-optic frequency combs referenced to a typical high quality commercial oscillator. On the other hand, 1 fs represents jitter levels for state of the art photonic approaches, where the frequency comb is referenced to a high quality optical reference cavity [157, 158, 159].

Generally, increasing the total comb power will increase SINAD until it saturates at a certain level due to the phase noise contribution, which is independent of power. This is seen more clearly in Fig. 3.8(b) which separates out the constituent noise components for the $N = 30$, jitter = 10 fs case. At low powers, thermal noise and SFDR is the dominant noise contribution until the relative jitter caps the SINAD at approximately 35 dB. The effect of changing the number of channels is seen in Fig. 3.8(a): more channels leads to lower total SINAD in all cases, since it increases shot and thermal noise due to less power per comb line and phase noise due to the highest channel being detected further from the frequency comb centre. This penalty may be outweighed however by the advantages of lower bandwidth analog and digital signal processing in the narrower channels.

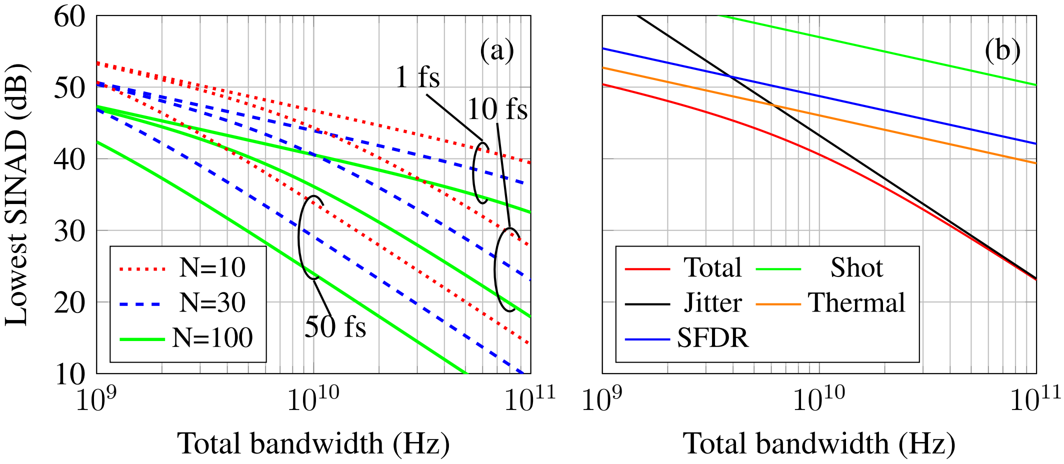

Fig. 3.9: Lowest SINAD (i.e. the N-th channel) as a function of total channelizer bandwidth for a total comb power of 10 dBm, with A_{in} optimised to minimise the total noise contribution from shot noise, thermal noise and SFDR. (a) shows a variety of channel numbers, N, and relative jitters, while (b) shows the constituent noise contributions for the $N = 30$, jitter = 10 fs case. The photodiode load is assumed to be 50 Ω, demultiplex loss is 3 dB and modulator insertion loss is 3.4 dB.

This is further seen in Fig. 3.9, which shows the worst case SINAD as a function of total channelizer bandwidth, assuming a fixed total comb power of 10 dBm. Here there is also a consistent penalty with increasing N across all scenarios in Fig. 3.9(a), and the different relative jitters converge at low bandwidths where the thermal/shot noise and SFDR become the limiting noise factors. At high bandwidths phase noise limits the achievable SINAD as is clearly seen in Fig. 3.9(b), which plots the separate noise components for the $N = 30$, jitter = 10 fs case. Note that achieving these theoretical limits in a low bandwidth (<10 GHz) channelizer may be challenging due to the narrow optical filtering required, which although achievable for example via optical injection locking [160, 161], can introduce additional absolute phase noise or decorrelation.

Both graphs highlight the dual comb channelizer's extreme sensitivity to relative phase noise when trying to achieve high accuracy and bandwidth. Indeed, Fig. 3.8(a) and Fig. 3.9(a) display how a relative jitter of only 50 fs will result in a phase noise limited channelizer in most cases. This may not be a problem in high noise and spread spectrum applications such as [129, 131, 130], but emphasises the importance of broadband phase noise correlation between the comb sources or low absolute jitter if high SINAD is required. Furthermore, the phase noise correlation between comb lines [162] may allow for novel digital signal processing schemes that can efficiently compensate the phase noise discussed here to some degree [163, 164, 165].

Finally, it is important to emphasize that the fundamental performance parameters discussed in this Chapter are not the only factors that will determine the extent to which dual frequency combs can be used as channelizers. The practical implementation of the dual-comb channelizer would benefit from the rapid development of photonic integrated circuits, which allow for high performance frequency comb sources, minimized channel mismatch and high density coherent receiver arrays that drives down the cost and power consumption. Heterogeneous integration that harnesses the benefit of different integration platforms, including silicon nitride [99, 135, 166] and thin lithium niobate [167, 168, 169, 170] and high performance III-V/Si/Si_3N_4 on silicon light sources [171, 172], could lead to a promising integrated solution for the dual-comb channelizer.

3.6 Summary

This Chapter has introduced the concept of dual frequency comb based analog to digital conversion and detailed a theoretical analysis to assess which factors limit the achievable signal to noise and distortion ratio. Our theoretical estimates were tested against a simulation model in an example performance analysis, which demonstrated how the noise contributions varied across the channelizer bandwidth and how the signal driving power affects the observed SINAD. In a broader discussion of dual comb channelizers, we showed that while sufficient comb power is important for overcoming thermal and shot noise limits, the dual comb channelizer is ultimately sensitive to the relative phase noise between the two frequency combs in high bandwidth scenarios.

Chapter 4

Experimental characterisation

In this Chapter, we investigate the performance of the dual frequency comb channelizer experimentally. Firstly, we measure the phase noise of an electro-optic dual comb system sharing a common reference to test our phase noise predictions from Chapter 3. These phase noise measurements are conducted using a single commercial phase-locked loop (PLL) based synthesizer chip which although has worse performance than the synthesizer used in the latter part of this thesis, has significantly more published details about the PLL design and allows for easier interpretation of the phase noise results. Then we construct a low phase noise dual frequency comb analog to digital converter prototype and test its performance in sub-sampling mode using the IEEE ADC testing standard [173] for comparison against the ADCs in the literature discussed in Chapter 2.

4.1 Phase noise characterisation

4.1.1 Experimental setup

To measure the phase noise of an electo-optic dual comb system, we devised the experimental setup shown in Fig. 4.1. A low linewidth (2.3 kHz) fiber laser at 1555.747 nm followed by a booster EDFA is used to seed two electro-optic frequency comb generators based on cascaded intensity and phase modulators [103]. The comb driving signals were generated from a 100 MHz crystal oscillator reference by two fractional-N PLL based synthesizers (Texas Instruments LMX2595) with an approximate loop bandwidth of 285 kHz and doubled to create two driving signals of frequency 25 GHz and 26 GHz for the signal and LO comb respectively. These driving signals are amplified such that each comb generates approximately 25 comb lines each within 3 dB power variation.

The comb outputs are then mixed in a 50/50 coupler with the coupler outputs being used as the inputs to a 50 Ω loaded 42 GHz optical balanced detector. Before being fed to the balanced detector, each branch is filtered by an optical bandpass filter in order to select the n-th comb line, such that a $n\Delta f$ beating signal is observed at the balanced detector output. The phase noise of this beating signal can then be measured

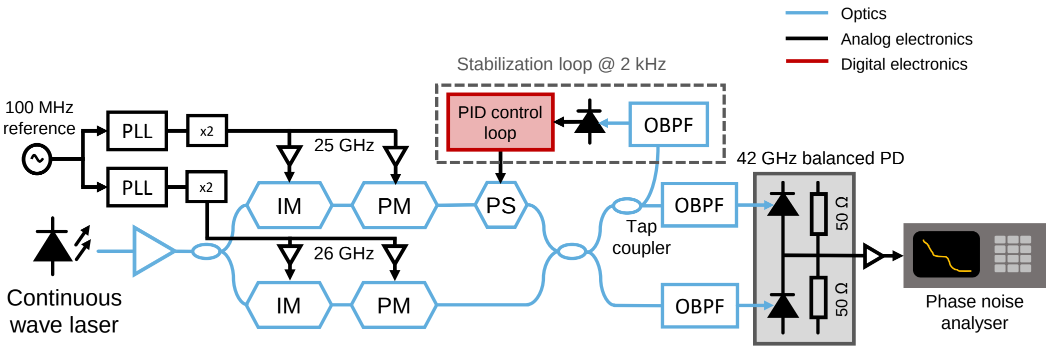

Fig. 4.1: Experimental setup. The PLL is a Texas Instruments LMX2595, details of which are described in Appendix B.3. IM, intensity modulator; PM, phase modulator; OBPF, optical bandpass filter; PD, photodiode; PS, phase shifter; PID, proportional integral derivative.

by a phase noise analyser, with the phase noise averaged over multiple measurements. All optical devices are fiber coupled to polarization maintaining fiber and the power into the photodiode remains constant between measurements. For comparison, we also measured the phase noise of each PLL, $|\phi_{LO}|^2$ and $|\phi_{sig}|^2$, and estimated the expected phase noise resulting from a coherent ($n^2|\phi_{LO} - \phi_{sig}|^2$) and incoherent ($n^2|\phi_{LO}|^2 + n^2|\phi_{sig}|^2$) sum of their phase noise.

One practical issue with the experimental setup is that the configuration of the two frequency combs essentially acts as a fiber Mach-Zehnder interferometer. Thus, any time dependent vibration and temperature induced phase fluctuations between the two branches will induce slow phase drift that increases the low frequency phase noise measured at the balanced receiver. To mitigate this, we use a slow feedback control loop to compensate for the vibration and thermal induced phase variations. As shown in Fig. 4.1, a tap coupler is used to tap off 1% of the light in one of the branches after the 50/50 coupler and filtered using an optical bandpass filter such that only the central comb lines are incident on a photodiode. This beating signal between the center tones of the two combs is used as the error signal for a digital proportional integral derivative (PID) controller that is used to stabilize the optical path length variation between the two combs by driving a piezo electric fiber phase shifter.

The PID feedback loop operates at 2 kHz bandwidth and so is able to effectively suppress any sub-kHz temperature and vibration induced optical path length fluctuations between the two branches. It is important to note that this feedback loop is unable to correct for any relative phase noise induced by the frequency combs themselves, since the central tone of the combs does not carry any phase noise from the driving signals (i.e. $n = 0$ in (3.21)). The feedback loop therefore only corrects for phase noise induced by the optical path length variation, and allows for accurate measurement of the relative phase noise between the two combs without artificially suppressing the phase noise in the sub-kHz offset frequency region.

4.1.2 Results

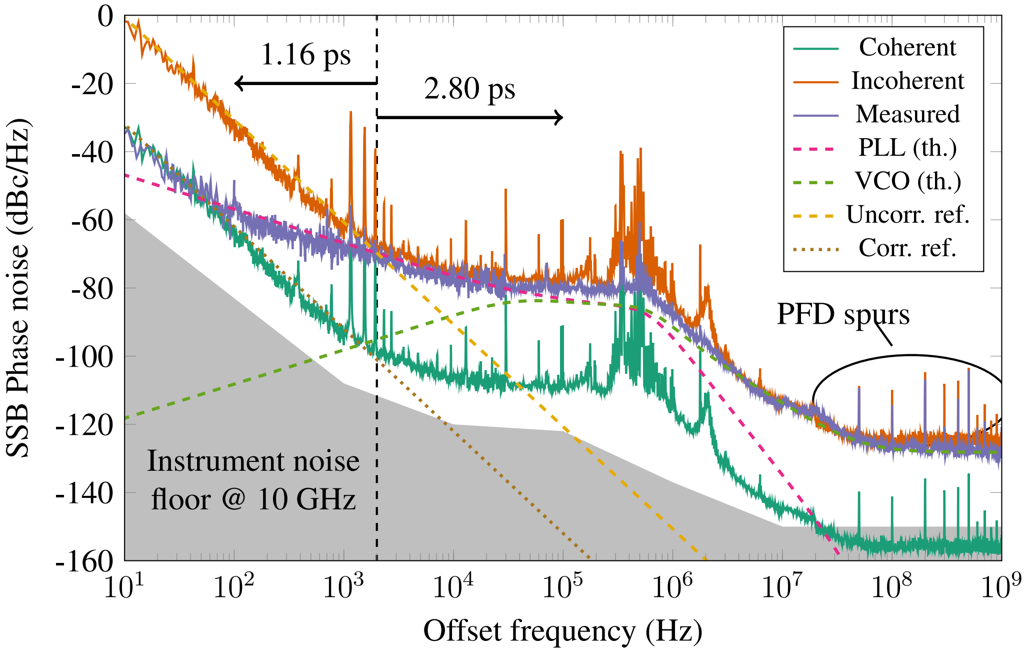

Fig. 4.2: Measured single side band phase noise of the 10 GHz beat note, whose total integrated jitter is 3.03 ps. Plotted for comparison are the coherent ($n^2|\phi_{LO} - \phi_{sig}|^2$) and incoherent ($n^2|\phi_{LO}|^2 + n^2|\phi_{sig}|^2$) summations of the PLL synthesisers phase noise, along with the integrated jitter below (1.16 ps) and above (2.80 ps) 2 kHz offset. The grey shaded region indicates the phase noise analyser phase noise at 10 GHz. PFD, phase frequency detector.

In Fig. 4.2, we use the phase noise measurement of the 10 GHz beat note ($n = 10$ channel) as an example to explain the composition of phase noise of the dual comb system. The measured single side band phase noise is shown as the purple curve, along with the estimated coherent ($n^2|\phi_{LO} - \phi_{sig}|^2$, green curve) and incoherent ($n^2|\phi_{LO}|^2 + n^2|\phi_{sig}|^2$, orange curve) sum of the two driving signals' phase noise. In addition, the $1/f^3$ estimate for the reference phase noise contribution is plotted twice: based on whether the reference phase noise is correlated (brown dotted line) or uncorrelated (yellow dashed line) between the two comb driving signals. This estimate is derived from a direct measurement of the reference oscillator phase noise.

For frequencies >2 kHz, the phase noise closely follows the incoherent sum of the driving signals phase noise, with the observed phase noise being a result of the incoherent summation of the PLL (pink dashed line) and voltage controlled oscillator (VCO) (green dashed line) phase noise ($n^2|\phi_{LO}|^2 + n^2|\phi_{sig}|^2$). The 'PLL' phase noise in this case contains contributions from the charge pump, phase detector and loop filter, details of which are provided in Appendix B.3. The integrated jitter in this

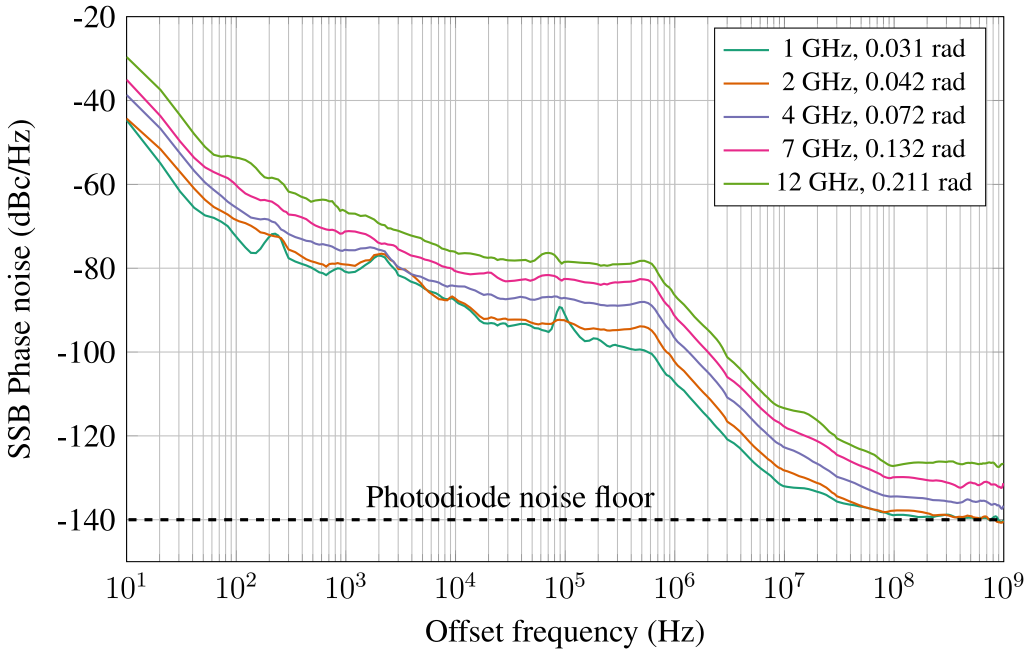

Fig. 4.3: Measured single side band phase noise of for various comb line numbers, with integrated phase noise from 10 Hz to 1 GHz shown in the legend. The measured phase noise has been smoothed with spurs removed for clarity.

section is 2.80 ps. In the low frequency region <2 kHz, however, the main phase noise contribution on each comb is the reference oscillator, which is correlated between the two combs. The phase noise power therefore drops below that predicted by an incoherent summation of the two synthesizers' phase noise, and begins to track the coherent summation of reference phase noise ($n^2|\phi_{LO} - \phi_{sig}|^2$) at approximately $<$100 Hz. In this section the integrated jitter is 1.16 ps, leading to an overall integrated jitter of 3.03 ps from 10 Hz to 1 GHz, or 0.19 rad at 10 GHz. The exact frequencies of these crossover points will be dependent on the specific reference oscillator used and PLL configuration. Note that the spurs plotted are specific to this system due to the cross talk on the printed circuit board of the PLL synthesizer, and can be eliminated through more careful design of the synthesizer. We suspect that some of these spurs are amplitude noise spurs (e.g. spurs at ≈ 400 kHz) that are suppressed during the nonlinear comb generation process, evidenced by the fact that they do not appear in the measured comb phase noise. However, they appear in the coherent/incoherent estimates due to the limitations of our phase noise analyzer in suppressing amplitude noise during direct measurement of the synthesizers' phase noise.

To show the scaling of phase noise with regard to the beat frequencies, we plot the phase noise for various channel numbers in Fig. 4.3, i.e. the beating between the n-th comb line of each comb, generating a tone of frequency $n\Delta f$. This shows that the relationship shown in Fig. 4.2 holds for any channel number. As expected, the total phase noise power increases as n^2. At low channel numbers (specifically $n = 1, 2$ in

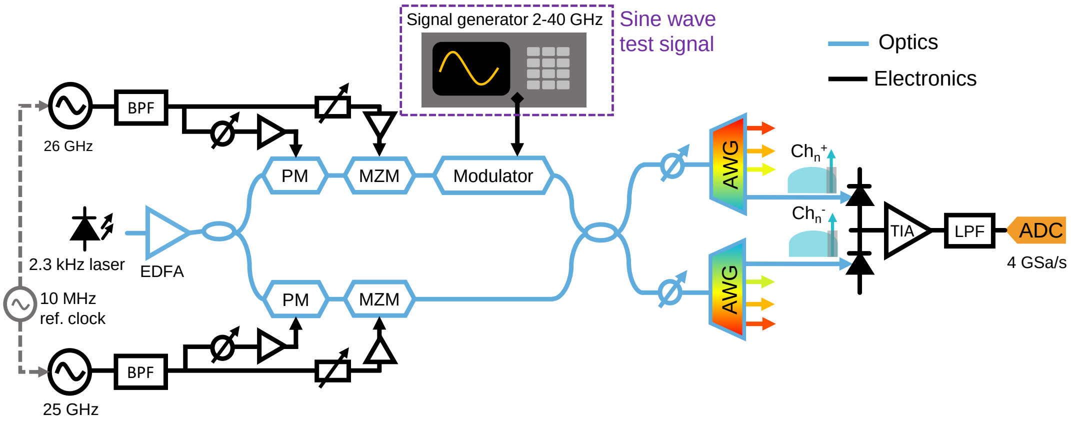

Fig. 4.4: Experimental setup. MZM, Mach-Zehnder modulator; PM, phase modulator; BPF, band-pass filter; EDFA, erbium-doped fiber amplifier; arrayed waveguide grating (AWG), arrayed waveguide grating; Ch, channel; TIA, transimpedance amplifier; ADC, analog to digital converter; LPF, low pass filter.

Fig. 4.3), we observed some increase in phase noise in the 2 kHz to 10 kHz region. This is likely the aforementioned vibrations picked up by the experimental setup that were unable to be compensated by the 2-kHz feedback loop, since it does not scale with channel number. This could be reduced by employing a faster feedback loop or photonic integration of the dual comb system. Furthermore, the $n = 1, 2$ channels also reach the photodiode thermal noise floor of our setup at frequencies > 10 MHz.

The results in Fig. 4.2 and Fig. 4.3 confirm the description in (3.21). Furthermore, since in this case the reference noise contribution is negligible above approximately 2 kHz we can write

$$|k_{LO}(\omega) - k_{sig}(\omega)|^2 |\phi_c(\omega)|^2 \approx \left(\frac{\Delta f}{f_{ref}}\right)^2 |\phi_{ref}(\omega)|^2 \tag{4.1}$$

where $|\phi_{ref}(\omega)|^2$ is the phase noise power of the reference at frequency f_{ref}. This approximation holds for electro-optic dual combs synthesized from a common reference, but may not hold if the reference contributes substantial phase noise at higher offset frequencies, or is not coherent between the two combs.

4.2 Dual comb sine wave testing

4.2.1 Dual comb ADC design and experimental setup

To evaluate the performance of the dual comb scheme, a dual frequency comb ADC prototype was built as shown in Fig. 4.4. In contrast to the dual comb system used for the previous section, this prototype was engineered to ensure minimal phase noise on the both the LO and signal comb. Two electro-optic frequency combs were generated from a common seed laser whose linewidth was measured to be 2.3 kHz, as shown in

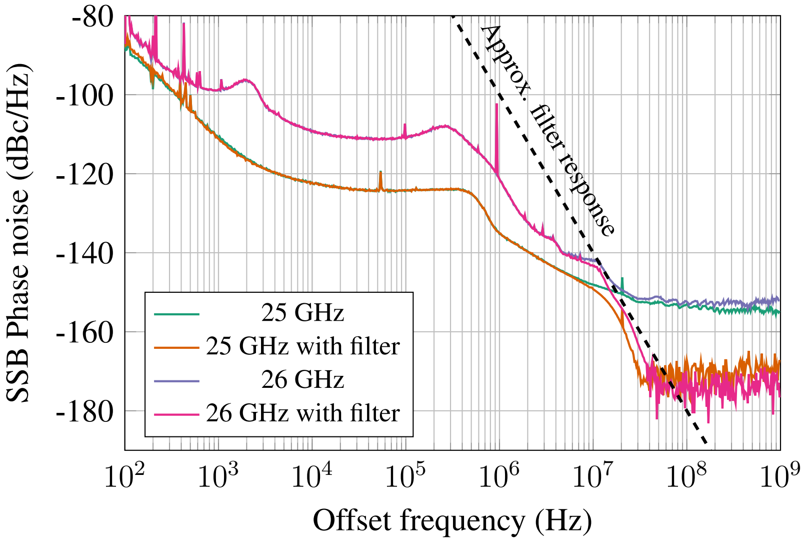

Fig. 4.5: Single side band phase noise of the signal (26 GHz) and LO (25 GHz) comb driving signals, with and without the cavity bandpass filters designed to reduce the wideband phase noise. The approximate filter response is illustrated by the dashed line, measured filter responses are given in Appendix B.4.

Appendix B.6. This laser, centred at 1555.949 nm., had an output power of 18.8 dBm that was subsequently boosted by an EDFA to up to 38 dBm. The driving signals for the electo-optic combs were generated from two Rohde and Schwarz low phase noise synthesizers, with the signal comb spacing set to 26 GHz and the LO comb spacing set to 25 GHz. Furthermore, the RF driving signal for each comb was filtered by two 25 MHz bandwidth bandpass filters centred at the driving frequency of each comb. The purpose of these filters was to suppress high frequency phase noise of the comb driving signals that would be transferred to the received signal and subsequently degrade the overall SINAD, as explained in Chapter 3.

The effect of these filters on the comb phase noise is shown in Fig. 4.5. Without the filters, both synthesizers exhibit an approximately -150 dBc/Hz white phase noise floor at frequencies of 10 MHz and higher. This is well above the thermal noise limited phase noise floor: given that the power of each RF signal is 10 dBm the thermal noise floor would be expected at -184 dBc/Hz given the thermal noise power spectral density of -174 dBm/Hz. Therefore, filtering should significantly improve the wideband phase noise of the comb driving signals. This can clearly been seen in the filtered phase noise spectra shown in Fig. 4.5: the filtering effect begins to suppress the phase noise at offset frequencies above 10 MHz, with the white phase noise floor being reduced by approximately 20 dB to around -170 dBc/Hz.

Note that this is actually the white phase noise floor of the phase noise analyser itself and so it is likely that the actual white phase noise floor of the comb driving signals is lower. Given the bandpass filter responses, shown in Appendix B.4, it can reasonably

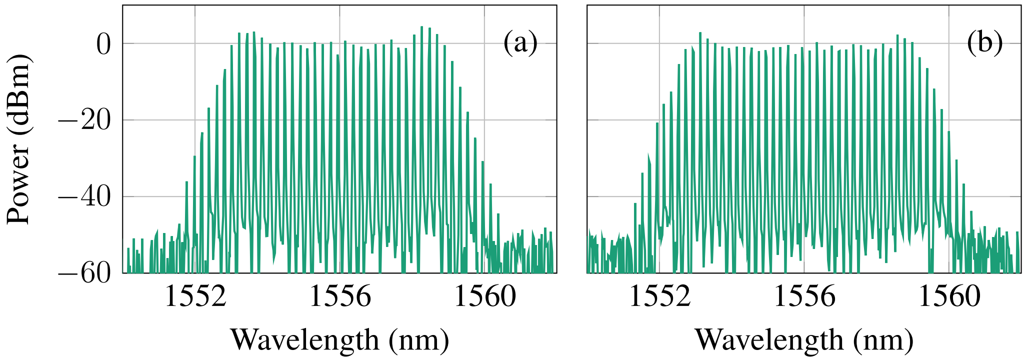

Fig. 4.6: Optical spectra of (a) signal comb with 26 GHz spacing and (b) LO comb with 25 GHz spacing. Both combs are centred at 1555.747 nm. Resolution is 0.01nm.

be assumed that for offset frequencies above 50 MHz, the broadband phase noise is suppressed to the the thermal noise limit of -184 dBc/Hz. Suppressing this wideband phase noise is particularly important given that any phase noise compensation schemes will be mostly effective at compensating low offset frequency phase noise (i.e. slow fluctuations). In schemes with large channel bandwidth, i.e. high Δf, reducing the wideband phase noise is even more important since this will form a larger proportion of the contributed jitter.

The RF driving signals are used to create two frequency combs via cascaded phase and intensity modulators as in [103]. The insertion loss of the phase and intensity modulators is 3.3 dB and 3.7 dB respectively, leading a total power of around 23 dBm for both frequency combs. The input signal of interest is in this case a sine wave that is modulated onto the signal comb via a Mach-Zehnder modulator biased at the null. The modulated signal comb and LO comb are combined in a 50/50 coupler, the outputs of which separated into the desired channels by two 25 GHz spaced AWGs. Note that all fibre up to and including the 50/50 coupler is polarisation maintaining fiber of the PANDA type, while fibre after the coupler is standard single mode fiber so that the two comb branches are aligned in polarisation during recombination. The path lengths between the signal and LO combs are carefully matched to $<$ 1 cm to ensure coherent suppression of the laser phase noise, as described in Section 3.2.2. Similar path length matching is ensured for fibre between the upper and lower branch AWGs.

For the sine wave testing in this Chapter, we perform sequential detection of each sub-band as shown in Fig. 4.4. The receiver consists of a balanced detector transimpedance amplifier (TIA) circuit with a bandwidth of 1.6 GHz. The detected electrical signal is filtered by a 650 MHz bandwidth low pass LC filter (Mini-Circuits VLFX-650+) and finally digitised by a 4 GSa/s, 12 bit analog to digital converter (Analog Devices AD9209). The ADC has a SINAD of approximately 57 dB (9.2 bits ENOB) for a -1 dBFS input when integrating across the entire ADC bandwidth and requires approximately 6 dBm RF power to hit its full scale input, once accounting for

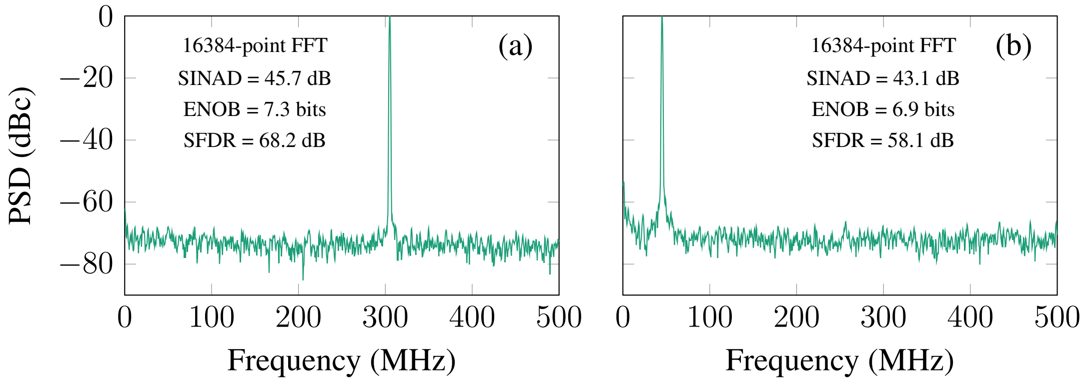

Fig. 4.7: Example captured spectra at (a) 2.305 GHz (2nd channel) and (b) 19.955 GHz (8th channel). The displayed spectra are an average of 4 16384-point FFTs.

the balun and matching network at the ADC input. The analog electrical front end circuit diagram is shown in Appendix B.5 .

The digital signal processing employed in this Chapter is relatively simple since the purpose is only to detect sine waves to estimate the system SNR, SINAD and SFDR as per the IEEE standard. For each sequentially detected channel, a 500 MHz low pass brick wall filter is applied to the detected signal and any DC offset is eliminated. In this case, the detected bandwidth of each channel is only 500 MHz since full coherent detection of each channel is not performed. Only balanced detection of each sub-channel is realised and therefore the system is unable to distinguish between signals in the upper and lower sidebands of each sub-band, for example the frequencies 1.8 GHz and 2.2 GHz in the 2nd channel. To detect arbitrary signals in each sub-band and therefore reconstruct an arbitrary signal across the entire system bandwidth, coherent detection of each sub-band is required which is demonstrated in Chapter 5. However, simple balanced detection of the channel is sufficient to perform the sine wave testing in this Chapter.

After digital filtering, the SFDR, SNR and SINAD of the detected signal can be estimated from the power spectral density of the detected signal, examples of which are shown in Fig. 4.7. A Kaiser window with $\beta = 38$ is applied to reduce spectral leakage caused by discontinuities due to finite capture length of the digital signal. In Fig. 4.7(a), a 2.305 GHz signal detected in the 2nd channel is shown. As expected, the effect of the dual comb system is to downconvert the 2.305 GHz signal by 2 GHz to the observed intra-channel frequency of 305 MHz seen in Fig. 4.7(a). As another example, Fig. 4.7(b) shows a 19.955 GHz signal appearing as a 45 MHz signal in the 8th channel. This second case shows the ability of the dual comb ADC to detect signals above its Nyquist bandwidth of 13 GHz, which is set by the 26 GHz spacing of the signal comb. The 19.955 GHz signal is in the 2nd Nyquist zone and has been aliased back into the 8th channel of the receiver. Both examples show relatively white noise floor, the origin of which will be explored later in this section. A slight rise in the noise floor can be observed at frequencies close to the carrier, which can be attributed to the close in phase noise of the frequency comb, as is plotted in Fig. 4.5. Furthermore, no spurious tones can be observed within the detected channel in both cases and the SFDR is defined by the aforementioned noise floor, indicating that the channel analog circuitry (photodiode, TIA, filter, ADC etc) provides a linear mapping from the optical to digital domain.

4.2.2 Results

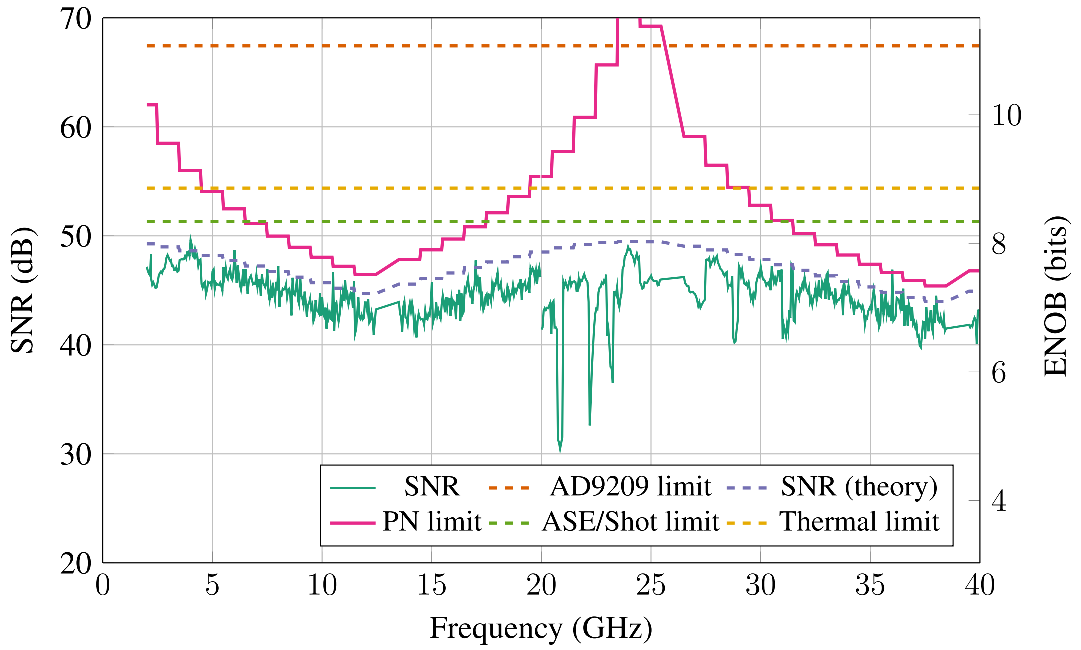

Fig. 4.8: SNR *excluding* harmonic distortions as a function of input frequency.

Firstly, the frequency of the single tone input signal was swept from 2-40 GHz while maintaining a fixed input power of 20 dBm. For frequencies below 20 GHz, the modulator is driven directly from the RF synthesiser, which is an Anritsu MG3692B. For frequencies in the range 20-40 GHz, a Marki ADA1020 frequency doubler is used to produce the desired frequency, since the synthesizer's frequency range is limited to 2-20 GHz. The SNR of the observed signal in its expected channel was calculated from an average of 4 16384-point FFTs and is plotted in Fig. 4.8 along with the corresponding ENOB. This SNR is calculated excluding harmonic distortions, which are analysed separately later in the Chapter since they are deterministic distortions: the purpose of Fig. 4.8 is to determine the fundamental performance of the dual comb ADC considering only stochastic noise as discussed in Chapter 3. Exclusion of the harmonic distortions is particularly important for frequencies above 20 GHz, since the frequency doubler has only -10 dBc suppression of the 2nd and 3rd harmonics and only -20 dBc suppression of the input signal, meaning that harmonic distortions observed in this range are not indicative of the dual comb system performance. Furthermore, since only a single channel is detected, the harmonic distortions would only be visible when the harmonics fall into the same channel as the fundamental, which only occurs for certain channels as can be calculated by (3.1).

Overall, the dual comb ADC maintains an SNR of over 40 dB across almost the entire frequency range plotted in Fig. 4.8, up to 40 GHz. At 40 GHz, the dual comb ADC achieves 44 dB SNR, equivalent to 7.0 bits ENOB. This result is equivalent to a timing jitter of 25 fs: i.e. an ADC with 25 fs jitter as its only source of noise would be able to detect the signal with the same fidelity. This outperforms all electronic ADC results and is equivalent to the best reported results of time interleaving photonic ADCs (see Fig. 2.11), with the potential for further improvements due to the relaxed jitter requirements of the frequency interleaving design as described in Chapter 2.

Drops in SINAD seen around 20 GHz are due to the limited common mode rejection ratio (CMRR) of the balanced photodiode (approximately 30 dB) causing signal-signal beat interference (SSBI) between modulated harmonics and the fundamental. For example, at 20.755 GHz, the fundamental and the unsuppressed harmonic (31.1325 GHz, third harmonic from the doubler input frequency) are approximately equidistant from the signal comb beat frequency 26 GHz and so have a signal-signal beat frequency $< \Delta f$ when incident on the photodiode. This causes additional frequency components to be observed if the CMRR of the photodiode is not sufficiently high, a problem which is especially acute when detecting broadband signals, as discussed in Chapter 5.

The overall variation in SNR is primarily caused by phase noise, as can be seen by the phase noise SNR limit plotted in Fig. 4.8. This phase noise limit is calculated from the measured phase noise of the comb synthesizers plotted in Fig. 4.5 according to the phase noise properties of the dual comb system derived in Chapter 3. When the signal is detected in the low channels (e.g. < 5GHz, and around 26 GHz) the SNR approaches 50 dB and is primarily limited by ASE/shot noise.

Notably, for the dual comb system the limit imposed by phase noise is, unlike other time interleaving designs, not strictly related to the detected frequency. As Fig. 4.5 demonstrates, the SNR can actually increase with an increase in the detected frequency when the signal is in the higher Nyquist zones. As was described in Chapter 3 the phase noise limit is instead related to the overall detectable bandwidth, which is in turn defined by the number of comb lines and Δf between the comb lines.

The maximum detectable frequency of the dual comb system is in practice limited by analog bandwidth of the input modulator, which in this case was 40 GHz (3dB bandwidth). The efficiency of the bulk lithium niobate modulators used here are in general limited due to the large waveguide structures, requiring the electrodes to be placed far from the propagating optical mode and increasing the required driving voltage [174, 175]. However, thin film lithium niobate has led to demonstrations of low V_π modulators with high bandwidths (e.g. $V_\pi = 2.3$ V, 100 GHz [176, 177]) and bandwidths approaching terahertz frequencies [178].

The maximum detectable frequency is ultimately limited by the bandwidth of the signal comb itself, which in this case is 338 GHz. This feature of the dual comb ADC, when combined with high bandwidth input modulators may be particularly useful in future wireless and radar applications as carrier frequencies are pushed to mm-wave and beyond [179, 180, 133]. The dual comb system demonstrated here would offer flexible, high resolution detection of broadband signals centred at extremely high frequencies without the need to rapidly switch local oscillator frequencies [132, 181].

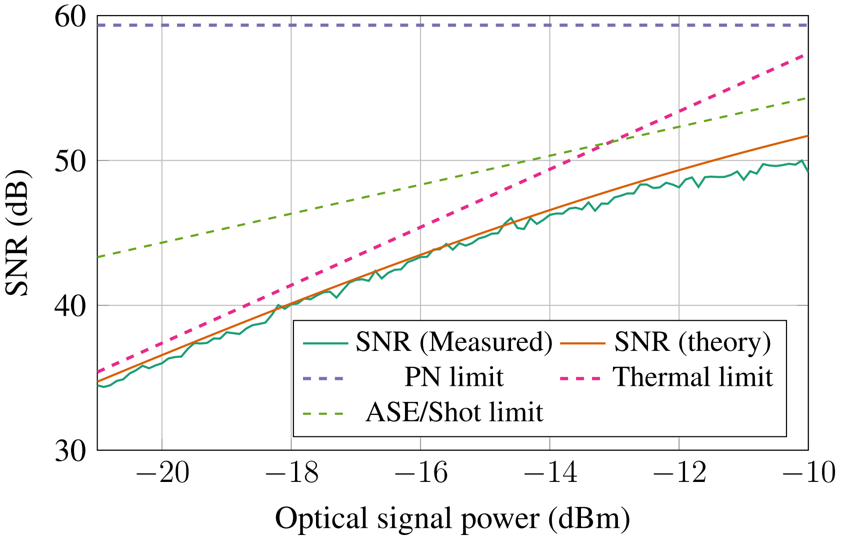

Fig. 4.9: SNR for a 2.2 GHz test signal as a function of optical signal power in the 2nd channel. SNR (th.) shows the SNR predicted by theory, dashed lines indicate limits imposed on the SNR by different noise sources. LO optical power is 10 dB higher than the signal optical power.

The optical power of the EDFA shown in Fig. 4.4 was also swept to determine the effect of total optical power on system performance. The output power of the EDFA was altered by changing the power of the pump laser diode, while keeping the input power of the seed laser fixed at 19 dBm. Fig. 4.9 plots the SNR calculated from an average of 4 16384-point FFTs as a function of the optical signal power measured in the 2nd channel (i.e. at the output of the respective AWG channel), for an input frequency of 2.2 GHz. The input signal RF power is fixed at 25 dBm. Due to the modulation and insertion loss of the modulator, the LO optical power per channel is 10 dB higher than the signal power shown in the axis of Fig. 4.9.

At low signal powers, the overall noise is dominated by thermal noise at the photodiode. This means that increasing the overall optical power by 1 dB will lead to a 2 dB increase in SNR since the photodiode is a square law detector. As the signal power exceeds approximately -13 dBm, ASE and shot noise becomes the main limiting factor. The ASE originates from the EDFA, which has a noise figure of 6 dB, but will be attenuated towards the optical shot noise floor as the signal and LO combs propagate through the dual comb system. The higher power of the LO comb ensures that it is the main contributor of ASE and shot noise. Since the 2.2 GHz signal is detected in the 2nd channel, the effect of phase noise as shown in Fig. 4.9 is negligible and is only plotted for reference as it does not depend on optical power.

Performance in the thermal noise limited region could be improved significantly by careful design of a lower noise thermal transimpedence amplifier. For the dual comb prototype demonstrated in this Chapter 4, a modified commercially available balanced detector (Thorlabs PDB-480C) was used as the photodiode-TIA receiver circuit. The noise performance of this photodiode-TIA is significantly poorer than what is possible since the photodiode uses a general purpose 50-ohm matched broadband amplifier (ABA-52563) as the transimpedence element. The relatively low frequencies (<500 MHz) required for the sub-band reception should allow for loading of the photodiode at much higher impedance and subsequent improvement in the photodiode thermal noise. Elimination of the EDFA should ensure that the dual comb system is shot noise limited at high optical powers and remove the contribution of ASE, which raises the optical noise floor by the EDFA noise figure of 6 dB in this experiment. In this discrete component demonstration, the EDFA is required to overcome the insertion losses of the comb modulators, input modulators and AWGs. On an integrated platform these insertion losses will no longer exist, aside from potential coupling losses from co-integration [182], which should remove the requirement for amplification of the seed laser. Combined with improvement of the photodiode-TIA thermal noise, good performance of the dual comb system should be possible with significantly lower optical powers than demonstrated here.

Finally, the effect of input RF signal power on harmonic distortions and therefore overall SINAD was investigated. As derived in Chapter 3, the main source of distortion will be third order harmonic distortions introduced by the nonlinearity of the Mach-Zehnder modulator. To measure this, the dual comb ADC was driven with a 2.2 GHz input sine wave whose power was varied from -10 to 25 dBm. In this experiment, the 2nd and 7th channels were detected simultaneously so that the fundamental 2.2 GHz and 6.6 GHz 3rd order harmonic respectively could be observed in parallel. Both channels were detected by synchronous ADCs with identical balanced receivers, and careful path length matching was implemented between the two channels, along with digital delay compensation. As shown in Fig 4.6, the 2nd and 7th channels are towards the centre of both combs and so have very similar powers, minimising the impact of any gain mismatch.

The captured 2nd and 7th channels were digitally up shifted to their respective

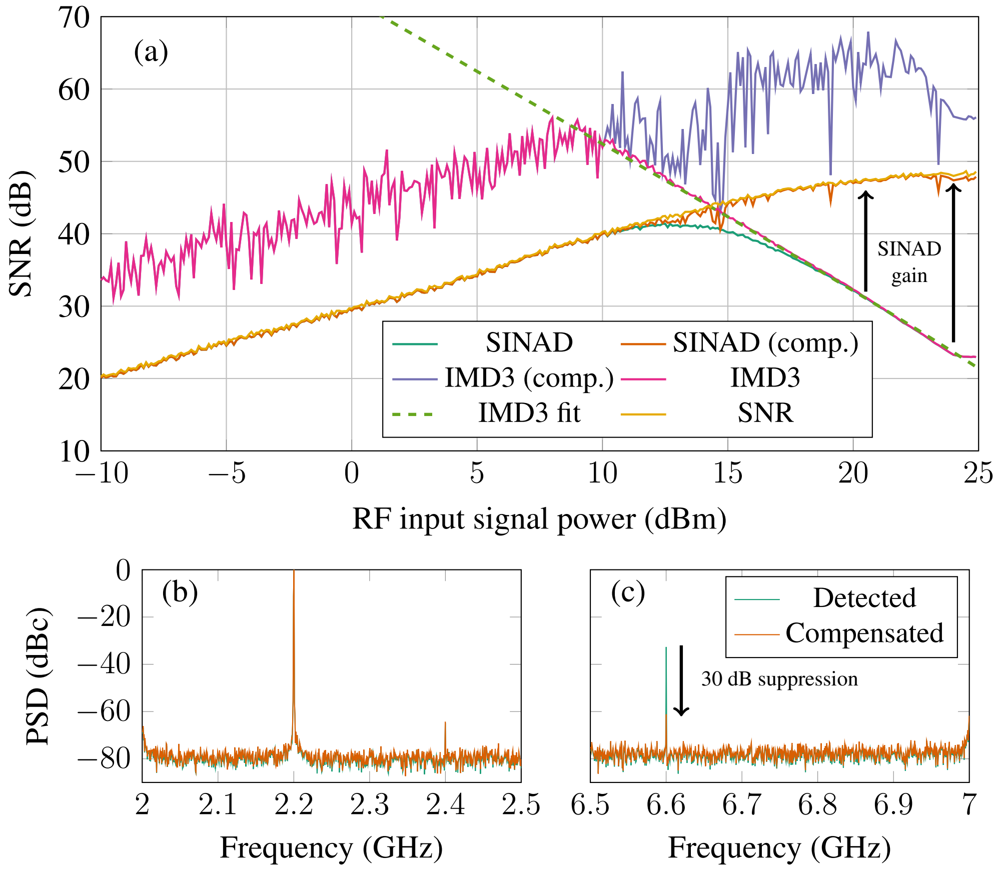

Fig. 4.10: (a) IMD3 and resultant SINAD vs input signal power, with optical signal/LO power at -10/0 dBm. Estimated Vpi is 6.2 V. Application of an arcsin function linearises the modulator transfer function and leads to SINAD gain in the region $>$ 12 dBm. (b) Detected/compensated 2.2 GHz test signal in the 2nd channel. (c) Detected/compensated 6.6 GHz third order harmonic in the 7th channel.

frequencies and the relative power of the fundamental and 3rd harmonic, known as the third order intermodulation distortion (IMD3) was calculated. Example spectra of the measured 2nd and 7th channels for an RF input power of 20 dBm are shown in Fig 4.10(b) and Fig 4.10(c) respectively in orange. In Fig 4.10(a) the IMD3 as a function of the full range of RF input powers is shown. At low RF powers, the dual comb SNR is shot noise limited and the increasing IMD3 simply tracks the white noise floor as the 3rd order distortion is below the ASE/shot noise floor. At approximately 10 dBm however, the distortion level becomes larger than the stochastic noise and the IMD3 causes a rapid decrease in the total SINAD. At 25 dBm, the overall SINAD drops to approximately 22 dB despite the SNR implying a stochastic noise floor of 48 dB (7.7 bits ENOB). This decrease in IMD3 is simply a function of (3.38), and the fit of (3.38) to the measured IMD3 is plotted in Fig 4.10(a) as the pink dashed line labelled ‘IMD3 fit’. Assuming the comb powers are equal, this trend is strictly defined by the modulator V_π which is estimated as 6.2 V from Fig 4.10(a), in line with the specification of the Mach-Zehnder modulator (MZM) used in this experiment.

Clearly, the IMD3 trend in Fig 4.10(a) exemplifies the trade-off described in Chapter 3 that it is beneficial to drive the modulator at quite high powers in order to increase the ASE/shot noise limit, yet this comes at the expense of strong harmonic distortions introduced by the sine transfer function of the MZM (see (3.35)). However, since the sine transfer function is a memoryless nonlinearity, i.e. it only depends on the instantaneous value of the input signal, it can be compensated through calibration by inverting the nonlinear response. In the case of an MZM biased at the null, a simple arcsin function can be applied to the received samples $x[t]$ [143, 144]

$$x_c[t] = \sin^{-1}\left(\frac{x[t]}{A}\right) \tag{4.2}$$

to give the compensated time sequence $x_c[t]$. The constant A is a simple scalar factor that depends on the overall ‘gain’ of the dual comb system and can be calibrated easily. This A was calibrated for the dual comb system by maximising the overall IMD3 on a received test sequence and applied to the received data in Fig 4.10. The IMD3 and SINAD after compensation are plotted in Fig 4.10(a) for comparison, labelled as IMD3 (comp.) and SINAD (comp.) respectively. The arcsin compensation improves the IMD3 by over 30 dB and allows for the compensated SINAD to simply track the stochastic SNR across the entire input signal power range. In the specific example of at 20 dBm shown in Fig 4.10(b)/(c), the power of the third order harmonic distortion is reduced by 30 dB in the compensated signal, as shown plotted in orange. These results demonstrate that the distortions introduced by the MZM can be compensated by simple static digital signal processing (DSP) and do not prevent the dual comb system from reaching the limits imposed by the stochastic noise sources, even in scenarios where the MZM is operated in the strongly nonlinear regime. Unlike previous demonstrations of arcsin compensation of the MZM response in analog photonic links [143, 144], this implementation must also account for the differential delay and gain between the channels, which must be calibrated before applying the arcsin compensation.

4.3 Summary

In this Chapter the performance of dual frequency comb ADCs was investigated. Firstly, the relative phase noise of coherent electro-optic frequency combs was measured, showing that at high offset frequencies, the phase noise is an incoherent sum of the timing phase noise of the two combs, multiplied by line number. At low offset frequencies, however, the phase noise scales more slowly due to the coherence of the common frequency reference.

Secondly, a low phase noise dual frequency comb ADC prototype was built and its performance was evaluated using the sine wave testing. At 40 GHz, the dual comb ADC achieves 44 dB SNR, equivalent to 7.0 bits ENOB, outperforming all electronic ADC results and is equivalent to the best reported results of time interleaving photonic ADCs. Finally, it was shown that nonlinear harmonic distortions introduced by the MZM can be suppressed by over 30 dB through simple arcsin compensation, allowing the ADC to achieve the SINAD levels only limited by stochastic noise sources.

Chapter 5

Arbitrary signal detection using dual combs

Having characterised the performance of the ADC through modelling in Chapter 3 and experiment in Chapter 4, this Chapter discusses how the dual comb system can be used to detect arbitrary input signals. A novel method is first described in order to detect an arbitrary signal within each sub-band using the upper and lower comb lines of the dual frequency comb system, which requires phase stabilisation between the signal and reference combs. It is shown that this method, unlike results presented in Chapter 4 allows for distinguishing between sub-band frequency component conjugates without significant loss in performance or use of sub-band coherent receivers. Finally, the impact of phase locking errors is explored using sine wave testing and M-ary quadrature amplitude modulated data signals are detected using the proposed dual comb ADC.

5.1 Theoretical description

The experimental results presented in this thesis so far were based on balanced detection of each frequency sub-band in the dual comb ADC. Although this method allows for high performance digitisation as demonstrated in Chapter 4, it does not allow for the detection of arbitrary signals such as phase and amplitude modulated digital communications signals across the entire ADC bandwidth. Here, we derive a method to detect arbitrary signals across the dual comb ADC without the use of sub-band coherent receivers.

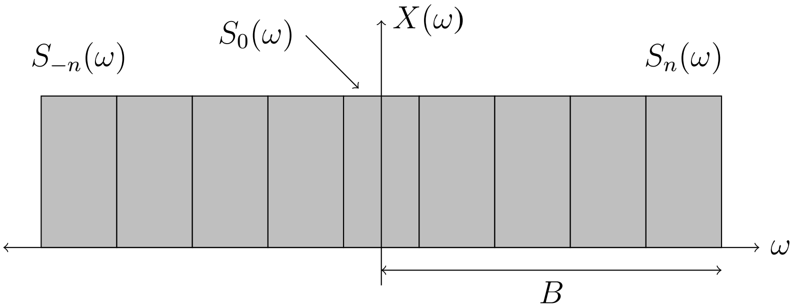

Fig. 5.1: A real signal of bandwidth B can be divided into $2N + 1$ complex sub-bands of bandwith $\Delta\omega$.

Consider an arbitrary real input signal $x(t)$. For our analysis, let us divide its Fourier transform $X(\omega)$ into $2N+1$ complex sub-bands S_n, as depicted in Fig 5.1

$$X(\omega) = \sum_{n=-N}^{N} S_n(\omega + n\Delta\omega) \tag{5.1}$$

where

$$S_n(\omega) = \begin{cases} X(\omega - n\Delta\omega) & \text{if } -\frac{\Delta\omega}{2} < \omega < \frac{\Delta\omega}{2} \\ 0 & \text{otherwise.} \end{cases}$$

In the time domain

$$x(t) = \sum_{n=-N}^{N} s_n(t) e^{in\Delta\omega t} \tag{5.2}$$

with $s_n(\omega)$ as the Fourier transform of its corresponding sub-band $S_n(\omega)$. Since $x(t)$ is real, $X(\omega)$ has the symmetry $X(\omega) = X^*(-\omega)$ and the sub-bands have the corresponding symmetry $S_n(\omega) = S^*_{-n}(\omega)$, $s_n(t) = s^*_{-n}(t)$. Now, assume we have dual frequency combs of spacing ω_{sig} and $\omega_{LO} = \omega_{sig} + \Delta\omega$ as per our analysis in Chapter 3, (3.7)/(3.8)

$$E_{sig}(t) = \sum_{n=-N}^{N} \sqrt{P_{sig,n}} e^{i(\omega_0 + n\omega_{sig})t}, \tag{5.3}$$

$$E_{LO}(t) = \sum_{n=-N}^{N} \sqrt{P_{LO,n}} e^{i(\omega_0 + n\omega_{LO})t}, \tag{5.4}$$

where we have disregarded phase noise for simplicity. We can apply a phase shift to the LO comb through a simple time delay Δt as in the setup shown in Fig. 5.2. Since $\omega_0 \gg \omega_{sig}, \omega_{LO}$, applying the time delay $\Delta t = -\pi/4\omega_0$ is equivalent to rotating the phase of every comb line by $-\pi/4$ and multiplying (5.4) by the factor $e^{-i\pi/4}$

$$E_{LO}(t) = \sum_{n=-N}^{N} \sqrt{P_{LO,n}} e^{i(\omega_0 + n\omega_{LO})t} e^{-i\frac{\pi}{4}}. \tag{5.5}$$

Our input signal $x(t)$ is then modulated onto the signal comb with an intensity modulator. We assume the modulator is ideal, with both perfect linearity and maximum extinction ratio, for the purpose of this analysis. Next, the modulated signal comb and the LO comb are combined via a 50:50 coupler. The transfer function of a 50:50 coupler means that the LO field in the lower arm has a phase shift of π relative to signal field compared to the upper arm. Subsequently, the upper branch field, $E_+(t)$, and lower

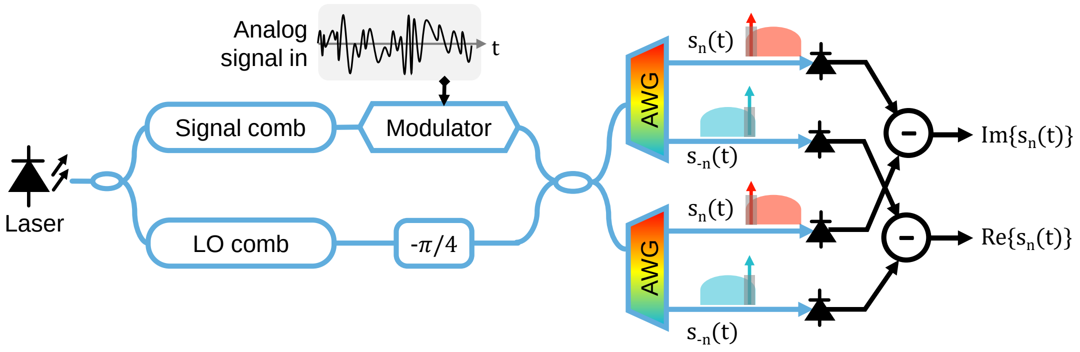

Fig. 5.2: Phase locking the two frequency combs with a relative phase offset of $-\pi/4$ allows for full arbitrary detection of each sub-band.

branch field, $E_-(t)$, are:

$$E_\pm(t) = x(t)\sum_{n=-N}^{N}\sqrt{\frac{P_{sig,n}}{2}}e^{i(\omega_0+n\omega_{sig})t} \pm \sum_{n=-N}^{N}\sqrt{\frac{P_{LO,n}}{2}}e^{i(\omega_0+n\omega_{LO})t}e^{-i\frac{\pi}{4}} \tag{5.6}$$

Both $E_+(t)$ and $E_-(t)$ are subsequently filtered by an arrayed waveguide grating or other optical de-multiplexing device. Considering the n-th tone, we have

$$E_{\pm,n}(t) = x(t)\sqrt{\frac{P_{sig,n}}{2}}e^{i(\omega_0+n\omega_{sig})t} \pm \sqrt{\frac{P_{LO,n}}{2}}e^{i(\omega_0+n\omega_{LO})t}e^{-i\frac{\pi}{4}} \tag{5.7}$$

$$= e^{i(\omega_0+n\omega_{sig})t}\left[x(t)\sqrt{\frac{P_{sig,n}}{2}} \pm \sqrt{\frac{P_{LO,n}}{2}}e^{in\Delta\omega t}e^{-i\frac{\pi}{4}}\right] \tag{5.8}$$

The optical signals are incident on photodiodes of responsivity R, producing currents

$$I_{\pm,n}(t) = R\left[\frac{P_{sig,n}^2|x(t)|^2}{2} + \frac{P_{LO,n}^2}{2} \pm \sqrt{P_{sig,n}P_{LO,n}}\,\mathrm{Re}\left\{x(t)e^{-in\Delta\omega t}e^{i\frac{\pi}{4}}\right\}\right] \tag{5.9}$$

with balanced detection assuming $R = 1$ and plugging in (5.2)

$$I_n(t) = I_{+,n}(t) - I_{-,n}(t) \tag{5.10}$$

$$= 2\sqrt{P_{sig,n}P_{LO,n}}\,\mathrm{Re}\left\{x(t)e^{-in\Delta\omega t}e^{i\frac{\pi}{4}}\right\} \tag{5.11}$$

$$= 2\sqrt{P_{sig,n}P_{LO,n}}\,\mathrm{Re}\left\{e^{-in\Delta\omega t}e^{i\frac{\pi}{4}}\sum_{n'=-N}^{N}s_{n'}(t)e^{in'\Delta\omega t}\right\} \tag{5.12}$$

Noting that as defined, $S_n(\omega) = 0$ for $\omega > (n+\frac{1}{2})\Delta\omega$ and $\omega < (n-\frac{1}{2})\Delta\omega$, applying a brick wall low pass filter of bandwidth $\frac{\Delta\omega}{2}$ gives us

$$I_n(t) = 2\sqrt{P_{sig,n}P_{LO,n}}\,\mathrm{Re}\left\{e^{i\frac{\pi}{4}}s_n(t)\right\} \tag{5.13}$$

Now, considering the current generated for $-n$-th channel

$$I_{-n}(t) = 2\sqrt{P_{sig,-n}P_{LO,-n}}\,\mathrm{Re}\left\{e^{i\frac{\pi}{4}}s_{-n}(t)\right\} \tag{5.14}$$

and given the aforementioned symmetry $s_n(t) = s^*_{-n}(t)$, we can write

$$\begin{aligned} I_{-n}(t) &= 2\sqrt{P_{sig,-n}P_{LO,-n}}\,\mathrm{Re}\left\{e^{i\frac{\pi}{4}}s^*_n(t)\right\} && (5.15)\\ &= 2\sqrt{P_{sig,-n}P_{LO,-n}}\,\mathrm{Re}\left\{[e^{-i\frac{\pi}{4}}s_n(t)]^*\right\} && (5.16)\\ &= 2\sqrt{P_{sig,-n}P_{LO,-n}}\,\mathrm{Re}\left\{e^{-i\frac{\pi}{4}}s_n(t)\right\}. && (5.17) \end{aligned}$$

Combining the detected currents $I_n(t)$ and $I_{-n}(t)$ to give the complex output for the n-th sub-band, assuming for simplicity that $P_{sig,n} = P_{sig,-n}$ and $P_{LO,n} = P_{LO,-n}$

$$\begin{aligned} y_n(t) &= I_n(t) + iI_{-n}(t) && (5.18)\\ &= 2\sqrt{P_{sig,n}P_{LO,n}}\Bigg[\frac{1}{\sqrt{2}}\big(\mathrm{Re}\{s_n(t)\} - \mathrm{Im}\{s_n(t)\}\big) \\ &\qquad + \frac{i}{\sqrt{2}}\big(\mathrm{Re}\{s_n(t)\} + \mathrm{Im}\{s_n(t)\}\big)\Bigg] && (5.19)\\ &= 2\sqrt{P_{sig,n}P_{LO,n}}\frac{1}{\sqrt{2}}(1+i)(\mathrm{Re}\{s_n(t)\} + i\,\mathrm{Im}\{s_n(t)\}) && (5.20)\\ &= 2\sqrt{P_{sig,n}P_{LO,n}}e^{i\frac{\pi}{4}}s_n(t). && (5.21) \end{aligned}$$

Here we have recovered the full complex sub-band scaled by a constant $2\sqrt{P_{sig,n}P_{LO,n}}$ and phase rotation $\pi/4$, allowing us to recover an arbitrary signal within each sub-band. Simultaneous detection of every sub-band therefore allows us to recover the full input signal $x(t)$. Note that for the special case of $n = 0$, $s_0(t)$ is real and therefore can be detected by a single balanced detector using (5.13). Furthermore, it is straightforward to see that locking the phase difference at $\Delta t = \pi/4\omega_0$ will result in the I and Q components simply being detected at opposite channels than is described in (5.5)-(5.18).

This method of using the upper and lower tones of the frequency combs to detect the full field of each sub-bands eliminates the need for a full coherent receiver for each channel compared to a more conventional setup as shown, for example, in Fig. 3.3. The lack of a 90 degree hybrid and use of the upper and lower sidebands increases the optical power incident on each photodiode fundamentally by 3 dB. This is without considering the additional insertion losses which often approach an additional 3 dB of loss, or 6 dB in total. This will increase the SNR by 6 dB in a shot noise limited system, as per (3.33), or 12 dB in a thermal noise limited system as per (3.34). Even if a second set of coherent receivers are used to detect the lower sidebands simultaneously, this will only increase the SNR of a coherent receiver based system by 1.5 dB. In addition, our design reduces the size, complexity and cost of the system which leads to a reduced device footprint in an integrated system.

5.2 Impact of phase locking error

In Section 5.1, we described how locking the relative phase between the LO and signal combs allows for detection of arbitray complex signal within each sub-band by detecting the upper and lower sidebands of the dual frequency combs. In practice, applying a fixed phase rotation to a time varying signal requires simply applying a fixed path (and therefore time) delay to the signal compared to its reference. In reality, it is unlikely that a real system can apply a precise phase lock due to errors in applying the fixed path delay. In this Section we discuss how this error may affect system performance.

Imagine that the actual phase rotation applied in (5.5) is instead offset with an error ϵ_θ, leading to an actual phase shift of $-\frac{\pi}{4} + \epsilon_\theta$. This modifies (5.13) and (5.14) to

$$I_n(t) = 2\sqrt{P_{sig,n} P_{LO,n}} \operatorname{Re}\left\{ e^{i(\frac{\pi}{4} - \epsilon_\theta)} s_n(t) \right\} \tag{5.22}$$

and

$$I_{-n}(t) = 2\sqrt{P_{sig,-n} P_{LO,-n}} \operatorname{Re}\left\{ e^{i(\frac{\pi}{4} - \epsilon_\theta)} s_{-n}(t). \right\} \tag{5.23}$$

respectively. For simplicity we can make the substitution $s_n(t) = e^{-i\frac{\pi}{4}} s_n(t)$, giving

$$I_n(t) = 2\sqrt{P_{sig,n} P_{LO,n}} \operatorname{Re}\left\{ e^{-i\epsilon_\theta} s_n(t) \right\} \tag{5.24}$$

$$I_{-n}(t) = 2\sqrt{P_{sig,-n} P_{LO,-n}} \operatorname{Re}\left\{ -ie^{i\epsilon_\theta} s_n(t) \right\}. \tag{5.25}$$

We can then write

$$I_n(t) = 2\sqrt{P_{sig,n} P_{LO,n}} \operatorname{Re}\left\{ e^{-i\epsilon_\theta} s_n(t) \right\} \tag{5.26}$$

$$I_n(t) = 2\sqrt{P_{sig,n} P_{LO,n}} \Big[\cos\epsilon_\theta \operatorname{Re}\left\{ s_n(t) \right\} + \sin\epsilon_\theta \operatorname{Im}\left\{ s_n(t) \right\} \Big] \tag{5.27}$$

and

$$I_{-n}(t) = 2\sqrt{P_{sig,-n} P_{LO,-n}} \operatorname{Re}\left\{ -ie^{i\epsilon_\theta} s_n(t) \right\} \tag{5.28}$$

$$I_{-n}(t) = 2\sqrt{P_{sig,-n} P_{LO,-n}} \Big[\cos\epsilon_\theta \operatorname{Im}\left\{ s_n(t) \right\} + \sin\epsilon_\theta \operatorname{Re}\left\{ s_n(t) \right\} \Big]. \tag{5.29}$$

Our formulation in (5.3)-(5.18) showed that the full complex sub-band $s_n(t)$ can be reconstructed as

$$s_n(t) = I_n(t) + iI_{-n}(t) \tag{5.30}$$

scaled by some constant and phase rotation, assuming for simplicity that $P_{sig,n} = P_{sig,-n}$ and $P_{LO,n} = P_{LO,-n}$. Plugging in (5.27) and (5.29)

$$\begin{aligned} I_n(t) + iI_{-n}(t) \propto \cos\epsilon_\theta \operatorname{Re}\{s_n(t)\} + \sin\epsilon_\theta \operatorname{Im}\{s_n(t)\} \\ + i\Big[\cos\epsilon_\theta \operatorname{Im}\{s_n(t)\} + \sin\epsilon_\theta \operatorname{Re}\{s_n(t)\}\Big] \end{aligned} \tag{5.31}$$

$$\propto \cos\epsilon_\theta s_n(t) + i\sin\epsilon_\theta s_n^*(t) \tag{5.32}$$

which is the undesired conjugate $s_n^*(t)$ interfering with the signal. Clearly, for the case $\epsilon_\theta = 0$ the conjugate is completely eliminated in (5.32) and the sub-band $s_n(t)$ is received as desired. On the other hand, locking to $-\pi/4$ will give us an error of $\epsilon_\theta = \pi/2$ and mean that the conjugate $s_n^*(t)$ is received. In the frequency interleaving dual comb architecture, this will lead to misidentification of a frequency component as its opposite sideband counterpart within the specific sub-band. For example, a 2.8 GHz signal detected in the 3rd channel will be detected as a 3.2 GHz signal or vice versa. Since the phase locking is performed across the entire bandwidth, this sub-band conjugate error will be consistent across the every channel in the dual comb ADC. If this error is static, it is therefore correctable through a calibration routine.

In the worst case, $\epsilon_\theta = \pi/4$ leading to

$$\cos\frac{\pi}{4}s_n(t) + i\sin\frac{\pi}{4}s_n^*(t) = \frac{1}{\sqrt{2}}\operatorname{Re}\{s_n(t)\} \tag{5.33}$$

and only the real part of the signal is received, which prohibits full reconstruction of an arbitrary signal across the entire ADC bandwidth. The same is true for $\epsilon_\theta = -\pi/4$, where only the imaginary part of the signal is received.

The SNR resulting from this phase locking error and the resulting interfering conjugate can be estimated by comparing the relative power of the desired signal $s_n(t)$ and the interfering conjugate $s_n^*(t)$

$$\text{SNR} = \frac{(\cos\epsilon_\theta s_n(t))^2}{(\sin\epsilon_\theta s_n^*(t))^2} = \frac{1}{\tan^2\epsilon_\theta} \tag{5.34}$$

which in dB is

$$\text{SNR} = -20\log_{10}(\tan\epsilon_\theta). \tag{5.35}$$

This SNR limit is plotted in Fig. 5.3, which suggests that the dual comb ADC is highly sensitive to errors in the phase locking between the signal and LO comb. To achieve an SNR above 50 dB, Fig. 5.3(b) shows that the combs need to be phase locked with a tolerance of < 0.2 degrees, which although possible on an integrated platform, would make using a discrete component based dual comb system for testing of arbitrary signal detection at high SNRs prohibitive.

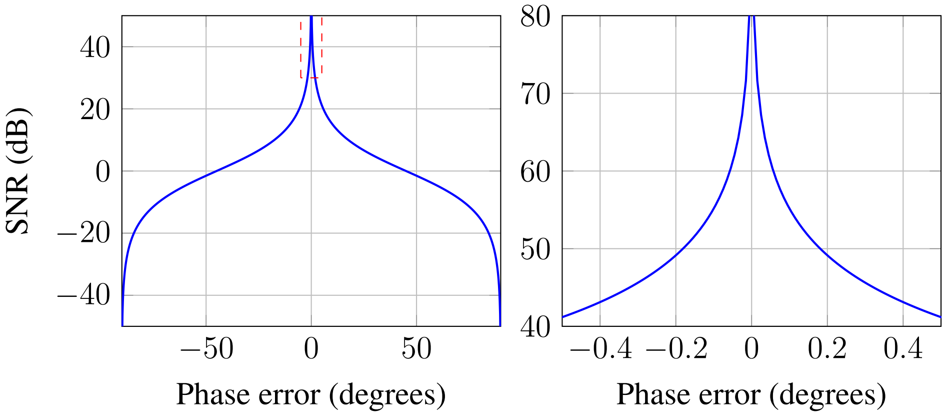

Fig. 5.3: SNR limit due to phase locking error. The red box highlighted in (a) is plotted in (b) to show the SNR at small phase errors.

Note however that the qualitative effect of a phase locking error ϵ_θ is to convert the ideally orthogonal received currents $I_n(t), I_{-n}(t)$ into the non-orthogonal currents (5.27) and (5.29). Fortunately, a number of techniques exist that can orthogonalise a set of non-orthogonal samples which have been widely used to combat the analogous phase offset error that can occur in coherent receivers, examples of which include the Gram-Schmidt orthogonalisation procedure (GSOP) or Loewdin Symmetric Orthogonalization [183, 184].

If the system can be orthogonalised, then the received samples can be transferred to an orthogonal basis set and the interfering conjugate shown in (5.32) is eliminated from the received signal. That is, we can find a basis set such that (5.32) becomes

$$\mathrm{Orth}\left\{I_n(t) + iI_{-n}(t)\right\} = e^{i\alpha} \cos \epsilon_\theta s_n(t) \tag{5.36}$$

where $e^{i\alpha}$ is some arbitrary phase rotation and $\mathrm{Orth}\{\cdot\}$ is the orthogonalisation operator. However, although many orthogonalisation techniques exist, the original signal was still detected by a non orthogonal axes set which is the origin of the scaling factor $\cos \epsilon_\theta$ in (5.36), as is illustrated in Fig. 5.4(a). This has the effect of reducing the dynamic range of the receiver and inducing an SNR penalty of

$$\mathrm{SNR} = -20 \log_{10}(\cos \epsilon_\theta) \tag{5.37}$$

as plotted in Fig. 5.4(b). This significantly relaxes the SNR penalty for any phase locking error, with as plotted in Fig. 5.4(b) showing that an up to 20 degrees error can be tolerated with a <1 dB reduction in dynamic range.

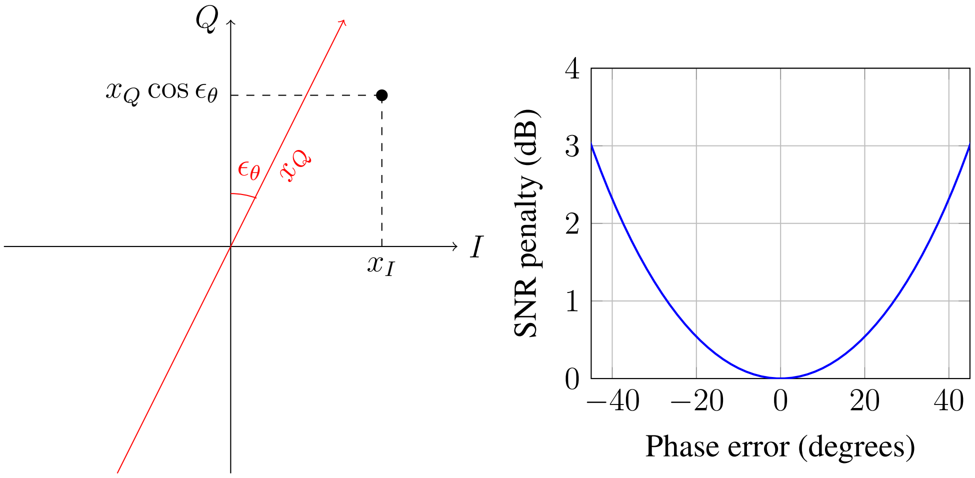

Fig. 5.4: (a) An error in the phase difference between two combs, from the ideal $-\pi/4$, results in non-orthogonality of the received signal. An orthogonalisation procedure allow for the projection of the detected x_Q onto the orthogonal basis but reduces its amplitude by $\cos\theta$, and therefore reduces the sensitivity of the receiver. (b) Calculated SNR penalty for an orthogonalised signal vs phase error.

5.3 Phase error at high channel counts

Even if the desired phase delay can be applied accurately, since the delay required to induce a specific phase rotation is strictly related to the signal frequency, it is not technically possible to apply a fixed phase rotation using a time delay across a broad bandwidth in a non-dispersive medium.

In our dual comb application, the delay is applied based on the central comb line which is at frequency ω_0 to create a phase rotation of $-\pi/4$. According to the scheme described in Section 5.1, the corresponding time delay applied is therefore $\Delta t = -\pi/4\omega_0$. At channel n, this leads to an actual phase rotation of

$$\Delta\phi = -\frac{\pi}{4} - \frac{n\omega_{LO}\pi}{4\omega_0} \tag{5.38}$$

$$= -\frac{\pi}{4}\left[1 + \frac{n\omega_{LO}}{\omega_0}\right] \tag{5.39}$$

with the error given by $\frac{n\omega_{LO}}{\omega_0} = \frac{nf_{LO}}{f_0}$. The magnitude of this phase error is plotted in Fig. 5.5. For the parameters demonstrated in Chapter 4, i.e. $f_{sig} = 25$ GHz and 12 channels, the fractional phase error is quite small at approximately 10^{-3}. However, if the number of channels increases to 100 or even 1000, the phase error can be significant, especially if operating with a high repetition rate, f_{LO}, frequency comb. With $f_{LO} = 400$ GHz, the fractional phase error exceeds 1 (i.e. a phase error magnitude larger than $\pi/4$) at 500 channels. Although an extreme example, these parameters might be reached if implementing a dual comb system with Kerr comb based microresonator rings, which can have repetition rates in the 100s of GHz and high numbers of comb lines.

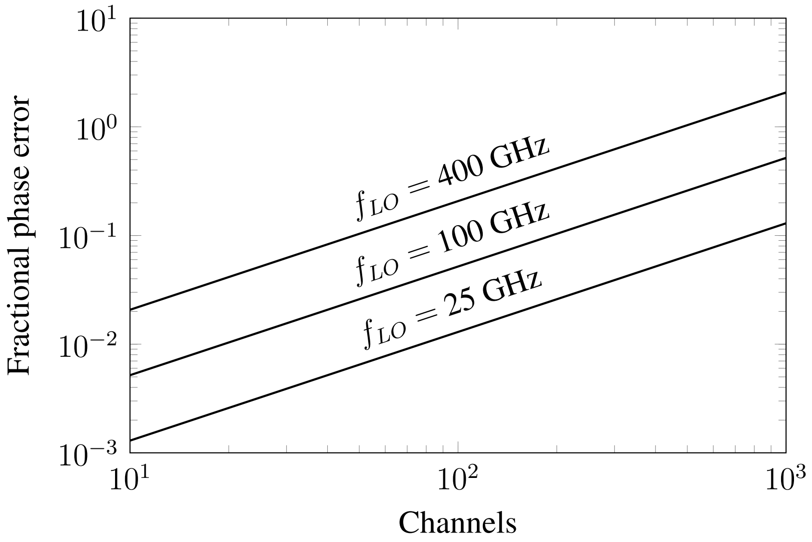

Fig. 5.5: Fractional phase error as a function of channel count for various comb spacing frequencies f_{LO}. The optical frequency is assumed to be $\frac{\omega_0}{2\pi} = f_0 = 193$ THz.

5.4 Experiments to detect arbitrary waveforms

In order to test arbitrary sub-band detection, the setup shown in Fig. 4.4 was modified to enable detection of an arbitrary signal within a single sub-band. Three principal changes were made to the modified setup as shown in Fig. 5.6.

Firstly, a feedback loop was implemented to stabilise the phase between the signal and reference comb at $-\pi/4$ as described in Section 5.1. The 0th channel, i.e. the channel containing the central comb line, from one of the arrayed waveguide gratings was incident on a single photodiode whose output current was used as the process variable in a digital PID controller. Changes in the relative phase between the two branches results in the light being switched between the two AWG branches and a subsequent change in optical intensity and the feedback photodiode. By sweeping the phase using the PID controller, the phase shifter voltage set point corresponding to the desired relative phase between the two combs can be inferred. Once the set point is observed, the phase between the two combs can be locked using a PID loop, which had an approximate loop bandwidth of around 2 kHz. This loop bandwidth was sufficient to compensate for thermal and mechanical induced phase shifts in the fiber, combined with passive techniques to insulate the fibers as much as possible from environment induced relative phase shifts.

Secondly, two synchronous channels were implemented to receive both the n-th and $-n$-th channels as required for arbitrary sub-channel reception. Both channels had nominally identical balanced photodiodes, TIAs and low pass filters, and were detected

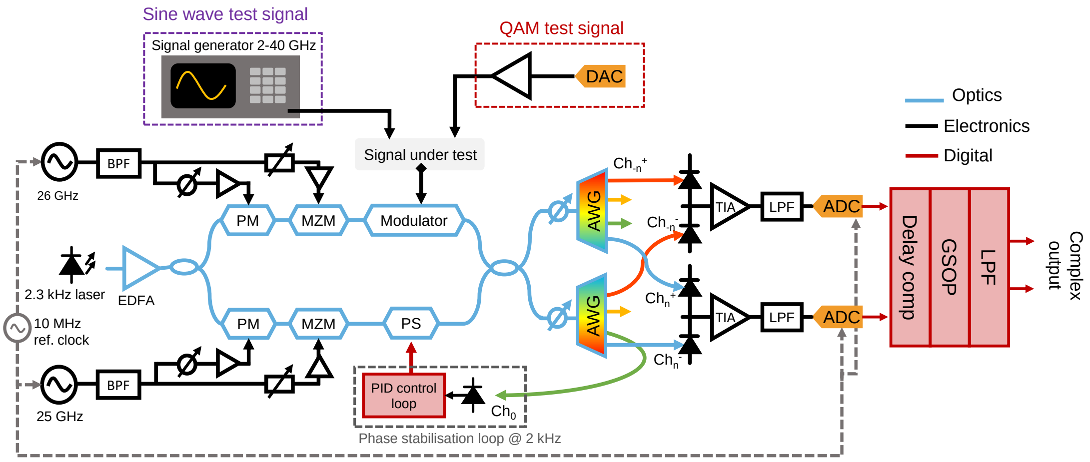

Fig. 5.6: Experimental setup. MZM, Mach-Zehnder modulator; PM, phase modulator; BPF, band-pass filter; EDFA, erbium-doped fiber amplifier; AWG, arrayed waveguide grating; Ch, channel; TIA, transimpedance amplifier; ADC, analog to digital converter; LPF, low pass filter; PID, proportional-integral-derivative; GSOP, Gram-Schmidt orthogonalisation procedure; PS, phase shifter.

by synchronous ADCs. The ADCs were two channels on the same Analog Devices AD9209 chip: synchronous captures were serialised and streamed off of the ADC onto an FPGA for transfer to a PC and offline processing.

Thirdly, delay compensation and othogonalisation using GSOP was implemented offline, along with a 500 MHz bandwidth digital low pass filter. The delay compensation applied a phase shift between the detected n-th and $-n$-th channels that corresponded to the difference in fiber delay between the two channels. A 16-QAM test signal, centred in the channel under test was sent to calibrate this delay which was measured to be 207 ps, corresponding to a physical fiber delay of 4.3 cm. This delay is a result of manufacturing variation in the length of the fiber pigtails from the AWGs used in this experiment.

5.4.1 Unambiguous sine wave detection

A sine wave test signal was used to demonstrate that the scheme described in Section 5.1 was capable of distinguishing symmetric frequencies between the upper and lower sidebands of a sub-channel, using the setup shown in Fig. 5.6. For example, the setup used in Chapter 4 would be unable to distinguish between a 2.8 GHz and 3.2 GHz signal, which would both appear as a 200 MHz signal in the n-th channel. This limitation effectively limits the bandwidth of each sub-band to $\Delta f/2$, or 500 MHz in this case.

A 2.8 GHz sine wave is used as the input signal and is detected simultaneously in the (a) 3rd and (b) -3rd channel, as shown in Fig. 5.7(a) and Fig. 5.7(b) respectively. The observed SINAD and SFDRs are 45.3 dB/46.0 dB and 55.2 dB/64.9 dB, which as

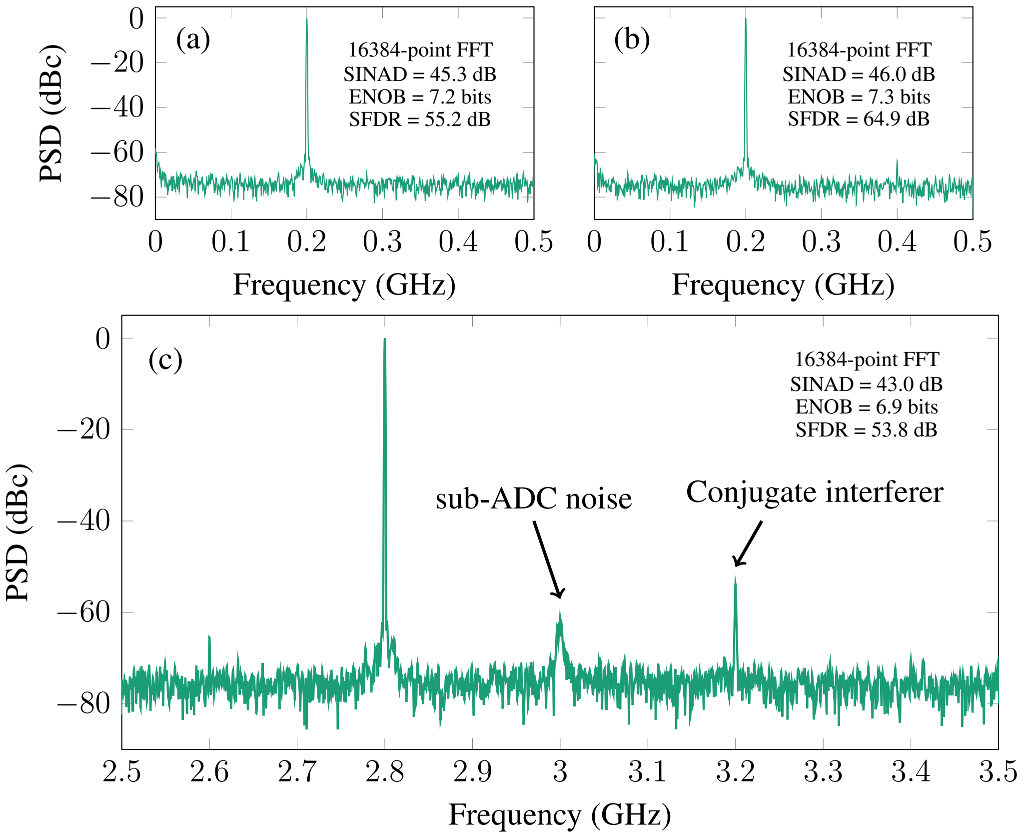

Fig. 5.7: Received spectrum in (a) 3rd and (b) -3rd channel for a 2.8 GHz input signal. (c) Full complex sub-band reception, with the phase difference locked at $\pi/4$. All spectra are an average of 4 16384-point FFTs.

expected are in agreement with the results presented in Chapter 4. The subsequent full received baseband resulting from coherent combination of these two channels is shown in Fig 5.7(c), with the observed signal being correctly identified as having a frequency of 2.8 GHz. The SINAD and SFDR are slightly degraded to 43.0 dB and 53.8 dB respectively compared to the individual detection of the I and Q components. This drop in performance can be attributed to several causes.

Firstly, the ADCs used exhibit significant flicker noise that can clearly be observed as a relatively broad peak around ‘DC’ component that has been upshifted to 3 GHz in Fig 5.7(c). This low frequency noise is a feature of the AD9209 that has been observed in electrical back to back experiments and is a result of the AD9209 and the evaluation board used being primarily designed for reception of non-baseband centred wireless and radar signals using the onboard digital down-conversion. To realise the full performance of the dual comb ADC, care must be taken to use sub-ADCs that can operate with low noise from the channel baseband DC to $\Delta f/2$, since this low frequency noise will appear at every $n\Delta f$ in a full bandwidth implementation.

Secondly, the non-orthogonality of the 3rd and -3rd channel, as discussed in Section 5.2 means that the 3.2 GHz interfering conjugate is not fully suppressed, likely because the phase locking at $-\pi/4$ had some error. Since the $-\pi/4$ locking set point voltage was judged by simply observing the scanned response of the feedback circuit, the precision of the phase locking is only around +/- 5 degrees. If implemented on a integrated platform, much greater phase control could be achieved, potentially without active feedback simply by matching the optical path length of the two combs to achieve the $-\pi/4$ phase difference. In any case, the conjugate interferer at 3.2 GHz is still suppressed to 53.8 dB in this demonstration, which is sufficient to avoid meaningfully degrading the observed SINAD.

To further investigate the effect of phase locking error on the suppression of conjugate interferer and therefore SINAD of the dual comb system, a second experiment was performed using the setup shown in Fig. 5.6. As before, the input test signal was a 2.8 GHz sine wave and both the -3rd and 3rd channel were detected synchronously. However, instead of locking the phase offset at the desired $-\pi/4$, the phase shifter was driven with a triangular wave at 200 Hz, which induced a slow, time varying phase offset between the signal and reference comb.

A large capture of 2^{20} samples was then obtained. This large capture was then divided into segments of length 2^{12} samples offline, with the aforementioned delay compensation and low pass filtering applied to each segment. Since the phase offset is varying with time across the large 2^{20} sample count capture, the relative strength of the desired 2.8 GHz signal and the 3.2 GHz conjugate interferer can be calculated for a specific phase offset and compared to the predictions made in Section 5.2.

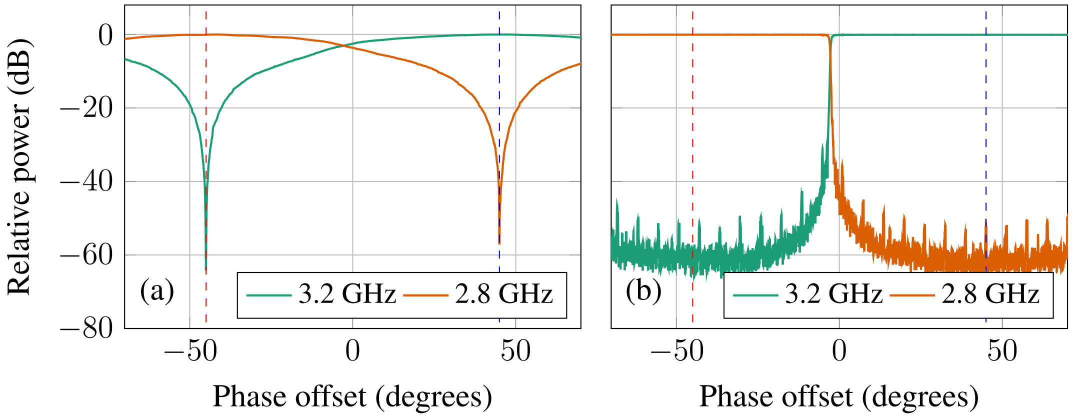

Fig. 5.8: Relative power of the sub-band conjugates 2.8 GHz and 3.2 GHz detected in the -3rd and 3rd channel, with (a) no GSOP (b) GSOP applied. Red and blue dashed lines indicate -45 degrees and 45 degrees phase lock respectively.

The relative strengths of the 2.8 GHz signal and the 3.2 GHz interferer without orthogonalisation are plotted in Fig. 5.8(a). The observed relative strengths show close agreement with the prediction of (5.35) and Fig. 5.3. Peak suppression of the conjugate is achieved at -45 degrees ($-\pi/4$) and the suppression of the 2.8 GHz signal is achieved at 45 degrees ($\pi/4$), which represents misidentification of the signal as its sub-band conjugate. At 0 degrees, the upper and lower sidebands are equal in strength: in this case only the real part of the signal is detected and the full arbitrary sub-band cannot be detected.

Fig. 5.8(a) further confirms that the dual comb ADC is very sensitive to phase offset errors, unless an orthogonalisation procedure can be applied. Fig. 5.8(b) shows presents the same data as Fig. 5.8(a) but with GSOP applied. GSOP significantly improves the phase error tolerance, with a error of over 20 degrees required before any rise in the strength of the suppressed conjugate is observed which is otherwise suppressed to >50 dB. Once the phase error exceeds 45 degrees, the GSOP procedure still misidentifies the test signal as its sub-band conjugate, since it is agnostic to the signal input.

5.4.2 QAM detection

The experimental setup in Fig. 5.6 was further used to evaluated the performance of the dual comb ADC in receiving broadband data signals that are representative of what is typically transmitted in digital communications links. The dual comb was driven with an 500 MBd root-raised-cosine (RRC, roll-off factor $= 0.1$) shaped 16-QAM signal generated by a 16-bit 1.5 GSPS digital to analog converter. The baseband signal, whose spectrum is shown in Fig 5.9(b), is up-converted to a 2.3 GHz carrier by the digital up-conversion and then amplified to approximately 10 dBm average power by an external broadband amplifier (noise figure = 1.5 dB).

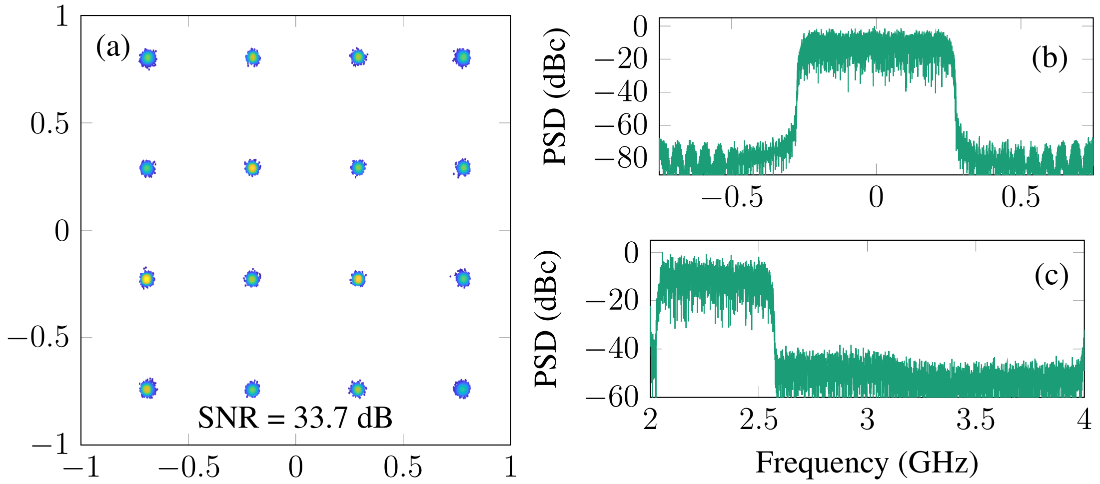

Fig. 5.9: RRC-shaped 500 MBd 16-QAM signal with 2.3 GHz carrier detected in the dual comb 2nd channel. (a) Constellation diagram of received symbols. (b) Transmitted baseband spectrum. (c) Received spectrum in the 2nd channel.

The carrier frequency of 2.3 GHz was chosen in this initial experimental to be offset from Δf to ensure that the signal could be detected by a single channel (i.e. the 2nd channel) without implementing the phase locking discussed earlier in this Chapter that would be required if, for example, the signal was centred at 2 GHz. This allows for evaluation of the system performance and comparison with the sine wave testing results shown in Chapter 4 without any performance degradation arising from phase stability issues discussed in the previous section.

A relatively narrowband signal of 500 MBd was used for two reasons. Firstly, detection of a sub-band limited signal (i.e. $< \Delta f$) does not require any channel stitching DSP to be implemented which, although required for the full broadband implementation of a dual comb ADC, is beyond the scope of this thesis. Secondly, generating a broadband signal of sufficient quality to test the performance of the dual comb ADC is not possible given current DAC technology and the observed SNR in such an experiment would be DAC limited. On the other hand, the SNR of the generated 500 MBd 16-QAM signal, when measured directly at the DAC output is > 45 dB, which is sufficient to test the performance of the dual comb ADC. From these narrowband tests, the fundamental performance of a full bandwidth dual comb ADC can then be inferred.

A matched RRC filter was applied to the received signal followed by a 21-tap linear equaliser that was trained using the least means squared method. The equaliser is compensating for DAC ripple, transmit amplifier roll-off, as well as the frequency response of the dual comb system which is contributed by the MZM, and photodiode-TIA circuit. The received symbols are shown as a constellation diagram in Fig. 5.9(a), along with the received spectrum in the 2nd dual comb channel in Fig. 5.9(c).

The observed SNR, calculated by comparing the received signals to the transmitted symbols, is 33.7 dB, which is substantially below that predicted by the sine wave testing shown in Fig. 4.10(a) at comparable drive powers (40 dB). The principal reason for this is the limited CMRR of the balanced detector (35 dB) that leads to significant SSBI when detecting broadband signals. This effect is not observed when detecting sine wave signals since the SSBI term will be DC and therefore eliminated by the blocking capacitors of the photodetector-TIA circuit. SSBI can be observed clearly on the received spectrum when shifting the signal away from the channel baseband. For example, increasing the carrier frequency to 2.7 GHz results in more of the SSBI being located out of the signal band leading to an increased SNR of 38 dB.

To show the capability of the dual comb system to detect arbitrary signals across each sub-band, the same RRC shaped 16-QAM signal was also received with a carrier frequency of 2 GHz. In this case, phase locking at $-\pi/4$ and detection of both the 2nd and -2nd channels are required to detect the full complex sub-band signal using the setup in Fig. 5.6. In addition to the DSP described for Fig. 5.9, IQ delay compensation and GSOP were applied in offline processing, as for the experiments described in Section 5.4.1.

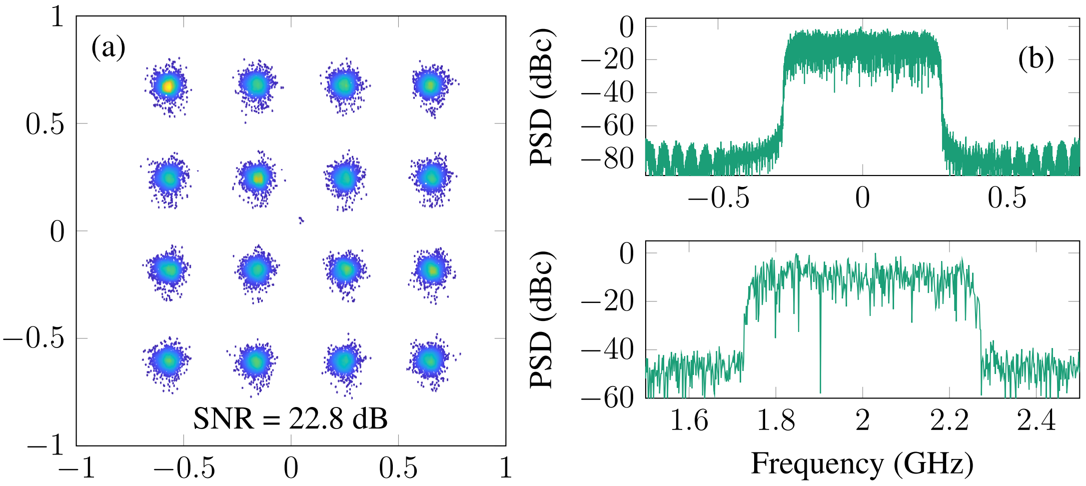

Fig. 5.10: RRC-shaped 500 MBd 16-QAM signal with 2 GHz carrier detected in the dual comb 2nd channel. (a) Constellation diagram of received symbols. (b) Transmitted baseband spectrum. (c) Received complex baseband in the 2nd channel.

The received symbols shown in Fig. 5.10(a) confirm that the phase locking at $-\pi/4$ allows for reconstruction of an arbitrary signal across the full sub-band bandwidth, with the received spectrum after GSOP and I/Q delay compensation shown in Fig. 5.10(c). However, the SNR is significantly less than that achieved for the single balanced detector reception shown in Fig. 5.9 at 22.8 dB. The comparatively low SNR may be due to a number of issues. One possible contributing factor is the poor performance sub-ADC (Analog devices AD9209) in receiving baseband signals. This poor performance was also observed in electrical back to back reception of PAM4 modulated signals using the AD9209 and can be ascribed to the ADC being primarily designed for the reception of non-baseband centred wireless and radar signals using the onboard digital down-conversion. As also discussed in Section 5.4.1, using sub-ADCs that can operate with low noise from the channel baseband DC to $\Delta f/2$ will be essential for achieving optimal performance when detecting broadband signals using a dual comb ADC.

5.5 Summary

This Chapter proposed a method for full bandwidth arbitrary signal detection using dual optical frequency combs through stabilisation of the relative phase between the two combs. The sensitivity of this method to errors in the phase stabilisation was shown to be straightforwardly mitigated by digital orthogonalisation procedures such as the Gram-Schmidt orthogonalisation procedure. The method was implemented experimentally by modifying the setup from Chapter 4 which proved its ability to distinguish sub-band conjugate sine wave test signals and detect arbitrary sub-band limited signals. Finally, sub-band limited QAM test signals were detected albeit with significantly reduced SNR, which could be attributed to SSBI caused by the limited CMRR of the balanced photodiodes and baseband centred noise from the sub-ADC used in the dual comb ADC prototype.

Chapter 6

Conclusions and Future Work

Designing high speed ADCs that can maintain the resolution required for high order modulation formats is extremely challenging but is essential for enabling the modern digital communications links that underpin our connected world. Photonic approaches to this challenge have been explored extensively, with most approaches seeking to utilise the extremely low jitter of mode locked lasers to implement photonic sampling in a time interleaving architecture. This thesis has explored a radically different approach to photonic ADCs based on using dual frequency combs to implement a frequency interleaving photonic front end and overcome the challenge of high speed, high frequency signal acquisition.

Chapter 2 discussed the state of the art in both electronic and photonic ADCs, beginning with defining the common metrics for evaluating ADCs and the impact of typical noise sources. The most common approach to electronic high speed ADCs is time interleaving, which although allowing for high sampling rates results in the same jitter degradation as a direct sampling architecture. Although frequency interleaving has been proposed and demonstrated to show lower jitter susceptibility in electronic ADCs, the challenges of local oscillator distribution and filter bank design has hindered their wide adoption. A variety of previous photonic ADC proposals and demonstrations were presented, followed by discussion of key photonic subsytems that are required for the experiments in this thesis.

Chapter 3 introduced the dual optical frequency comb ADC concept and set out the noise and distortion sources that define its performance. The relative phase noise (or jitter) of the two combs was shown to be a key factor to achieving high resolution at high bandwidths, using a novel phase noise analysis that is more broadly applicable to any dual comb based RF processing systems. This analysis was tested against numerical simulations and shown to be in good agreement.

Chapter 4 detailed the design of an experimental prototype designed to test the predictions of Chapter 3. The phase noise model developed was shown to be a good description of electro-optic based dual frequency comb systems, highlighting that both strong correlation between the two comb's jitter as well as low absolute phase noise is critical to achieving high resolution at high bandwidths. The dual comb prototype achieved 44 dB at 40 GHz under sine wave testing conditions, outperforming any conventional electronic ADC and is the best result for any known frequency interleaving approach. Compensation of the input modulator nonlinearity was shown to be possible using a simple arcsin based inversion of the modulator transfer function, which is essential to maintain high SINAD in shot noise limited scenarios.

Chapter 5 progressed the development of the dual comb ADC by proposing a novel technique that allowed recovery of arbitrary signals within the interleaved sub-bands by locking the relative phase between the two frequency combs. The impact of errors in this phase locking was explored and shown to be alleviated by common orthogonalisation techniques. Finally, the viability of the technique was verified experimentally by adapting the dual comb prototype and demonstrating the unambiguous detection of conjugate frequency components within a single sub-band, as well as the reception of a sub-band limited quadrature amplitude modulated data signal.

Overall, the dual comb ADC is a promising frequency interleaving photonic ADC technique that this thesis has shown can fundamentally outperform conventional high speed electronic ADCs. However, significant further work is needed to realise this performance when detecting the digitally modulated waveforms that are typically used in modern digital communications links. In particular, improving the performance of the sub-band receiver chain is critical to achieving the resolution promised by sine wave testing and theoretical analysis. Nevertheless, no fundamental obstacles appear to prohibit the dual comb ADC from achieving the crucial goal of high resolution digitisation of high speed arbitrary signals.

6.1 Future Work

6.1.1 Full sampling bandwidth demonstrations

All the work presented in this thesis was restricted to detecting and analysing the performance within a single sub-band, either through detection using a single balanced photodiode or through coherent detection of the full sub-band using the phase locking technique described in Chapter 5. This sub-sampling approach is typical when investigating photonic ADCs since it avoids the need to implement channel restitching DSP and allows for the investigation of fundamental performance without the need to contend with channel mismatch or other implementation errors. For example, to implement the full bandwidth of the dual comb prototype demonstrated in this thesis would require 25 balanced detectors, TIAs, and ADCs along with the associated DSP to reconstructed the detected signals.

The effect of these errors in a full bandwidth system is a clear avenue for investigation that was not considered in this thesis, whose focus was the fundamental performance. Literature investigating electronic ADC designs has shown that frequency interleaving designs are less susceptible to channel mismatch errors [43, 44, 41] and future work should investigate whether this benefit also applies to the dual comb approach. In particular, demonstrating this full bandwidth implementation in an application specific experiment such as an optical or wireless transmission system would illustrate the impact of the dual comb ADC's performance.

Furthermore, Chapter 5 showed that improvements to the sub-band receiver design over the prototype used in this thesis are needed for arbitrary signal detection. In particular, the ability of the analog front end and ADC to detect near DC frequency content should be improved, along with the CMRR of the balanced detector. The noise performance of the TIA could also be a focus to improve the thermal noise performance.

6.1.2 Integration and power consumption

Almost all photonic ADC demonstrations to date have been using discrete photonic components connected by optical fibers. Indeed, demonstrations of photonic ADCs on integrated platforms are scarce, and those which have been published have poor performance compared to their discrete component counterparts. A clear example of this is [48], where an integrated silicon design showed only 3.5 bits ENOB at 10 GHz compared to 7 bits at 41 GHz for the discrete component design. This disparity in achieved resolution is attributed by the authors to the poor efficiency of the silicon photodetectors and nonlinearity of the silicon modulators.

Given this, it is clear that demonstrating an integrated photonic ADC with performance approaching that promised by the published discrete component experiments would be a significant advance over the current state of the art. Indeed, it could be argued that the lack of such a result in the literature is why commercial ADC manufacturers have not, to the best of our knowledge, invested significant resources into investigating photonic approaches.

Besides SINAD, sampling rate, analog bandwidth and the associated effective jitter a key figure of merit (FOM) for electronic ADCs is the power dissipation P_{diss}, relative to the ENOB and sampling rate

$$\mathrm{FOM}_W = \frac{P_{diss}}{2^{\mathrm{ENOB}} f_s} \tag{6.1}$$

which is often called the Walden or ISSCC FOM [23]. Clearly, a discrete component photonic ADC cannot hope to compete with conventional electronic ADCs on this figure of merit. Efficiency goes hand in hand with integration and makes the demonstration of a high performance integrated photonic ADC essential to address this current weakness compared to their electronic counterpart.

A number of platforms could be explored for integration. For example, thin film lithium niobate is an ideal platform for the dual comb system with ultra low loss waveguides [185, 186, 187, 188], compact and high performance modulators [189, 190], broadband frequency comb generation [167, 168] and tunable filters [191]. A chip that integrates the entire optical structure of the dual comb ADC, including receiver photodiodes, along with two chips that separate the dual comb and sub-band receiver array for debugging in conjunction with our discrete component dual comb test could be produced. Co-integration with the seed laser on, for example, InP can allow for a fully integrated dual comb solution [182].

Besides an experimental demonstration of an integrated dual comb ADC, theoretical and simulation work could be undertaken to estimate its power consumption. A direct comparison on these grounds compared to conventional electronic ADCs may be critical in elucidating the role of dual comb ADCs in the future of high speed signal digitisation compared with the results presented in this thesis. Such an analysis could even be extended to photonic ADCs in general or across a variety of integrated or co-integrated photonic-electronic platforms, based on current and future performance trends. Even if a power consumption analysis is not favourable for the dual comb or photonic ADCs in general, their performance advantage over electronic ADCs may give them an edge in FOM_W or test and measuremnt scenarios where power consumption is not a consideration.

6.1.3 Phase noise compensation

This thesis described how in a dual comb system, both correlation in the phase noise between the two frequency combs and minimising the phase noise of each comb is essential to minimising the impact of phase noise in a dual comb system. Regardless, Chapters 3 and 4 showed how the phase noise of the combs can still significantly impact performance of the dual comb system in high bandwidth scenarios.

One approach to mitigate this might be to exploit the correlation of phase noise between comb lines, as has been shown in single frequency electro optic comb systems [162]. For example, in a cascaded phase-intensity modulator based EO comb the complementary outputs of the intensity modulators, assuming it is placed after the phase modulator, could be used to determine the instantaneous phase error in the dual comb system by measuring the beat note between two comb lines on a low speed ADC. This instantaneous phase error could then be applied as a correction to the measured data and drastically reduce the impact of phase noise on the dual comb system.

The maximum phase noise bandwidth that could be suppressed by such a system would be dependent on a number of factors. Firstly, the jitter or other white noise sources added by the sub-band receiver and error measurement circuit must be minimised in order to obtain an accurate measurement of the instantaneous phase error. In addition, the optical path lengths between the phase error detection path and signal detection channels must be tightly length matched so that the error detection is measuring the correct sampling point. In standard silica fibre with a refractive index of 1.44, achieving a correlation up to 1 GHz only requires length matching on the order of 20 cm, which is trivial to achieve using discrete components let alone on an integrated platform. Combined with the filtering of wideband phase noise demonstrated in this thesis using narrowband optical or RF filters, this could achieve strong suppression of the dual comb phase noise and subsequent improvement in performance at high bandwidths. The use of optical filters as opposed to the RF cavity filters used in this thesis may offer better prospects for integration and concurrently suppress any ASE noise added from optical amplifiers.

Bibliography

[1] C. E. Shannon, “A mathematical theory of communication,” *The Bell system technical journal*, vol. 27, no. 3, pp. 379–423, 1948.

[2] C. E. Shannon, “Communication in the presence of noise,” *Proceedings of the IRE*, vol. 37, no. 1, pp. 10–21, 1949.

[3] P. J. Winzer, D. T. Neilson, and A. R. Chraplyvy, “Fiber-optic transmission and networking: the previous 20 and the next 20 years,” *Optics express*, vol. 26, no. 18, pp. 24190–24239, 2018.

[4] R. H. Walden, “Analog-to-digital conversion in the early twenty-first century,” *Wiley Encyclopedia of Computer Science and Engineering*, pp. 1–14, 2007.

[5] T. Drenski and J. C. Rasmussen, “ADC and DAC Technology trends and steps to overcome current limitations,” in *2018 OFC*, p. M2C.1, 2018.

[6] G. C. Valley, “Photonic analog-to-digital converters,” *Optics express*, vol. 15, no. 5, pp. 1955–1982, 2007.

[7] V. Torres-Company and A. M. Weiner, “Optical frequency comb technology for ultra-broadband radio-frequency photonics,” *Laser and Photonics Reviews*, vol. 8, no. 3, pp. 368–393, 2014.

[8] C. Deakin and Z. Liu, “Dual frequency comb assisted analog-to-digital conversion,” *Optics Letters*, vol. 45, no. 1, pp. 173–176, 2020.

[9] C. Deakin and Z. Liu, “Noise and distortion analysis of dual frequency comb photonic RF channelizers,” *Optics Express*, vol. 28, no. 26, pp. 39750–39769, 2020.

[10] C. Deakin and Z. Liu, “Performance of dual frequency comb channelizers for RF signal processing,” in *Optical Fiber Communication Conference*, pp. Tu5F–4, Optical Society of America, 2021.

[11] C. Deakin, Z. Zhou, and Z. Liu, “Phase noise of electro-optic dual frequency combs,” *Optics Letters*, vol. 46, no. 6, pp. 1345–1348, 2021.

[12] C. Deakin and Z. Liu, “Frequency interleaving dual comb photonic ADC with 7 bits ENOB up to 40 GHz,” in *CLEO: Science and Innovations*, p. STh5M.1, Optical Society of America, 2022.

[13] Z. Liu and C. Deakin, “Signal processor apparatus,” Sept. 2021. App. No. WO2021170996A1.

[14] W. R. Bennett, “Spectra of quantized signals,” *The Bell System Technical Journal*, vol. 27, no. 3, pp. 446–472, 1948.

[15] T. Ulversoy, “Software defined radio: Challenges and opportunities,” *IEEE Communications Surveys and Tutorials*, vol. 12, no. 4, pp. 531–550, 2010.

[16] B. Brannon and A. Barlow, “Aperture uncertainty and ADC system performance,” *Applications Note AN-501. Analog Devices, Inc.(September)*, 2000.

[17] M. Shinagawa, Y. Akazawa, and T. Wakimoto, “Jitter analysis of high-speed sampling systems,” *IEEE Journal of Solid-State Circuits*, vol. 25, no. 1, pp. 220–224, 1990.

[18] H. Kobayashi, M. Morimura, K. Kobayashi, and Y. Onaya, “Aperture jitter effects in wideband ADC systems,” in *SICE’99. Proceedings of the 38th SICE Annual Conference. International Session Papers (IEEE Cat. No. 99TH8456)*, pp. 1089–1094, IEEE, 1999.

[19] E. Rubiola, *Phase Noise and Frequency Stability in Oscillators*. Cambridge: Cambridge University Press, 2008.

[20] B. Brannon, “Sampled systems and the effects of clock phase noise and jitter,” *Analog Devices App. Note AN-756*, pp. 1–11, 2004.

[21] A. Viterbi, “Nonlinear estimation of PSK-modulated carrier phase with application to burst digital transmission,” *IEEE Transactions on Information theory*, vol. 29, no. 4, pp. 543–551, 1983.

[22] T. Pfau, S. Hoffmann, and R. Noé, “Hardware-efficient coherent digital receiver concept with feedforward carrier recovery for M-QAM constellations,” *Journal of Lightwave Technology*, vol. 27, no. 8, pp. 989–999, 2009.

[23] R. Walden, “Analog-to-digital converter survey and analysis,” *IEEE Journal on Selected Areas in Communications*, vol. 17, pp. 539–550, Apr. 1999.

[24] B. Murmann, "ADC performance survey 1997-2021,." `http://web.stanford.edu/~murmann/adcsurvey.html`. Accessed: 2022-07-18. Rev. 20210628.

[25] P. S. Chakraborty, A. S. Cardoso, B. R. Wier, A. P. Omprakash, J. D. Cressler, M. Kaynak, and B. Tillack, "A 0.8 THz f_{MAX} SiGe HBT Operating at 4.3 K," *IEEE Electron Device Letters*, vol. 35, no. 2, pp. 151–153, 2014.

[26] S. A. Zahrai and M. Onabajo, "Review of analog-to-digital conversion characteristics and design considerations for the creation of power-efficient hybrid data converters," *Journal of Low Power Electronics and Applications*, vol. 8, no. 2, p. 12, 2018.

[27] R. Nguyen, A. Castrillon, A. Fan, A. Mellati, B. T. Reyes, C. Abidin, E. Olsen, F. Ahmad, G. Hatcher, J. Chana, *et al.*, "A highly reconfigurable 40-97 GS/s DAC and ADC with 40 GHz AFE bandwidth and sub-35 fJ/conv-step for 400Gb/s coherent optical applications in 7nm FinFET," in *2021 IEEE International Solid-State Circuits Conference (ISSCC)*, vol. 64, pp. 136–138, IEEE, 2021.

[28] Y. Duan and E. Alon, "A 6b 46 GS/s ADC with >23GHz BW and sparkle-code error correction," in *2015 Symposium on VLSI Circuits (VLSI Circuits)*, pp. C162–C163, IEEE, 2015.

[29] L. Kull, T. Toifl, M. Schmatz, P. A. Francese, C. Menolfi, M. Braendli, M. Kossel, T. Morf, T. M. Andersen, and Y. Leblebici, "A 90 GS/s 8b 667 mW 64× interleaved SAR ADC in 32 nm digital SOI CMOS," in *2014 IEEE International Solid-State Circuits Conference Digest of Technical Papers (ISSCC)*, pp. 378–379, IEEE, 2014.

[30] B. Razavi, "Design considerations for interleaved ADCs," *IEEE Journal of Solid-State Circuits*, vol. 48, no. 8, pp. 1806–1817, 2013.

[31] W. C. Black and D. A. Hodges, "Time interleaved converter arrays," *IEEE Journal of Solid-state circuits*, vol. 15, no. 6, pp. 1022–1029, 1980.

[32] Y.-C. Jenq, "Digital spectra of nonuniformly sampled signals: Fundamentals and high-speed waveform digitizers," *IEEE Transactions on Instrumentation and Measurement*, vol. 37, no. 2, pp. 245–251, 1988.

[33] N. Kurosawa, H. Kobayashi, K. Maruyama, H. Sugawara, and K. Kobayashi, "Explicit analysis of channel mismatch effects in time-interleaved ADC systems," *IEEE Transactions on Circuits and Systems I: Fundamental Theory and Applications*, vol. 48, no. 3, pp. 261–271, 2001.

[34] S. R. Velazquez, T. Q. Nguyen, S. R. Broadstone, and J. K. Roberge, "A hybrid filter bank approach to analog-to-digital conversion," in *Proceedings of IEEE-SP International Symposium on Time-Frequency and Time-Scale Analysis*, pp. 116–119, IEEE, 1994.

[35] P. J. Pupalaikis and D. C. Graef, "High bandwidth real-time oscilloscope," June 6 2006. US Patent 7,058,548.

[36] K. Lee and W. Namgoong, "A 0.25 µm CMOS 3b 12.5 GS/s frequency channelized receiver for serial-links," in *ISSCC. 2005 IEEE International Digest of Technical Papers. Solid-State Circuits Conference, 2005.*, pp. 336–337, IEEE, 2005.

[37] S. R. Velazquez, *Hybrid filter banks for analog/digital conversion*. PhD thesis, Massachusetts Institute of Technology, 1997.

[38] L. Guo, S. Tian, Z. Wang, K. Yang, and L. Qiu, "Analysis of channel mismatch errors in frequency-interleaved ADC system," *Circuits, Systems, and Signal Processing*, vol. 33, no. 12, pp. 3697–3712, 2014.

[39] U. Onunkwo, Y. Li, and A. Swami, "Effect of timing jitter on OFDM-based UWB systems," *IEEE journal on Selected areas in Communications*, vol. 24, no. 4, pp. 787–793, 2006.

[40] S. J. Mazlouman, S. Sheikhaei, and S. Mirabbasi, "4-and 6-GS/s 4-bit frequency-translating hybrid ADCs in 90-nm CMOS," *Analog Integrated Circuits and Signal Processing*, vol. 68, no. 3, pp. 329–340, 2011.

[41] S. Hoyos, S. Pentakota, Z. Yu, E. S. A. Ghany, X. Chen, R. Saad, S. Palermo, and J. Silva-Martinez, "Clock-jitter-tolerant wideband receivers: An optimized multichannel filter-bank approach," *IEEE Transactions on Circuits and Systems I: Regular Papers*, vol. 58, no. 2, pp. 253–263, 2010.

[42] S. R. Velazquez, T. Q. Nguyen, and S. R. Broadstone, "Design of hybrid filter banks for analog/digital conversion," *IEEE transactions on signal processing*, vol. 46, no. 4, pp. 956–967, 1998.

[43] S. W. Callender, *Wideband signal acquisition via frequency-interleaved sampling*. PhD thesis, UC Berkeley, 2015.

[44] J. Song, S. Tian, and Y.-H. Hu, "Analysis and correction of combined channel mismatch effects in frequency-interleaved ADCs," *IEEE Transactions on Circuits and Systems I: Regular Papers*, vol. 66, no. 2, pp. 655–668, 2018.

[45] J. A. Weldon, R. S. Narayanaswami, J. C. Rudell, L. Lin, M. Otsuka, S. Dedieu, L. Tee, K.-C. Tsai, C.-W. Lee, and P. R. Gray, “A 1.75-GHz highly integrated narrow-band CMOS transmitter with harmonic-rejection mixers,” *IEEE Journal of Solid-State Circuits*, vol. 36, no. 12, pp. 2003–2015, 2001.

[46] A. A. Rafi, A. Piovaccari, P. Vancorenland, and T. Tuttle, “A harmonic rejection mixer robust to RF device mismatches,” in *2011 IEEE International Solid-State Circuits Conference*, pp. 66–68, IEEE, 2011.

[47] J. Song, S. Tian, Y.-H. Hu, and P. Ye, “Digital iterative harmonic rejection and image cancellation for LPF-less frequency-interleaved analog-to-digital converters,” *IEEE Transactions on Circuits and Systems II: Express Briefs*, vol. 66, no. 12, pp. 2072–2076, 2019.

[48] A. Khilo *et al.*, “Photonic ADC: overcoming the bottleneck of electronic jitter,” *Optics Express*, vol. 20, pp. 4454–4469, Feb. 2012.

[49] C. K. Sun, C.-C. Wu, C. T. Chang, P. K. Yu, and W. H. McKnight, “A bridge type optoelectronic sample and hold circuit,” *Journal of lightwave technology*, vol. 9, no. 3, pp. 341–346, 1991.

[50] A. Bhushan, F. Coppinger, and B. Jalali, “Time-stretched analogue-to-digital conversion,” *Electronics Letters*, vol. 34, no. 9, pp. 839–841, 1998.

[51] A. Bhushan, F. Coppinger, B. Jalali, S. Wang, and H. Fetterman, “150 Gsample/s wavelength division sampler with time-stretched output,” *Electronics Letters*, vol. 34, no. 5, pp. 474–475, 1998.

[52] J. Chou, O. Boyraz, D. Solli, and B. Jalali, “Femtosecond real-time single-shot digitizer,” *Applied Physics Letters*, vol. 91, no. 16, p. 161105, 2007.

[53] X. Xie, Y. Dai, K. Xu, J. Niu, R. Wang, L. Yan, and J. Lin, “Broadband photonic RF channelization based on coherent optical frequency combs and I/Q demodulators,” *IEEE Photonics Journal*, vol. 4, no. 4, pp. 1196–1202, 2012.

[54] X. Xu, J. Wu, T. G. Nguyen, S. T. Chu, B. E. Little, R. Morandotti, A. Mitchell, and D. J. Moss, “Broadband RF channelizer based on an integrated optical frequency Kerr comb source,” *Journal of Lightwave Technology*, vol. 36, no. 19, pp. 4519–4526, 2018.

[55] N. K. Fontaine, R. P. Scott, L. Zhou, F. M. Soares, J. Heritage, and S. Yoo, “Real-time full-field arbitrary optical waveform measurement,” *Nature Photonics*, vol. 4, no. 4, pp. 248–254, 2010.

[56] D. Fang *et al.*, “320 GHz analog-to-digital converter exploiting Kerr soliton combs and photonic-electronic spectral stitching,” in *2021 European Conference on Optical Communication (ECOC)*, pp. Th3C1–PD2.2, IEEE, 2021.

[57] H. Hu and S. Radic, “Hybrid OFDM receiver assisted by a variable frequency comb,” *Optics Express*, vol. 28, no. 4, pp. 5658–5668, 2020.

[58] A. Lukashchuk, J. Riemensberger, J. Liu, P. Marin-Palomo, C. Koos, R. Bouchand, and T. J. Kippenberg, “Photonic-assisted analog-to-digital conversion using integrated soliton microcombs,” *2019 European Conference on Communications*, p. 4, 2019.

[59] J. Yang, R. Li, Y. Dai, J. Dong, and W. Li, “Wide-band RF receiver based on dual-ofc-based photonic channelization and spectrum stitching technique,” *Optics Express*, vol. 27, no. 23, pp. 33194–33204, 2019.

[60] H. Zmuda, “Analog-to-digital conversion using high-speed photonic processing,” in *Multifrequency Electronic/Photonic Devices and Systems for Dual-Use Applications*, vol. 4490, pp. 84–95, International Society for Optics and Photonics, 2001.

[61] M. Johansson, B. Löfving, S. Hård, L. Thylén, M. Mokhtari, U. Westergren, and C. Pala, “Study of an ultrafast analog-to-digital conversion scheme based on diffractive optics,” *Applied Optics*, vol. 39, no. 17, pp. 2881–2887, 2000.

[62] H. F. Taylor, “An electrooptic analog-to-digital converter,” *Proceedings of the IEEE*, vol. 63, no. 10, pp. 1524–1525, 1975.

[63] K. Takizawa and M. Okada, “Analog-to-digital converter: a new type using an electrooptic light modulator,” *Applied optics*, vol. 18, no. 18, pp. 3148–3151, 1979.

[64] R. Becker and F. Leonberger, “2-bit 1 Gsample/s electrooptic guided-wave analog-to-digital converter,” *IEEE Journal of Quantum Electronics*, vol. 18, no. 10, pp. 1411–1413, 1982.

[65] R. Dokhikyan, E. M. Zolotov, S. Karinskiĭ, V. Maksimov, V. Popkov, A. M. Prokhorov, I. Sisakyan, and E. Shcherbakov, “Prototype of an integrated-optics four-digit analog-digital converter,” *Soviet Journal of Quantum Electronics*, vol. 12, no. 6, p. 806, 1982.

[66] R. Walker, I. Bennion, and A. Carter, “Novel GaAs/AlGaAs guided-wave analogue/digital convertor,” *Electronics Letters*, vol. 25, no. 21, pp. 1443–1444, 1989.

[67] B. Jalali and Y. Xie, “Optical folding-flash analog-to-digital converter with analog encoding,” *Optics letters*, vol. 20, no. 18, pp. 1901–1903, 1995.

[68] M. Currie, T. R. Clark, and P. J. Matthews, “Photonic analog-to-digital conversion by distributed phase modulation,” *IEEE Photonics Technology Letters*, vol. 12, no. 12, pp. 1689–1691, 2000.

[69] K. Ikeda, J. M. Abdul, S. Namiki, and K.-i. Kitayama, “Optical quantizing and coding for ultrafast A/D conversion using nonlinear fiber-optic switches based on Sagnac interferometer,” *Optics express*, vol. 13, no. 11, pp. 4296–4302, 2005.

[70] L. M. Loh and J. L. LoCicero, “Subnanosecond sampling all-optical analog-to-digital converter using s-seeds,” *Optical Engineering*, vol. 35, 1996.

[71] M. J. Hayduk, R. J. Bussjager, and M. A. Getbehead, “Photonic analog-to-digital conversion techniques using semiconductor saturable absorbers,” in *Enabling Photonic Technologies for Aerospace Applications II*, vol. 4042, pp. 54–60, International Society for Optics and Photonics, 2000.

[72] J.-M. Jeong and M. Marhic, “All-optical analog-to-digital and digital-to-analog conversion implemented by a nonlinear fiber interferometer,” *Optics communications*, vol. 91, no. 1-2, pp. 115–122, 1992.

[73] P. Ho, Q. Wang, J. Chen, Q. Liu, and R. Alfano, “Ultrafast optical pulse digitization with unary spectrally encoded cross-phase modulation,” *Applied optics*, vol. 36, no. 15, pp. 3425–3429, 1997.

[74] S.-i. Oda, A. Maruta, and K.-i. Kitayama, “All-optical quantization scheme based on fiber nonlinearity,” *IEEE Photonics Technology Letters*, vol. 16, no. 2, pp. 587–589, 2004.

[75] J. Chou, J. A. Conway, G. A. Sefler, G. C. Valley, and B. Jalali, “Photonic bandwidth compression front end for digital oscilloscopes,” *Journal of Lightwave Technology*, vol. 27, no. 22, pp. 5073–5077, 2009.

[76] R. Williamson, R. Younger, P. Juodawlkis, J. Hargreaves, and J. Twichell, “Precision calibration of an optically sampled analog-to-digital converter,” in *2003 Digest of LEOS Summer Topical Meeting (Cat. No. 03TH8701)*, pp. MC4–2, IEEE, 2003.

[77] G. A. Sefler, J. Chou, J. A. Conway, and G. C. Valley, “Distortion correction in a high-resolution time-stretch ADC scalable to continuous time,” *Journal of Lightwave Technology*, vol. 28, no. 10, pp. 1468–1476, 2010.

[78] S. Gupta and B. Jalali, “Time-warp correction and calibration in photonic time-stretch analog-to-digital converter,” *Optics letters*, vol. 33, no. 22, pp. 2674–2676, 2008.

[79] F. Laghezza, F. Scotti, P. Ghelfi, A. Bogoni, and S. Pinna, “Jitter-limited photonic analog-to-digital converter with 7 effective bits for wideband radar applications,” in *2013 IEEE Radar Conference (RadarCon13)*, pp. 1–5, IEEE, 2013.

[80] S. Xu, X. Zou, B. Ma, J. Chen, L. Yu, and W. Zou, “Deep-learning-powered photonic analog-to-digital conversion,” *Light: Science and Applications*, vol. 8, no. 1, pp. 1–11, 2019.

[81] D. J. Esman, A. O. Wiberg, N. Alic, and S. Radic, “Highly linear broadband photonic-assisted Q-band ADC,” *Journal of Lightwave Technology*, vol. 33, no. 11, pp. 2256–2262, 2015.

[82] J. Kim, M. J. Park, M. H. Perrott, and F. X. Kärtner, “Photonic subsampling analog-to-digital conversion of microwave signals at 40-GHz with higher than 7-ENOB resolution,” *Optics Express*, vol. 16, no. 21, pp. 16509–16515, 2008.

[83] D. J. Esman, A. O. Wiberg, M.-H. Yang, L. Liu, B. P.-P. Kuo, N. Alic, and S. Radic, “Photonic parametric sampled analog-to-digital conversion at 100 GHz and 6 ENOBs,” in *2014 The European Conference on Optical Communication (ECOC)*, pp. 1–3, IEEE, 2014.

[84] H. R. Telle, G. Steinmeyer, A. Dunlop, J. Stenger, D. Sutter, and U. Keller, “Carrier-envelope offset phase control: A novel concept for absolute optical frequency measurement and ultrashort pulse generation,” *Applied Physics B*, vol. 69, no. 4, pp. 327–332, 1999.

[85] I. Coddington, N. Newbury, and W. Swann, “Dual-comb spectroscopy,” *Optica*, vol. 3, p. 414, Apr. 2016.

[86] T. Udem, R. Holzwarth, and T. W. Hänsch, “Optical frequency metrology,” *Nature*, vol. 416, no. 6877, p. 233, 2002.

[87] N. R. Newbury, “Searching for applications with a fine-tooth comb,” *Nature photonics*, vol. 5, no. 4, p. 186, 2011.

[88] M. Mazur, A. Lorences-Riesgo, J. Schröder, P. A. Andrekson, and M. Karlsson, “10 Tb/s PM-64QAM self-homodyne comb-based superchannel transmission with 4% shared pilot tone overhead,” *Journal of Lightwave Technology*, vol. 36, no. 16, pp. 3176–3184, 2018.

[89] D. Kuizenga and A. Siegman, “FM and AM mode locking of the homogeneous laser - Part I: Theory,” *IEEE Journal of Quantum Electronics*, vol. 6, no. 11, pp. 694–708, 1970.

[90] J. Kim and Y. Song, “Ultralow-noise mode-locked fiber lasers and frequency combs: principles, status, and applications,” *Advances in Optics and Photonics*, vol. 8, no. 3, pp. 465–540, 2016.

[91] A. C. S Jr, J. C. Boggio, A. Rieznik, H. Hernandez-Figueroa, H. Fragnito, and J. Knight, “Highly efficient generation of broadband cascaded four-wave mixing products,” *Optics Express*, vol. 16, no. 4, pp. 2816–2828, 2008.

[92] J. C. Boggio, S. Moro, N. Alic, M. Karlsson, J. Bland-Hawthorn, and S. Radic, “Nearly octave-spanning cascaded four-wave-mixing generation in low dispersion highly nonlinear fiber,” in *2009 35th European Conference on Optical Communication*, pp. 1–2, IEEE, 2009.

[93] Z. Tong, A. O. Wiberg, E. Myslivets, B. P. Kuo, N. Alic, and S. Radic, “Spectral linewidth preservation in parametric frequency combs seeded by dual pumps,” *Optics Express*, vol. 20, no. 16, pp. 17610–17619, 2012.

[94] H. Hu, F. Da Ros, M. Pu, F. Ye, K. Ingerslev, E. P. da Silva, M. Nooruzzaman, Y. Amma, Y. Sasaki, T. Mizuno, *et al.*, “Single-source chip-based frequency comb enabling extreme parallel data transmission,” *Nature Photonics*, vol. 12, no. 8, p. 469, 2018.

[95] B. Kuyken, M. Billet, F. Leo, K. Yvind, and M. Pu, “Octave-spanning coherent supercontinuum generation in an AlGaAs-on-insulator waveguide,” *Opt. Lett.*, vol. 45, pp. 603–606, Feb 2020.

[96] M. D. Pelusi, V. G. Ta’eed, L. Fu, E. Magi, M. R. E. Lamont, S. Madden, D.-Y. Choi, D. A. P. Bulla, B. Luther-Davies, and B. J. Eggleton, “Applications of highly-nonlinear chalcogenide glass devices tailored for high-speed all-optical signal processing,” *IEEE Journal of Selected Topics in Quantum Electronics*, vol. 14, no. 3, pp. 529–539, 2008.

[97] R. Sohanpal, H. Ren, L. Shen, C. Deakin, A. M. Heidt, T. W. Hawkins, J. Ballato, U. J. Gibson, A. C. Peacock, and Z. Liu, “All-fibre heterogeneously-integrated frequency comb generation using silicon core fibre,” *Nature Communications*, vol. 13, no. 1, p. 3992, 2022.

[98] G. Son, S. Han, J. Park, K. Kwon, and K. Yu, “High-efficiency broadband light coupling between optical fibers and photonic integrated circuits:,” *Nanophotonics*, vol. 7, no. 12, pp. 1845–1864, 2018.

[99] P. DelHaye, A. Schliesser, O. Arcizet, T. Wilken, R. Holzwarth, and T. J. Kippenberg, "Optical frequency comb generation from a monolithic microresonator," *Nature*, vol. 450, no. 7173, pp. 1214–1217, 2007.

[100] T. J. Kippenberg, R. Holzwarth, and S. A. Diddams, "Microresonator-based optical frequency combs," *Science*, vol. 332, no. 6029, pp. 555–559, 2011.

[101] P. Del'Haye, T. Herr, E. Gavartin, R. Holzwarth, and T. J. Kippenberg, "Octave Spanning Frequency Comb on a Chip," *Physical Review Letters*, vol. 107, p. 063901, Aug. 2011. arXiv: 0912.4890.

[102] P. DelHaye, O. Arcizet, A. Schliesser, R. Holzwarth, and T. J. Kippenberg, "Full stabilization of a microresonator-based optical frequency comb," *Physical Review Letters*, vol. 101, no. 5, p. 053903, 2008.

[103] V. Torres-Company, J. Lancis, and P. Andrés, "Lossless equalization of frequency combs," *Opt. Lett.*, vol. 33, pp. 1822–1824, Aug 2008.

[104] B. H. Kolner and M. Nazarathy, "Temporal imaging with a time lens," *Optics letters*, vol. 14, no. 12, pp. 630–632, 1989.

[105] IEEE, "IEEE standard definitions of physical quantities for fundamental frequency and time metrology—random instabilities," *IEEE Std Std 1139-2008*, pp. c1–35, 2009.

[106] F. N. Hooge, "1/f noise sources," *IEEE Transactions on electron devices*, vol. 41, no. 11, pp. 1926–1935, 1994.

[107] D. Leeson, "A simple model of feedback oscillator noise spectrum," *proc. IEEE*, vol. 54, no. 2, pp. 329–330, 1966.

[108] E. Rubiola and R. Brendel, "A generalization of the Leeson effect," *arXiv preprint arXiv:1004.5539*, 2010.

[109] C. Henry, "Theory of the linewidth of semiconductor lasers," *IEEE Journal of Quantum Electronics*, vol. 18, no. 2, pp. 259–264, 1982.

[110] K. Kikuchi, "Effect of 1/f-type FM noise on semiconductor-laser linewidth residual in high-power limit," *IEEE Journal of Quantum Electronics*, vol. 25, no. 4, pp. 684–688, 1989.

[111] G. Tenchio, "Low-frequency intensity fluctuations of c.w. d.h. GaAlAs-diode lasers," *Electronics Letters*, vol. 12, no. 21, pp. 562–563, 1976.

[112] D. Welford and A. Mooradian, “Observation of linewidth broadening in (GaAl)As diode lasers due to electron number fluctuations,” *Applied Physics Letters*, vol. 40, no. 7, pp. 560–562, 1982.

[113] M. O’Mahony and I. Henning, “Semiconductor laser linewidth broadening due to 1/f carrier noise,” *Electronics Letters*, vol. 19, no. 23, pp. 1000–1001, 1983.

[114] G. Stéphan, T. Tam, S. Blin, P. Besnard, and M. Têtu, “Laser line shape and spectral density of frequency noise,” *Physical Review A*, vol. 71, no. 4, p. 043809, 2005.

[115] L. B. Mercer, “1/f frequency noise effects on self-heterodyne linewidth measurements,” *Journal of Lightwave Technology*, vol. 9, no. 4, pp. 485–493, 1991.

[116] E. Rubiola, “The measurement of am noise of oscillators,” in *2006 IEEE International Frequency Control Symposium and Exposition*, pp. 750–758, IEEE, 2006.

[117] S. Chang, A. Mann, A. Luiten, and D. Blair, “Measurements of radiation pressure effect in cryogenic sapphire dielectric resonators,” *Physical review letters*, vol. 79, no. 11, p. 2141, 1997.

[118] N. Gufflet, R. Bourquin, and J.-J. Boy, “Isochronism defect for various doubly rotated cut quartz resonators,” *IEEE transactions on ultrasonics, ferroelectrics, and frequency control*, vol. 49, no. 4, pp. 514–518, 2002.

[119] G. P. Agrawal and N. K. Dutta, *Long-wavelength semiconductor lasers*, vol. 1. Springer, 1986.

[120] C. Spiegelberg, J. Geng, Y. Hu, Y. Kaneda, S. Jiang, and N. Peyghambarian, “Low-noise narrow-linewidth fiber laser at 1550 nm,” *Journal of lightwave technology*, vol. 22, no. 1, pp. 57–62, 2004.

[121] E. Desurvire, *Erbium-Doped Fiber Amplifiers: Principles and Applications*. Wiley, New York, 1994.

[122] H. Haus, “The noise figure of optical amplifiers,” *IEEE Photonics Technology Letters*, vol. 10, no. 11, pp. 1602–1604, 1998.

[123] E. Desurvire, “Comments on "the noise figure of optical amplifiers",” *IEEE Photonics Technology Letters*, vol. 11, no. 5, pp. 620–621, 1999.

[124] D. M. Baney, P. Gallion, and R. S. Tucker, “Theory and measurement techniques for the noise figure of optical amplifiers,” *Optical fiber technology*, vol. 6, no. 2, pp. 122–154, 2000.

[125] B. Mukherjee, I. Tomkos, M. Tornatore, P. Winzer, and Y. Zhao, *Springer Handbook of Optical Networks*. Springer, 2020.

[126] B. Liu, A. Shakouri, and J. E. Bowers, “Wide tunable double ring resonator coupled lasers,” *IEEE Photonics Technology Letters*, vol. 14, no. 5, pp. 600–602, 2002.

[127] T. Claes, W. Bogaerts, and P. Bienstman, “Experimental characterization of a silicon photonic biosensor consisting of two cascaded ring resonators based on the Vernier-effect and introduction of a curve fitting method for an improved detection limit,” *Optics express*, vol. 18, no. 22, pp. 22747–22761, 2010.

[128] L. Guo, S. Tian, Z. Wang, K. Yang, and L. Qiu, “Analysis of Channel Mismatch Errors in Frequency-Interleaved ADC System,” *Circuits, Systems, and Signal Processing*, vol. 33, pp. 3697–3712, Dec. 2014.

[129] V. Ataie, D. Esman, B. P.-P. Kuo, N. Alic, and S. Radic, “Subnoise detection of a fast random event,” *Science*, vol. 350, pp. 1343–1346, Dec. 2015.

[130] D. J. Esman, V. Ataie, B. P. Kuo, E. Temprana, N. Alic, and S. Radic, “Detection of Fast Transient Events in a Noisy Background,” *Journal of Lightwave Technology*, vol. 34, pp. 5669–5674, Dec. 2016.

[131] H. Hu, V. Ataie, E. Myslivets, and S. Radic, “Optical comb assisted OFDM RF receiver,” *Journal of Lightwave Technology*, vol. 37, no. 4, pp. 1280–1287, 2019.

[132] M. S. Alshaykh, D. E. Leaird, J. D. McKinney, and A. M. Weiner, “Rapid wideband RF subsampling and disambiguation using dual combs,” in *CLEO: Science and Innovations*, p. SF2N.8, Optical Society of America, 2019.

[133] Z. Pi and F. Khan, “An introduction to millimeter-wave mobile broadband systems,” *IEEE communications magazine*, vol. 49, no. 6, pp. 101–107, 2011.

[134] J. Wenger, “Automotive mm-wave radar: Status and trends in system design and technology,” *IEE Colloquium on Automotive Radar and Navigation Techniques*, 1998.

[135] Y. Okawachi, K. Saha, J. S. Levy, Y. H. Wen, M. Lipson, and A. L. Gaeta, “Octave-spanning frequency comb generation in a silicon nitride chip,” *Optics letters*, vol. 36, no. 17, pp. 3398–3400, 2011.

[136] E. Myslivets, B. P. Kuo, N. Alic, and S. Radic, “Generation of wideband frequency combs by continuous-wave seeding of multistage mixers with synthesized dispersion,” *Optics express*, vol. 20, no. 3, pp. 3331–3344, 2012.

[137] E. Rubiola, *Phase noise and frequency stability in oscillators*. Cambridge University Press, 2009.

[138] C. W. Nelson, A. Hati, and D. A. Howe, “Relative intensity noise suppression for RF photonic links,” *IEEE Photonics Technology Letters*, vol. 20, no. 18, pp. 1542–1544, 2008.

[139] D. Kim, S. Zhang, D. Kwon, R. Liao, Y. Cui, Z. Zhang, Y. Song, and J. Kim, “Intensity noise suppression in mode-locked fiber lasers by double optical bandpass filtering,” *Optics Letters*, vol. 42, no. 20, pp. 4095–4098, 2017.

[140] X. Xie, J. Khurgin, J. Kang, and F.-S. Chow, “Linearized Mach-Zehnder intensity modulator,” *IEEE Photonics Technology Letters*, vol. 15, no. 4, pp. 531–533, 2003.

[141] H. Yamazaki, H. Takahashi, T. Goh, Y. Hashizume, T. Yamada, S. Mino, H. Kawakami, and Y. Miyamoto, “Optical modulator with a near-linear field response,” *Journal of Lightwave Technology*, vol. 34, no. 16, pp. 3796–3802, 2016.

[142] A. Khilo, C. M. Sorace, and F. X. Kärtner, “Broadband linearized silicon modulator,” *Optics express*, vol. 19, no. 5, pp. 4485–4500, 2011.

[143] T. Clark, M. Currie, and P. Matthews, “Digitally linearized wide-band photonic link,” *Journal of Lightwave Technology*, vol. 19, no. 2, pp. 172–179, 2001.

[144] Y. Cui, Y. Dai, F. Yin, Q. Lv, J. Li, K. Xu, and J. Lin, “Enhanced spurious-free dynamic range in intensity-modulated analog photonic link using digital postprocessing,” *IEEE Photonics Journal*, vol. 6, no. 2, pp. 1–8, 2014.

[145] W. Jiang, Q. Tan, W. Qin, D. Liang, X. Li, H. Ma, and Z. Zhu, “A linearization analog photonic link with high third-order intermodulation distortion suppression based on dual-parallel Mach-Zehnder modulator,” *IEEE Photonics Journal*, vol. 7, no. 3, pp. 1–8, 2015.

[146] A. Ishizawa, T. Nishikawa, A. Mizutori, H. Takara, A. Takada, T. Sogawa, and M. Koga, “Phase-noise characteristics of a 25-GHz-spaced optical frequency comb based on a phase-and intensity-modulated laser,” *Optics express*, vol. 21, no. 24, pp. 29186–29194, 2013.

[147] K. Nishimoto, K. Minoshima, T. Yasui, and N. Kuse, “Investigation of the phase noise of a microresonator soliton comb,” *Optics Express*, vol. 28, no. 13, pp. 19295–19303, 2020.

[148] D. Rönnow, S. Amin, M. Alizadeh, and E. Zenteno, “Phase noise coherence of two continuous wave radio frequency signals of different frequency,” *IET Science, Measurement and Technology*, vol. 11, no. 1, pp. 77–85, 2017.

[149] A. B. Matsko, A. A. Savchenkov, N. Yu, and L. Maleki, “Whispering-gallery-mode resonators as frequency references. I. Fundamental limitations,” *JOSA B*, vol. 24, no. 6, pp. 1324–1335, 2007.

[150] W. Liang, D. Eliyahu, V. S. Ilchenko, A. A. Savchenkov, A. B. Matsko, D. Seidel, and L. Maleki, “High spectral purity Kerr frequency comb radio frequency photonic oscillator,” *Nature communications*, vol. 6, no. 1, pp. 1–8, 2015.

[151] A. B. Matsko and L. Maleki, “Noise conversion in Kerr comb RF photonic oscillators,” *JOSA B*, vol. 32, no. 2, pp. 232–240, 2015.

[152] S. Camatel and V. Ferrero, “Narrow linewidth CW laser phase noise characterization methods for coherent transmission system applications,” *Journal of Lightwave Technology*, vol. 26, no. 17, pp. 3048–3055, 2008.

[153] Z. Liu, J. Kakande, B. Kelly, J. OCarroll, R. Phelan, D. J. Richardson, and R. Slavík, “Modulator-free quadrature amplitude modulation signal synthesis,” *Nature communications*, vol. 5, no. 1, pp. 1–7, 2014.

[154] Z. Chen, M. Yan, T. W. Hänsch, and N. Picqué, “A phase-stable dual-comb interferometer,” *Nature communications*, vol. 9, no. 1, pp. 1–7, 2018.

[155] K. Kikuchi and S. Tsukamoto, “Evaluation of sensitivity of the digital coherent receiver,” *Journal of Lightwave Technology*, vol. 26, no. 13, pp. 1817–1822, 2008.

[156] R. H. Walden, “Analog-to-digital converter survey and analysis,” *IEEE Journal on selected areas in communications*, vol. 17, no. 4, pp. 539–550, 1999.

[157] T. M. Fortier, C. W. Nelson, A. Hati, F. Quinlan, J. Taylor, H. Jiang, C. Chou, T. Rosenband, N. Lemke, A. Ludlow, D. Howe, C. W. Oates, and S. A. Diddams, “Sub-femtosecond absolute timing jitter with a 10 GHz hybrid photonic-microwave oscillator,” *Applied Physics Letters*, vol. 100, no. 23, p. 231111, 2012.

[158] D. R. Carlson, D. D. Hickstein, W. Zhang, A. J. Metcalf, F. Quinlan, S. A. Diddams, and S. B. Papp, “Ultrafast electro-optic light with subcycle control,” *Science*, vol. 361, no. 6409, pp. 1358–1363, 2018.

[159] K. Beha, D. C. Cole, P. DelHaye, A. Coillet, S. A. Diddams, and S. B. Papp, "Electronic synthesis of light," *Optica*, vol. 4, no. 4, pp. 406–411, 2017.

[160] D. S. Wu, D. J. Richardson, and R. Slavík, "Optical Fourier synthesis of high-repetition-rate pulses," *Optica*, vol. 2, no. 1, pp. 18–26, 2015.

[161] Z. Liu and R. Slavík, "Optical injection locking: From principle to applications," *Journal of Lightwave Technology*, vol. 38, no. 1, pp. 43–59, 2019.

[162] L. Lundberg, M. Mazur, A. Fiilöp, V. Torres-Company, M. Karlsson, and P. A. Andrekson, "Phase correlation between lines of electro-optical frequency combs," in *CLEO: Science and Innovations*, p. JW2A.149, Optical Society of America, 2018.

[163] L. Lundberg, M. Mazur, A. Mirani, B. Foo, J. Schröder, V. Torres-Company, M. Karlsson, and P. A. Andrekson, "Phase-coherent lightwave communications with frequency combs," *Nature communications*, vol. 11, 2020.

[164] L. Lundberg, M. Mazur, A. Lorences-Riesgo, M. Karlsson, and P. A. Andrekson, "Joint carrier recovery for DSP complexity reduction in frequency comb-based superchannel transceivers," in *2017 European Conference on Optical Communication (ECOC)*, p. Th.1.D.3, 2017.

[165] L. Lundberg, M. Karlsson, A. Lorences-Riesgo, M. Mazur, J. Schröder, and P. A. Andrekson, "Frequency comb-based WDM transmission systems enabling joint signal processing," *Applied Sciences*, vol. 8, no. 5, p. 718, 2018.

[166] C. G. Roeloffzen, L. Zhuang, C. Taddei, A. Leinse, R. G. Heideman, P. W. van Dijk, R. M. Oldenbeuving, D. A. Marpaung, M. Burla, and K.-J. Boller, "Silicon nitride microwave photonic circuits," *Optics express*, vol. 21, no. 19, pp. 22937–22961, 2013.

[167] C. Wang, M. Zhang, M. Yu, R. Zhu, H. Hu, and M. Loncar, "Monolithic lithium niobate photonic circuits for Kerr frequency comb generation and modulation," *Nature communications*, vol. 10, no. 1, pp. 1–6, 2019.

[168] M. Zhang, B. Buscaino, C. Wang, A. Shams-Ansari, C. Reimer, R. Zhu, J. M. Kahn, and M. Lončar, "Broadband electro-optic frequency comb generation in a lithium niobate microring resonator," *Nature*, vol. 568, no. 7752, pp. 373–377, 2019.

[169] M. He, M. Xu, Y. Ren, J. Jian, Z. Ruan, Y. Xu, S. Gao, S. Sun, X. Wen, L. Zhou, L. Liu, C. Guo, H. Chen, S. Yu, L. Liu, and X. Cai, "High-performance

hybrid silicon and lithium niobate Mach-Zehnder modulators for 100 Gbit s^{-1} and beyond," *Nature Photonics*, vol. 13, pp. 359–364, May 2019.

[170] P. O. Weigel, J. Zhao, K. Fang, H. Al-Rubaye, D. Trotter, D. Hood, J. Mudrick, C. Dallo, A. T. Pomerene, A. L. Starbuck, C. T. DeRose, A. L. Lentine, G. Rebeiz, and S. Mookherjea, "Bonded thin film lithium niobate modulator on a silicon photonics platform exceeding 100 GHz 3-dB electrical modulation bandwidth," *Optics express*, vol. 26, no. 18, pp. 23728–23739, 2018.

[171] C. Xiang, W. Jin, J. Guo, J. D. Peters, M. Kennedy, J. Selvidge, P. A. Morton, and J. E. Bowers, "Narrow-linewidth III-V/Si/Si_3N_4 laser using multilayer heterogeneous integration," *Optica*, vol. 7, no. 1, pp. 20–21, 2020.

[172] S. Gundavarapu, G. M. Brodnik, M. Puckett, T. Huffman, D. Bose, R. Behunin, J. Wu, T. Qiu, C. Pinho, N. Chauhan, J. Nohava, P. T. Rakich, K. D. Nelson, M. Salit, and D. J. Blumenthal, "Sub-hertz fundamental linewidth photonic integrated Brillouin laser," *Nature Photonics*, vol. 13, no. 1, pp. 60–67, 2019.

[173] IEEE, "IEEE standard for terminology and test methods for analog-to-digital converters," *IEEE Std 1241-2010 (Revision of IEEE Std 1241-2000)*, pp. 1–139, Jan 2011.

[174] E. L. Wooten, K. M. Kissa, A. Yi-Yan, E. J. Murphy, D. A. Lafaw, P. F. Hallemeier, D. Maack, D. V. Attanasio, D. J. Fritz, G. J. McBrien, *et al.*, "A review of lithium niobate modulators for fiber-optic communications systems," *IEEE Journal of selected topics in Quantum Electronics*, vol. 6, no. 1, pp. 69–82, 2000.

[175] D. Janner, D. Tulli, M. García-Granda, M. Belmonte, and V. Pruneri, "Micro-structured integrated electro-optic linbo3 modulators," *Laser and Photonics Reviews*, vol. 3, no. 3, pp. 301–313, 2009.

[176] C. Wang, M. Zhang, X. Chen, M. Bertrand, A. Shams-Ansari, S. Chandrasekhar, P. Winzer, and M. Lončar, "100-GHz low voltage integrated lithium niobate modulators," in *2018 Conference on Lasers and Electro-Optics (CLEO)*, pp. 1–2, IEEE, 2018.

[177] C. Wang, M. Zhang, B. Stern, M. Lipson, and M. Lončar, "Nanophotonic lithium niobate electro-optic modulators," *Optics express*, vol. 26, no. 2, pp. 1547–1555, 2018.

[178] A. J. Mercante, S. Shi, P. Yao, L. Xie, R. M. Weikle, and D. W. Prather, "Thin film lithium niobate electro-optic modulator with terahertz operating bandwidth," *Optics express*, vol. 26, no. 11, pp. 14810–14816, 2018.

[179] S. Pan and Y. Zhang, “Microwave photonic radars,” *Journal of Lightwave technology*, vol. 38, no. 19, pp. 5450–5484, 2020.

[180] L. Kong, M. K. Khan, F. Wu, G. Chen, and P. Zeng, “Millimeter-wave wireless communications for IoT-cloud supported autonomous vehicles: Overview, design, and challenges,” *IEEE Communications Magazine*, vol. 55, no. 1, pp. 62–68, 2017.

[181] X. Li, A. Wen, X. Li, H. Zhuo, and J. Zhao, “A disambiguation method for dual-comb-sampling-based frequency measurement,” *Journal of Lightwave Technology*, 2022.

[182] A. Shams-Ansari, D. Renaud, R. Cheng, L. Shao, L. He, D. Zhu, M. Yu, H. R. Grant, L. Johansson, M. Zhang, *et al.*, “Electrically pumped laser transmitter integrated on thin-film lithium niobate,” *Optica*, vol. 9, no. 4, pp. 408–411, 2022.

[183] I. Fatadin, S. J. Savory, and D. Ives, “Compensation of quadrature imbalance in an optical QPSK coherent receiver,” *IEEE Photonics Technology Letters*, vol. 20, no. 20, pp. 1733–1735, 2008.

[184] I. Mayer, “On Löwdin’s method of symmetric orthogonalization,” *International Journal of Quantum Chemistry*, vol. 90, no. 1, pp. 63–65, 2002.

[185] R. Wu, M. Wang, J. Xu, J. Qi, W. Chu, Z. Fang, J. Zhang, J. Zhou, L. Qiao, Z. Chai, *et al.*, “Long low-loss-litium niobate on insulator waveguides with sub-nanometer surface roughness,” *Nanomaterials*, vol. 8, no. 11, p. 910, 2018.

[186] R. Wolf, I. Breunig, H. Zappe, and K. Buse, “Scattering-loss reduction of ridge waveguides by sidewall polishing,” *Optics express*, vol. 26, no. 16, pp. 19815–19820, 2018.

[187] B. Desiatov, A. Shams-Ansari, M. Zhang, C. Wang, and M. Lončar, “Ultra-low-loss integrated visible photonics using thin-film lithium niobate,” *Optica*, vol. 6, no. 3, pp. 380–384, 2019.

[188] M. Zhang, C. Wang, R. Cheng, A. Shams-Ansari, and M. Lončar, “Monolithic ultra-high-Q lithium niobate microring resonator,” *Optica*, vol. 4, no. 12, pp. 1536–1537, 2017.

[189] A. J. Mercante, P. Yao, S. Shi, G. Schneider, J. Murakowski, and D. W. Prather, “110 GHz CMOS compatible thin film $LiNbO_3$ modulator on silicon,” *Optics express*, vol. 24, no. 14, pp. 15590–15595, 2016.

[190] C. Wang, M. Zhang, X. Chen, M. Bertrand, A. Shams-Ansari, S. Chandrasekhar, P. Winzer, and M. Lončar, “Integrated lithium niobate electro-optic modulators operating at cmos-compatible voltages,” *Nature*, vol. 562, no. 7725, pp. 101–104, 2018.

[191] D. Zhu, L. Shao, M. Yu, R. Cheng, B. Desiatov, C. Xin, Y. Hu, J. Holzgrafe, S. Ghosh, A. Shams-Ansari, *et al.*, “Integrated photonics on thin-film lithium niobate,” *Advances in Optics and Photonics*, vol. 13, no. 2, pp. 242–352, 2021.

[192] D. Banerjee, *PLL performance, simulation and design*. Dog Ear Publishing, 2006.

[193] D. Elliott, R. Roy, and S. Smith, “Extracavity laser band-shape and bandwidth modification,” *Physical Review A*, vol. 26, no. 1, p. 12, 1982.

[194] P. Gallion and G. Debarge, “Quantum phase noise and field correlation in single frequency semiconductor laser systems,” *IEEE Journal of Quantum Electronics*, vol. 20, no. 4, pp. 343–349, 1984.

[195] T. Okoshi, K. Kikuchi, and A. Nakayama, “Novel method for high resolution measurement of laser output spectrum,” *Electronics letters*, vol. 16, no. 16, pp. 630–631, 1980.

[196] P. Horak and W. H. Loh, “On the delayed self-heterodyne interferometric technique for determining the linewidth of fiber lasers,” *Optics express*, vol. 14, no. 9, pp. 3923–3928, 2006.

Appendices

Appendix A

Mathematical Derivations

This appendix provides mathematical derivations for several of the equations given earlier in the thesis. These derivations are included for completeness of the thesis.

A.1 Third order harmonic distortion products amplitudes

For a two tone input

$$V_{in}(t) = A_1 \sin(\omega_1 t) + A_2 \sin(\omega_2 t) \tag{A.1}$$

the modulator transfer function has output

$$M(V_{in}(t)) = \sin\left[\frac{\pi}{V_\pi}(A_1 \sin(\omega_1 t) + A_2 \sin(\omega_2 t))\right] \tag{A.2}$$

$$= \frac{\pi}{V_\pi}(A_1 \sin(\omega_1 t) + A_2 \sin(\omega_2 t)) - \frac{1}{3!}\left(\frac{\pi}{V_\pi}\right)^3 (A_1 \sin(\omega_1 t) + A_2 \sin(\omega_2 t))^3 + \cdots \tag{A.3}$$

considering the first two terms of the sine expansion (i.e. up to cubic order) gives the so-called third order harmonics, whose amplitudes are given in Table A.1.

Frequency	Amplitude
ω_1	$\frac{\pi A_1}{V_\pi} - \frac{1}{24}\left(\frac{\pi}{V_\pi}\right)^3\left(3A_1^3 + 6A_1A_2^2\right)$
$2\omega_1 - \omega_2$	$\frac{1}{8}\left(\frac{\pi}{V_\pi}\right)^3 A_1^2A_2$
$2\omega_1 + \omega_2$	$\frac{1}{8}\left(\frac{\pi}{V_\pi}\right)^3 A_1^2A_2$
$3\omega_1$	$\frac{1}{24}\left(\frac{\pi A_1}{V_\pi}\right)^3$
ω_2	$\frac{\pi A_2}{V_\pi} - \frac{1}{24}\left(\frac{\pi}{V_\pi}\right)^3\left(3A_2^3 + 6A_2A_1^2\right)$
$2\omega_2 - \omega_1$	$\frac{1}{8}\left(\frac{\pi}{V_\pi}\right)^3 A_2^2A_1$
$2\omega_2 + \omega_1$	$\frac{1}{8}\left(\frac{\pi}{V_\pi}\right)^3 A_2^2A_1$
$3\omega_2$	$\frac{1}{24}\left(\frac{\pi A_2}{V_\pi}\right)^3$

Table A.1: Third order harmonic distortion products amplitudes.

Appendix B

Supplementary data

The Chapter provides supplementary data for the simulations in Chapter 3 and experiments in Chapters 4 and 5.

B.1 Frequency comb power for Section 3.3

Figure B.1 shows the optical power of the frequency combs used in the simulation in Section 3 as a function of the line number.

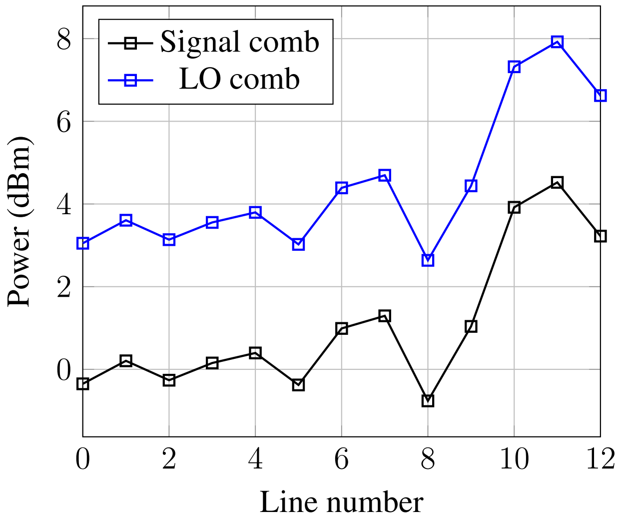

Fig. B.1: Optical power vs frequency comb line number for the frequency combs generated in the simulation described in Section 3.

B.2 Relative jitter estimation for Section 3.3

In order to obtain a reasonable estimate for relative jitter we show in Fig. B.2 a line segment approximation for a commercially available microwave synthesiser (Rohde and Schwarz SMAB-B711(N)) operating at 20 GHz. Scaling these phase noise levels by $(25/20)^2$ and $(26/20)^2$ gives us an estimate of the phase noise level for 25 GHz and 26 GHz respectively. The data sheet suggests that the internal loop filter is around 1 kHz: phase noise between two synthesizers below this frequency will be correlated and above it uncorrelated.

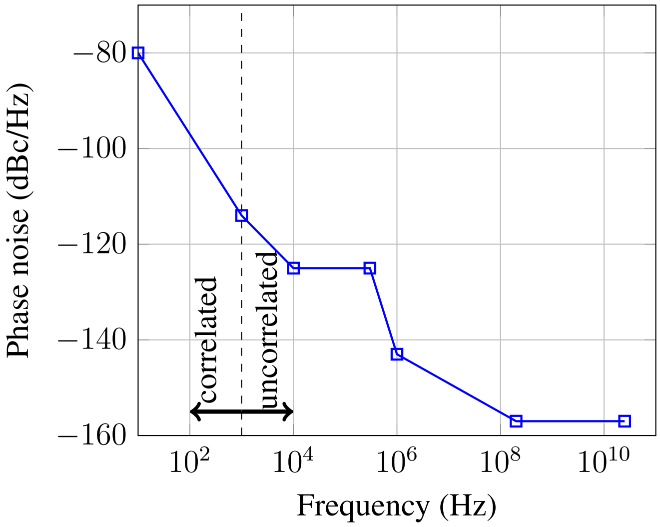

Fig. B.2: Phase noise spectrum used for the example analysis in this paper: this is a line segment approximation for the Rohde and Schwarz SMAB-B711(N) at 20 GHz. Note that by convention this is single sided phase noise spectral density, $\mathscr{L}(f) = S_\phi(f)/2$.

We can now plug these estimates into (3.21)

$$S_{\Delta\phi_n}(\omega) = n^2 \left[\left| \frac{26-25}{20} \right|^2 |\phi_c(\omega)|^2 + \left| \frac{26}{20} \phi_{u,LO}(\omega) \right|^2 + \left| \frac{25}{20} \phi_{u,sig}(\omega) \right|^2 \right] \tag{B.1}$$

and calculate the phase noise power in dBc using (3.17), writing the spectrum in Fig. B.2 as $|\phi_{RS}(\omega)|^2$

$$\frac{\overline{\Delta\phi_n^2}}{2n^2} = \frac{1}{20^2} \int_{10\text{ Hz}}^{1\text{ kHz}} |\phi_{RS}(f)|^2 \mathrm{d}f + \left[\left(\frac{26}{20} \right)^2 + \left(\frac{25}{20} \right)^2 \right] \int_{1\text{ kHz}}^{500\text{ MHz}} |\phi_{RS}(f)|^2 \mathrm{d}f \tag{B.2}$$

$$= 3.43 \times 10^{-10} + 4.83 \times 10^{-7} + 4.46 \times 10^{-7} \tag{B.3}$$

$$\overline{\Delta\phi_n^2} = n^2 (1.86 \times 10^{-6}) \tag{B.4}$$

noting the limits defined by our loop bandwidth estimate and sub-channel bandwidth, $\frac{\Delta f}{2} = 500$ MHz. In terms of relative jitter (3.22) this is

$$\sigma_j = \sqrt{\frac{2 \times 3.43 \times 10^{-10}}{(2\pi \times 1\,\text{GHz})^2} + \frac{2 \times 4.83 \times 10^{-7}}{(2\pi \times 25\,\text{GHz})^2} + \frac{2 \times 4.46 \times 10^{-7}}{(2\pi \times 26\,\text{GHz})^2}} = 9.47\,\text{fs} \tag{B.5}$$

which corresponds to 6.70 fs uncorrelated contribution from each comb.

B.3 LMX2595 phase noise estimation

The Texas Instruments LMX2595 is a single phased locked loop based fractional-N synthesiser: a simplified schematic is shown in Fig. B.3. In the experiment shown in Section 4.1, Fig. 4.1, the input frequency is 100 MHz leading to a PFD frequency of 200 MHz. The loop fractional-N divider is set to 62.5 and 65 to generate VCO frequencies of 12.5 GHz and 13 GHz respectively.

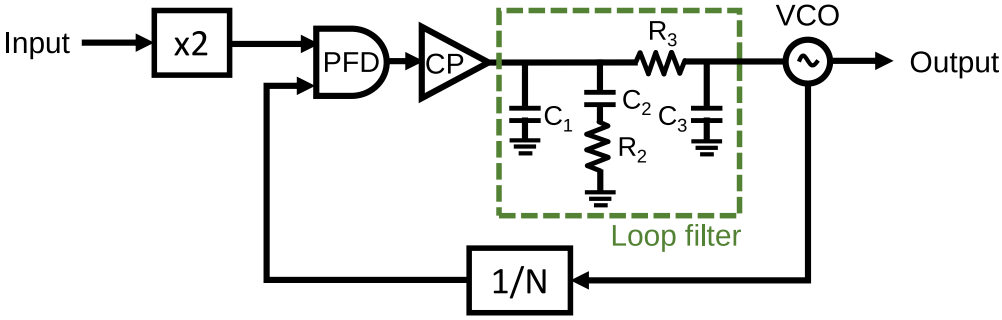

Fig. B.3: Simplified Texas Instruments LMX2595 PLL schematic. CP, charge pump; VCO, voltage controlled oscillator; PFD, phase frequency detector.

The loop filter is a 3rd order passive filter with transfer function

$$Z(s) = \frac{1 + sR_2C_2}{s(A_2s^2 + A_1s + A_0)} \tag{B.6}$$

where

$$A_0 = C_1 + C_2 + C_3 \tag{B.7}$$

$$A_1 = C_2R_2(C_1 + C_3) + C_3R_3(C_1 + C_2) \tag{B.8}$$

$$A_2 = C_1C_2C_3R_2R_3. \tag{B.9}$$

The VCO and PLL phase noise in terms of their $1/f^i$ processes are given in Table B.1. An estimate for the overall phase noise can be obtained by summing the VCO, PLL and resistor thermal noise contributions, each shaped by the PLL loop transfer function (B.6) [192]. The shaped VCO and PLL contributions are shown in Fig. 4.2.

Parameter	Value
PLL white (at 1 Hz PFD)	-236.2 dBc/Hz
PLL 1/f (at 10 kHz offset, 1 GHz output)	-129.2 dBc/Hz
Charge pump gain	15 mA
VCO $1/f^3$	156.3 dBc/Hz
VCO $1/f^2$	144.8 dBc/Hz
VCO white	178.6 dBc/Hz
C_1	390 pF
C_2	68 nF
C_3	1.8 nF
R_2	68 Ω
R_3	18 Ω

Table B.1: LMX2595 parameters.

B.4 Comb RF filters

Fig. B.4 shows the S_{21} responses for the bandpass filters used in the dual comb setup shown in Fig. 4.4. These were custom RF cavity filters designed by an external vendor to a specified 3 dB bandwidth of 25 MHz at the target frequencies of 25 GHz and 26 GHz. The 25 GHz and 26 GHz filters had a measured insertion loss of 3.92 dB and 3.98 dB respectively and a measured bandwidth of 28.1 MHz and 32.0 MHz respectively.

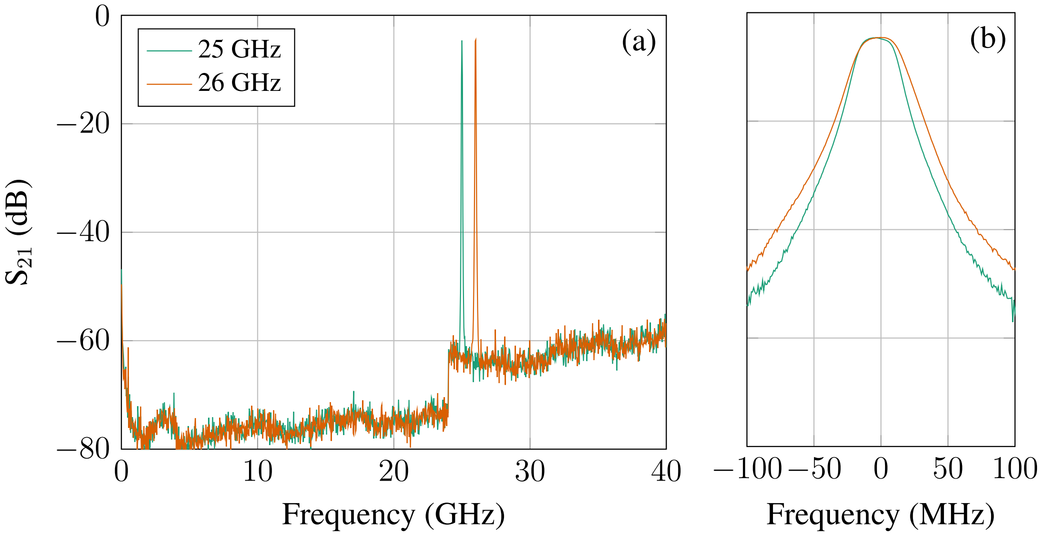

Fig. B.4: (a) Broadband and (b) narrowband RF filter response. The frequency axis in (b) is centred at the respective target frequency.

B.5 Sub-band analog front end

Fig. B.5 shows the circuit diagram for the sub-band analog front end used in Chapters 4 and 5. It consists of a modified commercial photodiode-TIA (Thorlabs PDB480-AC), 650 MHz LC low pass filter (VLFX-650+) and 4 GSa/s ADC with balun and matching network (Analog Devices AD9209 on AD9081-FMCA-EBZ evaluation board).

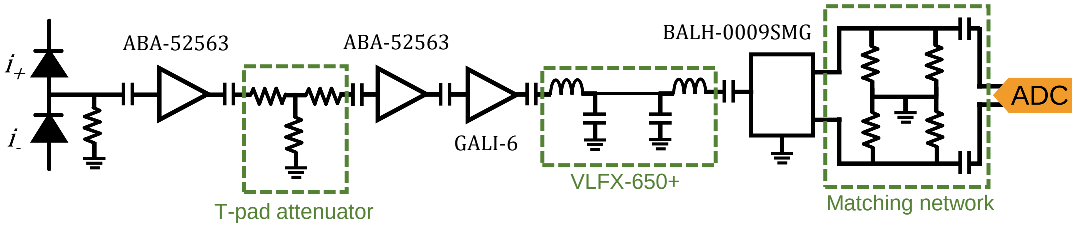

Fig. B.5: Analog front end circuit diagram, interfacing the photodiode-TIA to the differential input of the ADC.

B.6 Laser linewidth

Given a laser with frequency noise spectral density $S_{\Delta\nu(f)}$, the Wiener-Khintchine theorem allows us to calculate the laser line shape via the Fourier transform of the autocorrelation function $R_{EE}(\tau)$ [193]

$$S_E(\nu) = \int_{-\infty}^{\infty} e^{-i2\pi\nu\tau} R_{EE}(\tau) d\tau. \tag{B.10}$$

The autocorrelation function itself is defined

$$R_{EE}(\tau) = E^*(t)E(t+\tau) \tag{B.11}$$

which for the laser light field

$$E(t) = E_0 e^{i(2\pi\nu_0 t + \phi(t))} \tag{B.12}$$

at frequency ν_0 with phase noise $\phi_0(t)$, is

$$R_{EE}(\tau) = E_0^2 e^{i2\pi\nu_0 t} \exp\left[- \int_{-\infty}^{\infty} S_{\Delta\nu}(f) \frac{\sin^2(\pi f \tau)}{f^2} df \right]. \tag{B.13}$$

For the trivial case of white frequency noise, $S_{\Delta}\nu(f) = h_0$, this leads to Lorentzian lineshape [194]. In general the lineshape (B.10) cannot be evaluated analytically, but it has been shown that for $1/f$ frequency noise $S_{\Delta}\nu(f) = h_{-1}f^{-1}$ the lineshape is approximately Gaussian [115, 114].

When the laser frequency noise contains both white and $1/f$, the laser lineshape can be described by a Voigt profile [114]. The Voigt profile is defined as a convolution between a Gaussian and Lorentzian

$$V(x;\sigma,\gamma) = \int_{-\infty}^{\infty} G(x';\sigma)L(x-x';\gamma)dx' \tag{B.14}$$

for the Gaussian profile

$$G(x;\sigma) = \frac{e^{x^2/(2\sigma^2)}}{\sigma\sqrt{2\pi}} \tag{B.15}$$

with standard deviation σ, and Lorentzian profile

$$L(x;\gamma) = \frac{\gamma}{\pi(x^2+\gamma^2)} \tag{B.16}$$

with half width at half maximum γ. Since the Voigt profile cannot be expressed in a closed form, it is often approximated by a linear combination of the Gaussian and Lorentzian functions, known as the pseudo-Voigt

$$V(x;\gamma,\eta) \approx \eta G(x;\gamma) + (1-\eta)L(x;\gamma), \text{ for } 0 \geq \eta \leq 1 \tag{B.17}$$

where σ and γ are related by

$$\sigma = \frac{\gamma}{\sqrt{2\ln(2)}}. \tag{B.18}$$

The parameter η expresses the weighting of the Gaussian or Lorentzian in the overall lineshape with $\eta = 1$ meaning a pure Gaussian and $\eta = 0$ a pure Lorentzian.

The linewidth of the low linewidth laser (NP Photonics Rock Module ULTRA) used as the seed laser for the dual comb setup (Fig. 4.4) was measured using the delayed self-heterodyne method [195]. The delay line used was 81 km (corresponding to a delay of 389 μs) and the non-delayed portion was modulated by a acoustic optical modulator at a frequency of 35 MHz. 100 averages of the combined signals were detected by an electrical spectrum analyser at a resolution bandwidth of 10 Hz, after beating on a single photodiode.

The observed lineshape is plotted in Fig. B.6. A pseudo-Voigt profile with $\eta = 0.34$ fits the observed spectrum with an $R^2 = 0.9996$, giving a γ and corresponding Lorentzian laser full width half maximum linewidth of 2.3 kHz. Note that this is significantly larger than described in the laser data sheet < 600 Hz, due to the insufficient delay [196] used in the specification (25 km, 120 μs).

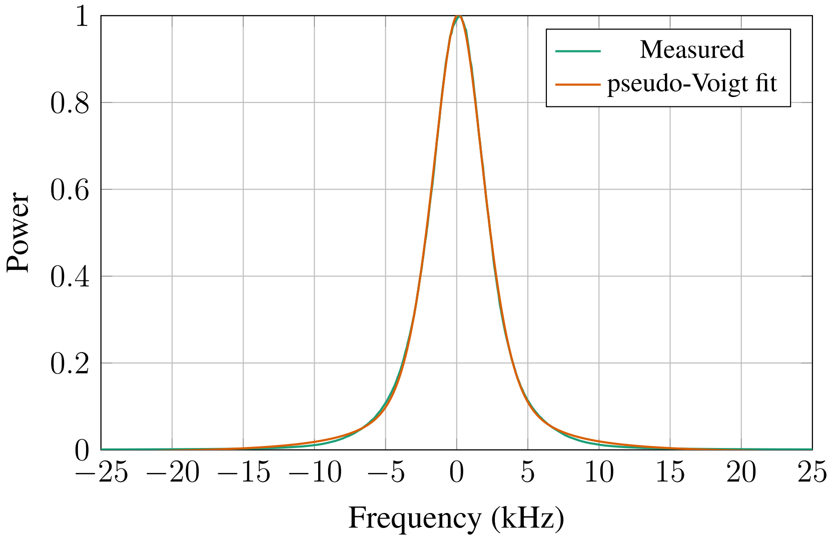

Fig. B.6: Dual comb seed laser lineshape. The observed γ and corresponding Lorentzian laser full width half maximum linewidth is 2.3 kHz.